Anomalous Diffusion in Artificial Lipid Bilayers

Helena L. E. Coker
Wadham College
University of Oxford

A thesis submitted for the degree of
Doctor of Philosophy
in Physical and Theoretical Chemistry

Trinity 2018

Declaration

The work described in this thesis was carried out in the laboratory of Professor Mark Wallace, between October 2014 and September 2016 in the Chemistry Research Laboratory of the University of Oxford and between September 2016 and March 2018 at Britannia House, King's College London. The work described within this thesis is my own unless explicitly attributed to my collaborators. This work has not been submitted previously for any other degree at the University of Oxford or any other university. Publications stemming from this work are detailed in Appendix A.

Helena L. E. Coker

Trinity 2018

Abstract

Anomalous Diffusion in Artificial Lipid Bilayers

Helena L. E. Coker - Wadham College - University of Oxford

Submitted for the degree of Doctor of Philosophy in Trinity Term 2018

Diffusion is a process essential to life. The way diffusion processes occur at, and within, the cell membrane is of particular importance for cellular signalling, transport and cellular integrity. However, within cell membranes, diffusion of lipids and proteins has been shown to be 'anomalous'. In such cases the molecules do not conform to basic Brownian motion and instead show slower diffusion over long timescales. The cell exploits this to tightly control the movement of key molecules including receptors. Although it has been hypothesised that this is due to the complex, crowded environment found within the membrane, the physical basis for anomalous diffusion is not yet fully understood and certainly is not well controlled in current membrane mimics. In the present work, artificial lipid bilayers were used to produce platforms in which to exhibit, control and study anomalous diffusive processes. A combination of fluorescence and optimised interferometric scattering microscopies, allowed careful study of this diffusive behaviour over biologically relevant length and timescales.

Bay 5

And through the dark nothingness of the bay,
a beam of laser fine light strikes gold
riding the sea in its melancholic random walk.

With contrast as bright and clear as day,
the image is stacked in a memory, only to be processed
and morphed until no one can talk

of its original beauty. What was looked upon in that way?
With curiosity and hope. Whose dance will be searched for,
whose likeness is sought

through the dark nothingness of the bay.

Acknowledgements

I would like to acknowledge my supervisor, Professor Mark Wallace, for supporting me and for providing the ERC funding for this project. Thank you to Professor Hagan Bayley for continued supervision at the University of Oxford. I'm very grateful for the members of the Wallace lab; in no particular order, cheers to Eve Weatheril, Jason Sengel, John Danial, Joanne Carniello, Carina Monico, Lyndsey Starr and Ravinash Krishna Kumar. In particular, I acknowledge Matthew Blosser for his support and ideas, Hajra Basit for technical expertise and Vivek Ramakrishna for being the light of the lab. I specifically thank Matthew Cheetham for working with me on the anomalous diffusion projects, teaching me MATLAB and patiently explaining some difficult concepts. I'd like to thank my parents for raising me up to a place from which I was even capable of completing this thesis. Parenting can be a thankless task but I hope you realise how grateful I am. Similarly, I am grateful to Sophie for the advice, the hummus and keeping me going whilst I was in London. Finally, thank you to Donald Fraser whose impact on my life and my success is ineffable.

Contents

1 Introduction **1**

1.1 Lipids and lipid self assembly 1

1.2 Lipids in cell membranes 4

1.2.1 Fluidity, viscosity and continuity 5

1.2.2 Asymmetry 5

1.2.3 Domain formation 6

1.2.4 Interactions with proteins 6

1.2.5 Interaction with the cytoskeleton 7

1.3 Diffusion 7

1.3.1 Theory of diffusion 7

1.3.2 Anomalous diffusion 8

1.3.3 The importance of anomalous diffusion in biological membranes 8

1.4 Artificial lipid bilayers 10

1.4.1 Black Lipid Membranes, BLMs 10

1.4.2 Supported Lipid Bilayers, SLBs 11

1.4.3 Droplet Interface Bilayers, DIBs 13

1.5 Techniques for studying diffusion in model membrane systems 14

1.5.1 Total Internal Reflection Fluorescence, TIRF 14

1.5.1.1 Total Internal Reflection, TIR 14

1.5.1.2 Evanescent fields for fluorescence microscopy 15

1.5.2 Interferometric Scattering, iSCAT 16

2 General Methods **23**

2.1 Materials 23

2.1.1 Lipids 23

2.1.2 Nanoparticles 24

2.1.3 Other materials 24

2.1.4 Microscopy materials 24

2.2 Model membrane platforms . . . 24
2.2.1 SLBs . . . 24
2.2.2 DIBs . . . 25
2.2.2.1 Lipid-in droplet preparation . . . 26
2.2.2.2 Lipid-out droplet preparation . . . 26
2.3 Microscopy . . . 26
2.3.1 Single molecule TIRF experiment . . . 26
2.3.2 iSCAT . . . 27
2.3.2.1 Image acquisition . . . 29
2.3.2.2 Background subtraction . . . 29
2.4 Single Particle Tracking, SPT . . . 29
2.4.1 TrackMate . . . 30
2.4.2 Contrast and signal to noise analysis . . . 30
2.4.3 Diffusion analysis . . . 31
2.4.3.1 MSD calculation . . . 31
2.4.3.2 $\langle \Delta r^2 \rangle (4\Delta t)^{-1}$ *vs.* Δt plots . . . 32
2.4.3.3 Extraction of the anomalous exponent (α) and anomalous transport coefficient (Γ) . . . 32
2.4.4 Monte Carlo diffusion simulations . . . 33

3 iSCAT Single Particle Tracking Experiment Optimisation 34
3.1 Experimental requirements . . . 34
3.2 Microscope improvements . . . 36
3.2.1 Magnification . . . 36
3.2.2 Imaging speed and illumination . . . 37
3.3 Experiment improvements . . . 38
3.3.1 Scattering cross-section . . . 38
3.3.2 Reducing reflected and stray light . . . 41
3.3.2.1 Bilayer stacks . . . 42
3.3.2.2 DIBs . . . 43
3.4 Optimisation of acquisition and analysis . . . 44
3.4.1 Image collection and initial processing . . . 44
3.4.2 Tracking . . . 44
3.5 Summary . . . 44

4 Controlling Anomalous Diffusion in Artificial Membranes Using PEG-lipids 46
4.1 Introduction . . . 46
4.2 Specific methods . . . 47
4.2.1 Lipids . . . 47
4.2.2 Atomic Force Microscopy, AFM . . . 49
4.2.3 Fluorescence Recovery After Photobleaching, FRAP . . . 49
4.2.4 DIBs . . . 49
4.2.5 Tracking . . . 50
4.2.6 Monte Carlo simulations . . . 50
4.3 Theory . . . 50
4.4 Results . . . 52
4.4.1 AFM shows interfacial defects . . . 52
4.4.2 PEG bilayers exhibit anomalous behaviour . . . 54
4.4.3 Anomalous exponent can be finely tuned . . . 55
4.4.4 Controls . . . 59
4.4.4.1 Rescue of anomalous behaviour . . . 59
4.4.4.2 DIBs do not exhibit anomalous behaviour . . . 59
4.4.5 Monte Carlo simulations . . . 59
4.4.6 De-dimensionalisation . . . 62
4.5 Discussion . . . 63
4.6 Conclusion . . . 67

5 Controlling Anomalous Diffusion in Artificial Membranes Using Urea 69
5.1 Introduction . . . 69
5.2 Specific methods . . . 69
5.2.1 Materials . . . 69
5.2.2 SLBs . . . 70
5.2.3 TIRF imaging . . . 70
5.3 Results . . . 70
5.3.1 Urea slows diffusion in a concentration dependent manner . . . 70
5.3.2 Urea induces anomalous behaviour in a time dependent manner 71
5.3.2.1 Confinement evident in the particle locations . . . 72
5.3.3 De-dimensionalisation . . . 73
5.4 Discussion . . . 73
5.5 Conclusion . . . 76

6 Topography *vs.* Topology **77**
6.1 Introduction . . . 77
6.2 Theory . . . 77
6.2.1 Rectangular wave model . . . 79
6.2.2 Sine wave model . . . 79
6.3 Specific methods . . . 80
6.3.1 Patterned substrates . . . 80
6.3.1.1 Pillars . . . 80
6.3.1.2 Nanowalls . . . 80
6.3.2 Anisotropic MSD analysis . . . 80
6.3.3 iSCAT Analysis . . . 82
6.3.4 Simulations . . . 82
6.3.4.1 Sine wave surface . . . 83
6.3.4.2 Rectangular wave surface . . . 84
6.3.5 Fibronectin printing . . . 84
6.4 Results . . . 85
6.4.1 Bilayers conform to substrate profile . . . 85
6.4.2 Diffusion on nanowalls is anisotropic . . . 88
6.4.3 Topography does not cause anomalous behaviour . . . 90
6.4.4 Using diffusion data to estimate feature height . . . 91
6.4.4.1 Model validation with simulations . . . 91
6.4.4.2 Application of the rectangular-wave model to the experimental data . . . 94
6.4.4.3 Immobile obstacles are required to induce anomalous behaviour . . . 96
6.5 Discussion . . . 97
6.6 Conclusions . . . 101

7 Conclusions and Outlook **103**

A Publications **107**

B Code **108**
B.1 Python . . . 108
B.1.1 GUI free TrackMate . . . 108
B.1.2 Cine-TIFF conversion and averaging . . . 113
B.2 ImageJ background subtraction macro (Java) . . . 117

B.3 Matlab 117
B.3.1 Track analysis 117
B.3.2 Extraction of spot intensities using TrackMate XML co-ordinates 119
B.3.3 Monte Carlo simulations 122

Bibliography **127**

List of Figures

1.1 General phospholipid structure and structure of lipid components. . . 2
1.2 Structure of DPhPC. 3
1.3 Self assembly of lipids. 3
1.4 Generalised packing of a phospholipid into a liposome. 4
1.5 Compartmentalisation of a cell membrane. 9
1.6 Schematic of a black lipid membrane. 11
1.7 Schematic of a SLB. 12
1.8 Schematic of droplet interface bilayers. 13
1.9 Scheme of early TIRF microscopy. 15
1.10 Scheme of a single molecule TIRFM experiment. 16
1.11 RCIM of a cell. 18
1.12 Scheme of the antiflex technique. 19
1.13 Scheme of a single molecule iSCAT experiment. 20

2.1 Schematic of a DIB custom device. 25
2.2 Scheme of a TIRF microscope. 27
2.3 Scheme of an iSCAT microscope. 28
2.4 Schematics of second moment and $\langle \Delta r^2 \rangle (4\Delta t)^{-1}$ *vs.* Δt plots. 32

3.1 Effect of SNR on MSD alalysis. 35
3.2 Increase in magnification. 36
3.3 Scheme of the optimised iSCAT microscope. 37
3.4 Effect of gold label size on contrast and SNR. 39
3.5 Effect of gold label size on diffusion. 41
3.6 Contrast enhancement using Nanolane substrates. 42
3.7 Schematic of the custom device for Nanolane substrates. 43

4.1 Schematic of SLB disruption by PEG-DPPE. 47
4.2 Position of PEG-DPPE levels used in relation to the mushroom-brush transition. 48

4.3 Schematic of the asymmetric PEG-DPPE containing DIB. 49
4.4 AFM imaging of PEG(2K)-DPPE containing SLBs. 52
4.5 AFM force curves. 52
4.6 Thresholding and autocorrelation of AFM images. 53
4.7 Anomalous diffusion in PEG bilayers. 56
4.8 Extraction of α and Γ. 57
4.9 Variation of α and Γ with mol% PEG and EAF. 58
4.10 Normal diffusive behaviour can be rescued. 60
4.11 Diffusive behaviour in DIBs remains normal. 60
4.12 Monte Carlo simulations of anomalous diffusion 61
4.13 De-dimensionalisation of the data. 62

5.1 Effect of urea concentration on lipid diffusion. 71
5.2 Time dependence of anomalous behaviour induced by 1 M urea. . . . 71
5.3 Time course of spot locations from tracked particles. 72
5.4 Relationship of the anomalous exponent with estimated EAF. 72
5.5 De-dimensionalisation of the data to extract a length scale. 73

6.1 Schematic of a rectangular wave. 78
6.2 Schematic of the pillared substrate. 81
6.3 Schematic of the nanowall substrate. 81
6.4 Schematic of the projection of a sine wave onto a plane. 83
6.5 iSCAT imaging of pillared substrate. 85
6.6 Pillar distances estimated from tracks. 86
6.7 iSCAT imaging of nanowall substrate, 200 nm spacing. 87
6.8 iSCAT imaging of nanowall substrate, 600 nm spacing. 89
6.9 Comparison of isotropic and anisotropic MSD analysis of diffusion on Nanowall samples. 90
6.10 Anomalous exponents show normal diffusion on topographical substrates. 91
6.11 Application of the rectangular wave model to data from simulations on rectangular wave and sine wave surfaces. 92
6.12 Quadratic fitting to the sine wave simulation data. 94
6.13 Application of the rectangular wave model to experimental data. . . . 95
6.14 Confinement of tracks after fibronectin printing. 96
6.15 Diffusive behaviour on 200 nm height nanowalls printed with fibronectin and comparison with topographical substrate. 97
6.16 Anomalous exponents distinguish between topography and topology. . 98

Abbreviations

α	anomalous exponent
AOD	acouso-optic deflector
AFM	atomic force microscopy
Atto488-DOPE	Atto-488-1,2-dioleoyl-*sn*-glycero-3-phosphoethanolamine
biotin-DOPE	1,2-dioleoyl-*sn*-glycero-3-phosphoethanolamine-N-cap-biotinyl
BLM	black lipid membrane
CMOS	complementary metal oxide semiconductor
DCM	dichroic mirror
DIB	droplet interface bilayer
D	lateral diffusion coefficient
D_{xx}	diffusion coefficient in the x direction
D_{yy}	diffusion coefficient in the y direction
DOPC	1,2-dioleoyl-*sn*-glycero-3-phosphocholine
DPhPC	1,2-diphytanoyl-*sn*-glycero-3-phosphocholine
EAF	excluded area fraction
EDTA	ethylenediamminetetraacetic acid
EF	emission filter
EM	electron microscopy / electron micrograph
EM CCD	electron-multiplying charge-coupled device
FCS	fluorescence correlation spectroscopy
FM	flip mirror
FRAP	fluorescence recovery after photobleaching
FWHM	full width half maximum
Γ	anomalous transport coefficient
GUI	graphical user interface
GUV	giant unilamellar vesicle
HEPES	4-(2-hydroxyethyl)-1-piperazineethanesulfonic acid
ICM	interference contrast microscopy
IRM	interference reflection microscopy
iSCAT	interferometric scattering
λ	characteristic length scale
LAP	linear assignment problem
LoG	Laplacian of Gaussian
LUV	large unilamellar vesicle

MC	Monte Carlo
MD	molecular dynamics
MQ	MilliQ water (deionised)
MSD	mean-squared displacement
OD	optical density
PBS	phosphate buffered saline or polarising beam splitter
PEG	polyethylene glycol
PEG(1K)-DPPE	1,2-dipalmitoyl-*sn*-glycero-3-phosphoethanolamine-N-... ...[methoxy(polyethylene glycol) - 1000] ammonium salt
PEG(2K)-DPPE	1,2-dipalmitoyl-*sn*-glycero-3-phosphoethanolamine-N-... ...[methoxy(polyethylene glycol) - 2000] ammonium salt
PEG(5K)-DPPE	1,2-dipalmitoyl-*sn*-glycero-3-phosphoethanolamine-N-... ...[methoxy(polyethylene glycol) - 5000] ammonium salt
PMMA	poly(methyl methacrylate)
PSD	position sensitive diode
PSF	point-spread function
QCM-D	quartz crystal microbalance with dissipation monitoring
QD	colloidal nanocrystalline semiconductor - quantum dot
QWP	quarter wave plate
RICM	reflection interference contrast microscopy
SEEC	surface enhanced ellipsometric contrast microscopy
SLB	supported lipid bilayer
SNR	signal to noise ratio
SPT	single particle tracking
surf	Nanolane surface
SUV	small unilamellar vesicle
τ	characteristic time scale or *jump time*
Δt	observation time
TIFF	Tagged Image File Format
TIRFM	total internal reflection fluorescence microscopy
TR-DHPE	TexasRed™1,2-dihexadecanoyl-*sn*-glycero-3-phosphoethanol... ...amine triethylammonium
UV	ultra-violet light
Vis	visible light

Chapter 1

Introduction

Biological phenomena within the plasma membrane, including diffusion and binding events occur on nanometer length scales and micro to millisecond time scales. By detecting single molecules at this level, one can get direct insights into the structure, function and interaction of the individual units which form the membrane. Being able to resolve these molecules in simplified systems presents a powerful platform to better understand the workings of cells, which are often too complex to study as a whole. This thesis focusses on the application of single particle tracking techniques to study lipid diffusion processes in artificial membranes. Diffusion is essential for cellular signalling, reactions and survival and yet is known not to be *normal*, that is in cells, diffusion deviates from Brownian behaviour. Instead, many cellular diffusion processes can be described as *anomalous*. To study these processes total internal reflection fluorescence microscopy (TIRFM) and interferometric scattering (iSCAT) microscopy are employed. This chapter will introduce these techniques as well as lipids, artificial membrane platforms and the theory of anomalous diffusion.

1.1 Lipids and lipid self assembly

Lipids, particularly phospholipids, are essential for life and are a major component of cell membranes [1]. Phospholipids, in the most basic sense, are comprised of a head and tail region (Figure 1.1A-D). The head region is polar and can be zwitterionic or carry a non-zero net charge. In this example, 1,2-dioleoyl-*sn*-glycero-3-phosphocholine (DOPC), the head group is a choline derivative. There are many other possible head groups which dictate the overall charge and area of the phospholipid (Figure 1.1E-K).

The hydrocarbon tail, Figure 1.1A, is linked to the head group by a glyceryl moiety (B). The hydrocarbon tail is biosynthestically derived from fatty acids (Figure 1.1I-K) and is therefore hydrophobic. Owing to the mechanism of this pathway, any

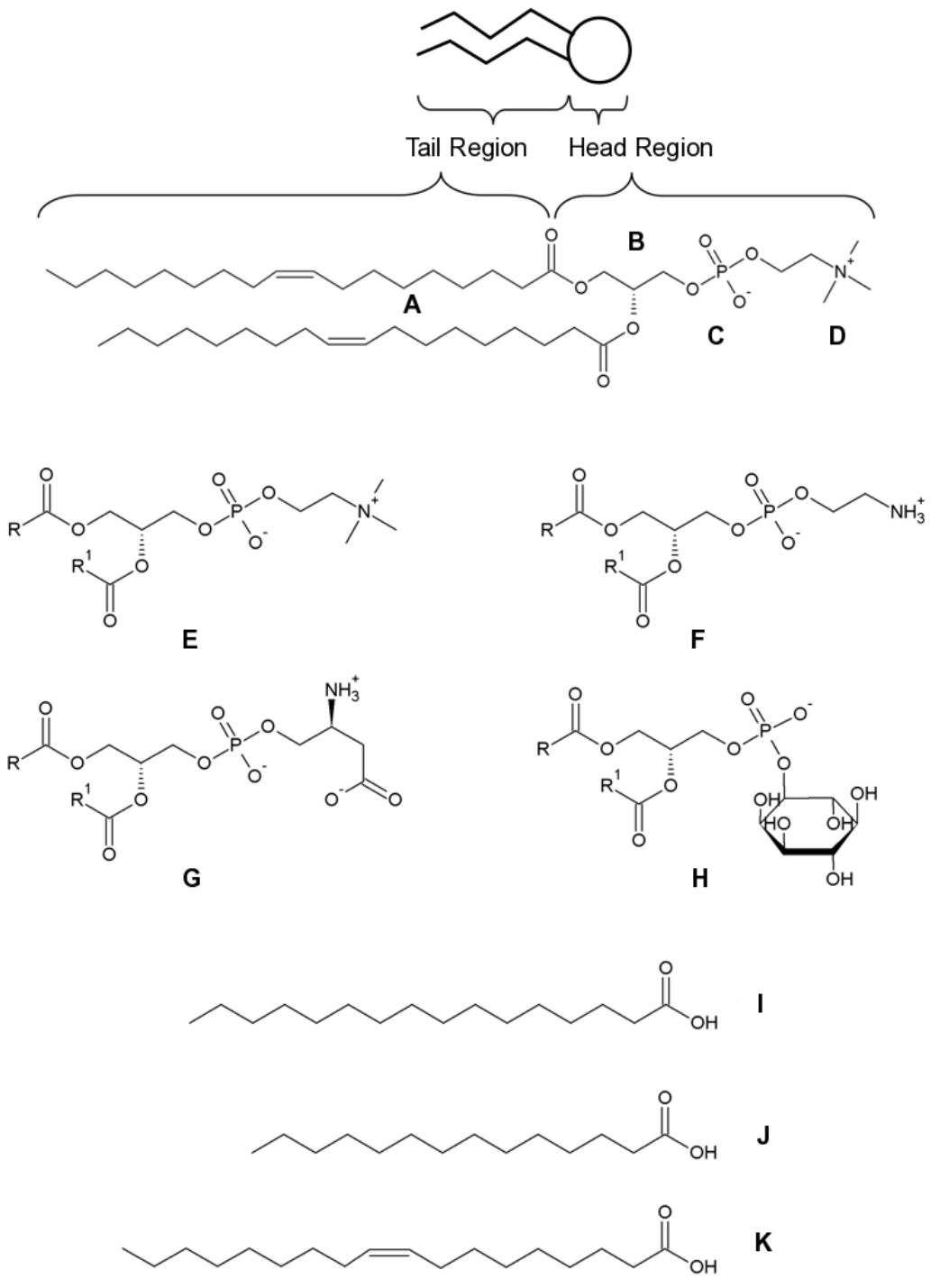

Figure 1.1: **General phospholipid structure and structure of lipid components.** Schematic representation of a phospholipid molecule and how this maps onto the structure of DOPC. **(A)** hydrocarbon chain, **(B)** glycerol linkage, **(C)** phosphate group and **(D)** choline head group. Examples of common lipid components; Head regions **(E-H)** and fatty acid tails **(I-K)**. **(E)** phosphatidylcholine, **(F)** phosphatidylethanolamine, **(G)** phosphatidylserine, **(H)** phosphatidylinositol, **(I)** palmitic acid (hexadecanoic acid), **(J)** myristic acid (tetradecanoic acid) and **(K)** oleic acid ((9Z)-Octadec-9-enoic acid).

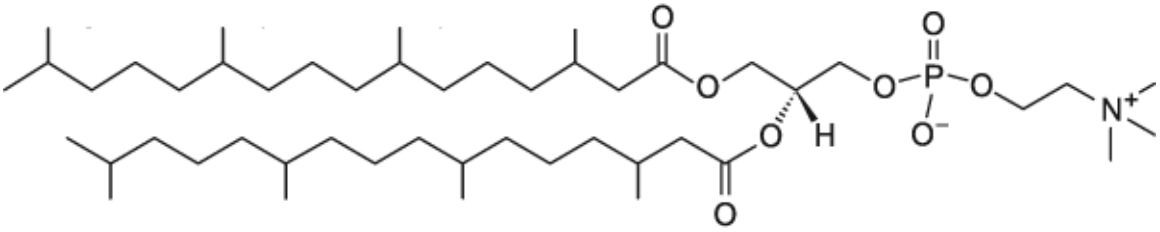

Figure 1.2: **Structure of DPhPC.**

unsaturation is always an alkene moiety of cis (Z) configuration [2]. There are a number of different hydrocarbon tails found abundantly in nature and further modified chains, such as in diphytanylephosphatidylcholine (DPhPC, Figure 1.2), available [3]. The saturation of the chain affects the shape and volume of the tail region, with unsaturation leading to kinks and hence a larger apparent molecular volume.

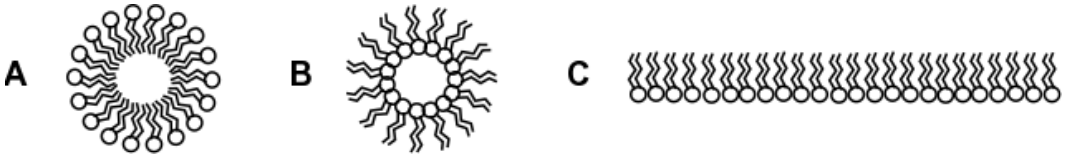

Figure 1.3: **Selfassembly of lipids. (A)** micelle, **(B)** inverse micelle and **(C)** a planar monolayer.

At an interface between organic and aqueous phases or at an air/water interface, phospholipids orientate to the most thermodynamically stable state. The polar head groups will interact with the aqueous phase, while the tails extend into the non-polar medium [4]. In mixtures of aqueous and organic media, approximately spherical micelles or reverse micelles are formed around the immiscible droplets (Figure 1.3 A and B respectively). At planar surfaces such as that in a Langmuir Trough, planar monolayers will form (Figure 1.3C) [5].

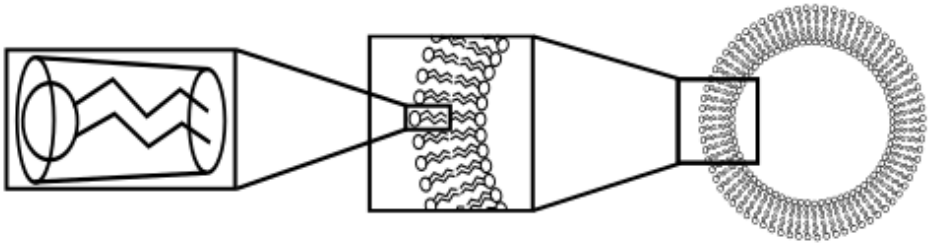

Figure 1.4: **Generalised packing of a phospholipid into a liposome.** The truncated cone shape of a lipid packs into a thermodynamically favourable spherical bilayer structure.

The self-assembled shape is predicted by the packing parameter equal to the ratio expressed in Equation 1.1:

$$\frac{V}{(al_c)} \tag{1.1}$$

where V is the tail volume, a the head group area and l_c the critical tail length. Most two chain lipids, such as phospholipids, have a packing parameter between 0.5 and 1. This describes a truncated cone shape which, in the presence of only aqueous medium, best packs into a flexible bilayer vesicle structure (Figure 1.4) [6]. The phospholipids spontaneously form spherical bilayers to *'shield'* the hydrophobic tails in a shell of polar head groups. These structures, first formally observed in 1964 by Bangham [7] are most commonly referred to as vesicles or liposomes. Preparations of vesicles are named by their size and lamellarity. In this work the most relevant preparations are of small unilamellar vesicles (SUVs) of up to 100 nm in diameter. There are, of course, many other parameters which affect the shape of the self assembled structures. These include lipid concentration, temperature, lipid charge and osmolarity of the aqueous medium.

1.2 Lipids in cell membranes

This spontaneous self assembly into secondary structures and compartments is exploited in biology to create selectively permeable barriers or membranes. It is arguable that the main function of such membranes is to separate the inner environment of the cell, the cytosol and organelles, from the external world. The lipids themselves offer some selectivity to which molecules can pass from one side to the other owing to the hydrophobic core of the bilayer [8]. Non-polar, fat soluble molecules can cross the

membrane relatively freely, where as small polar, but uncharged, molecules such as water traverse more slowly. The bilayer is impermeable to ions which are not soluble in the fatty lipid tail region.

In 2016 Bernardino de la Serna *et al.* outlined nine *'intrinsic properties of cell membrane essential for their function'* [9]. All of these involve the nature and behaviour of the lipid portion of the cell membrane. The following sections outline these properties.

1.2.1 Fluidity, viscosity and continuity

Although incorporation of different phospholipids, as well as different classes of lipids, further affects the permeability of biological membranes [10], lipids alone could not explain the permeability of membranes to water and ions. Thus it was proposed that integral proteins were an essential constituent of membranes which provide transport across the bilayer. Such properties prompted the general acceptance of the *fluid mosaic* model [11], which described an environment in which components were free to move and diffuse within the membrane. This model also highlighted the continuity of the membrane allowing molecules to diffuse anywhere.

The diverse lipid composition of biological membranes and protein content, finely tunes the fluidity and viscosity of the barrier [12]. Notably, sterols, such as cholesterol, insert into the hydrophobic portion of the membrane and modulate membrane rigidity in a bidirectional manner [13]. Cells can therefore modulate lipid composition to maintain plasticity of the membrane [14] such that size, rigidity and shape can alter if necessary, for example to accommodate osmotic or temperature changes as well as morphological changes [15, 16, 17, 18].

The Saffmann-Delbrück hydrodynamic model [19] highlighted the importance of the membrane viscosity. This model provides a means to estimate the free movement of integral membrane proteins and other 'solid inclusions' within the fluid-mosaic. The membrane is modelled as a viscous fluid surrounded by bulk liquid of lower viscosity. The model can be used to approximate the diffusion coefficients of nano to micro-scale inclusions and can be modified to better describe larger inclusions such as macro-scale phase separation [20].

1.2.2 Asymmetry

Biological membranes are largely asymmetric; the composition of the inner leaflet is different to the outer leaflet. This is true of protein and carbohydrate content, but

also of the lipids themselves [21, 22]. Early work could not elucidate the role that lipid asymmetry might play in the proper functioning of the cell membrane and the notion that it was an *'incidental consequence'* was not dismissed [22]. However, more recent work has suggested a role of lipid asymmetry in maintaining membrane rigidity [23] and the thermodynamic stabilisation of curvature [24]. For example, in prokaryotic cells cardiolipin enrichment is evident at the poles of bacillus [25]. The role of proteins in maintaining the asymmetric distribution of lipids has been thoroughly reviewed in the last 15 years [26, 27].

1.2.3 Domain formation

In eukaryotic cells, cholesterol is closely linked with sphingolipids, such as sphingomyelin, in both physical localisation as well as homeostatic influences [28]. The *'preference'* of cholesterol for sphingolipid containing membranes further affects the packing dynamics leading to phase separation. These lipids often segregate into different regions tens of nanometers in size, nano-domains [29], to domains on the mesoscale. Domains are often *'registered'* meaning that the local enrichment of a particular lipid is present at the same location of both leaflets of the bilayer. This has been attributed to inter-leaflet coupling, yet full understanding of the roles of particular lipids in this, and the effect of interdigitation is still not fully elucidated [9].

Nano-domains, also referred to as lipid rafts, are particularly important in supporting, compartmentalising and concentrating certain membrane proteins [30]. These domains are known to be highly dynamic [29] and therefore one might expect an effect on the diffusion of molecules either within them or which interact with the boundaries. This is a deviation from the standard fluid-mosaic model which was addressed by Nicholson in 2014 [31].

1.2.4 Interactions with proteins

As alluded to above, the lipid portion of the membrane is hydrophobic and therefore functional macromolecules must be included to allow transport of polar or charged molecules. Proteins account for between 25 - 75 % of the mass of the cell membrane depending on the type, and function, of the membrane [10]. Association of proteins with the membrane occurs by several mechanisms, including covalent attachment to lipid anchors, electrostatic interactions and amphipathic partitioning dictated by the tertiary structure of hydrophobic and polar amino acid residues. However arguably,

the class of proteins most important to membrane function is the large group of transmembrane proteins. As these protein span the bilayer, they have large zones of interaction with the lipids. Therefore, it is the role of the lipids to accommodate these, makes sure that they are stable, properly folded and function correctly. The ability of lipids to account for hydrophobic mismatch and undergo specific interactions with proteins is key [32]. The *mattress model* [33], provided by Mouritsen in 1984, emphasised the importance of this. This thermodynamic model describes the lipid bilayer as an elastic matrix in which individual springs (proteins) are embedded, both are described as having their own spring constants.

1.2.5 Interaction with the cytoskeleton

The cytoskeleton is a network of proteinaceous fibres comprised, in eukaryotes, of actin, tubulin and the family of intermediate filament proteins [34]. Although not part of the membrane, the cytoskeleton is essential in maintaining membrane integrity and stability by its close interaction with the bilayer [35]. It is not a unilateral relationship however and studies have shown that the membrane also regulates cytoskeletal dynamics [36]. As early as 1976 the importance of the cytoskeleton and extracellular matrix structuring the membrane was included in the Singer and Nicolson model [37]. More recent extensions to cell membrane models (compartment model) have focussed the key role of the cytoskeleton in compartmentalisation and controlling the spacial distribution of molecules within the cell and its environment [38].

1.3 Diffusion

Thus, the cell membrane is far from the simple fluid-mosaic model first proposed in 1972, yet it is clear from the preceding section that much of the function of the cell membrane is dependant on the careful control of the the movement of molecules. This movement at the very basic level is controlled by diffusion and it is therefore important to understand what is meant by this.

1.3.1 Theory of diffusion

Brownian motion first explained in 1905 [39], refers to the simple random walk of a molecule undergoing stochastic bombardment by other molecules. As discussed above the membrane exhibits 2D continuity and therefore here, diffusion is considered within a plane.

The mean squared displacement (second moment) of a free particle scales linearly with the observation time, whilst the mean displacement (first moment) should be exactly zero by symmetry. This is expressed via

$$\left\langle \Delta r^2 \right\rangle = 4D\Delta t, \quad \langle \Delta \mathbf{r} \rangle = \mathbf{0}, \tag{1.2}$$

where D is the diffusion coefficient, $\Delta\mathbf{r}$ is the vector displacement, and Δt is the observation time. Note that the observation time here is not the same as absolute time; it is an average calculated over multiple measurements for a fixed Δt window, but with a varying starting time. Equation 1.2 defines what is referred to as *'normal'* diffusion herein.

1.3.2 Anomalous diffusion

Anomalous diffusion describes random molecular motion that does not display a linear scaling of the second moment with time (whilst still maintaining a zero first moment). The most common model for anomalous diffusion is to allow the second moment to scale as a power of time [40, 41],

$$\left\langle \Delta r^2 \right\rangle = 4\Gamma\Delta t^{\alpha}, \tag{1.3}$$

where α is the anomalous exponent and D is replaced by Γ, an anomalous transport coefficient. Anomalous sub- and super-diffusion are defined by $\alpha < 1$ and $\alpha > 1$, and the special cases of $\alpha = 1$ and $\alpha = 0$ represent normal and confined diffusion. Given the form of Equation 1.3, α can be determined from the gradient of a logarithmic plot of $\langle \Delta r^2 \rangle / 4\Delta t$ *vs.* Δt.

The transport coefficient Γ is somewhat more difficult to interpret; as it has dimensions of [Length]^2/[Time], its dimensions are changing for different degrees of anomalous behaviour. This is further discussed in Chapter 4.

1.3.3 The importance of anomalous diffusion in biological membranes

In the preceding sections, it was noted that the complex nature of the bilayer has lead to many additions and extensions to membrane models over the last 40 years. In particular, the need to understand the anomalous behaviour first described by Saxton in 1994 [41], has lead to a sizeable body of work on this phenomenon *in vivo*

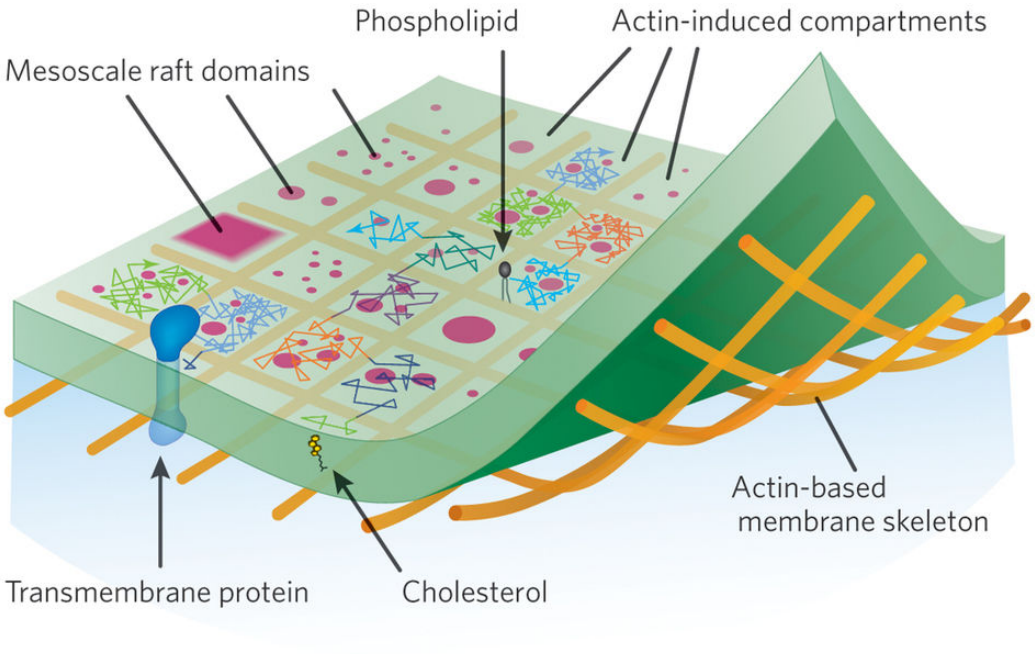

Figure 1.5: **Compartmentalisation of a cell membrane.** This schematic illustrates the complex nature of the cell membrane and highlights the components which act to compartmentalise it. Reproduced from [42].

[43, 44, 45]. Of note was the study of *'hop-diffusion'*, pioneered by Kusumi [46], which describes the anomalous motion and trapping of lipids [47, 48] and proteins [49], which is detected in many cell types. Further to this, because anomalous behaviour had been detected in both the inner and outer leaflets of the bilayer, Kusumi ameliorated the compartment model (illustrated in Figure 1.5) to include a *'picket fence'* theory [46]. Here, viscosity changes around cytoskeleton-associated proteins (pickets) directly anchored within the membrane account for locally hindered diffusion in both leaflets. The cytoskeleton has been implicated in causing anomalous behaviour by others using single particle tracking (SPT) methods [50, 51, 52]. Yet this is not the only contributing factor in cells.

Publication of further articles describing theory and modelling helped to assign and number of other factors as possible causes of anomalous behaviour in biological membranes. For example, obstacles (both mobile, immobile and fractal) [53, 54, 55], transient binding [52] and heterogeneous diffusion [56] are expected to contribute to the phenomenon. Particularly, simulations have been a vital part of this work with much of the early studies being completed by Saxton [41, 57, 58]. These Monte Carlo simulations described obstacles randomly placed on a lattice over which a tracer performs the random walk. Monte Carlo simulations of percolating geometries showed

ergodicity breaking for obstacle densities above the percolation threshold [59]. More recently, molecular dynamics simulations have probed the evolution of anomalous diffusion at short time scales (on the order of nanoseconds) [60, 61, 62, 63, 64].

Further to the *in silico* models, artificial lipid bilayers have played a key role in improving our understanding of anomalous diffusion. Within this research, anomalous behaviour of a number of lipids has been observed in supported lipid bilayers (further described in Section 1.4.2) by single particle [51], bulk methods [65], or both [66]. Membrane bound proteins at critical concentrations [67] and tracers undergoing confinement in domains [68, 69], also exhibit anomalous behaviour.

Importantly, work has also been undertaken which describes how to better interpret single particle tracking data [51, 70, 71] and provide methods to discriminate between classes of anomalous diffusion [72]. Schütz *et al.* described a probability based method of MSD analysis which better allows for analysis of SPT data were the population of diffusion particles comprises of two distinct species, usually one with a much lower diffusion coefficient than the other.

However, why and how anomalous diffusion exists in the plasma membrane remains a contentious issue. The production of artificial mimics of the complex membrane assembly, perhaps with the end goal being artificial cells, requires a fuller understanding of the way the membrane molecules move and interact. To this end, it is helpful to study anomalous diffusion first in more simple membranes (see Section 1.4), increasing complexity as the underlying mechanisms are understood. As well as platforms which exhibit anomalous behaviour, there is also a need for techniques and methods which reliably detect and interpret anomalous behaviours.

1.4 Artificial lipid bilayers

As mentioned above, cells as a whole can be too complex to study as many phenomena may interact or outcompete the feature one is interested in. Therefore, membrane models, or *artificial lipid bilayers*, have been an integral part of studies into membrane biophysics since the 1960s. There are a number of methods for making artificial membranes which have been extensively used and developed for this purpose. Some of these are discussed in this section.

1.4.1 Black Lipid Membranes, BLMs

The original artificial lipid bilayer platform was the *black lipid membrane* (BLM) conceived by Mueller in the 1960s [73]. As illustrated in Figure 1.6, the bilayer

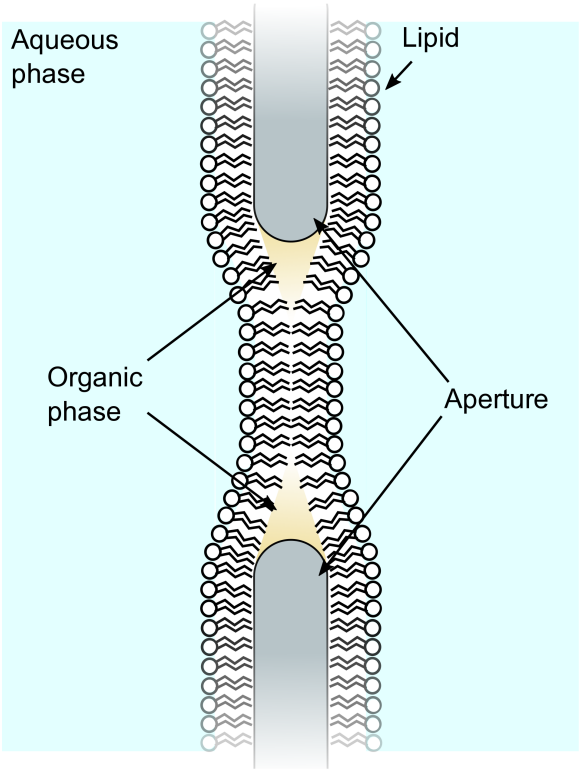

Figure 1.6: **Schematic of a black lipid membrane.**

is formed over a small aperture, usually tens of microns to a few millimetres in diameter. Lipid in an organic phase are *painted* over the aperture before hydration with aqueous phase. In the original method, relatively large regions of organic solvent were required to stabilise the membrane at the interface with substrate and some inevitably included in the tail region of the bilayer. This was implicated in the failure of some membrane proteins to insert into BLMs leading to developments by Montal [74] allowing formation of the membrane from an water/air interface thus removing the need for organic solvent. BLMs allowed access to both leaflets of the membrane and were commonly used for electrical measurements. The term *black lipid membrane* destructive interference from the two sides of the thin bilayer film resulting in a black appearance in reflected light microscopy [75].

1.4.2 Supported Lipid Bilayers, SLBs

Supported bilayers are produced at a surface by such techniques as Langmuir Blodgett deposition [76] or vesicular fusion [77] (as illustrated in Figure 1.7). In vesicle fusion, small unilamellar vesicle (SUVs) are prepared and added to a well on a very clean,

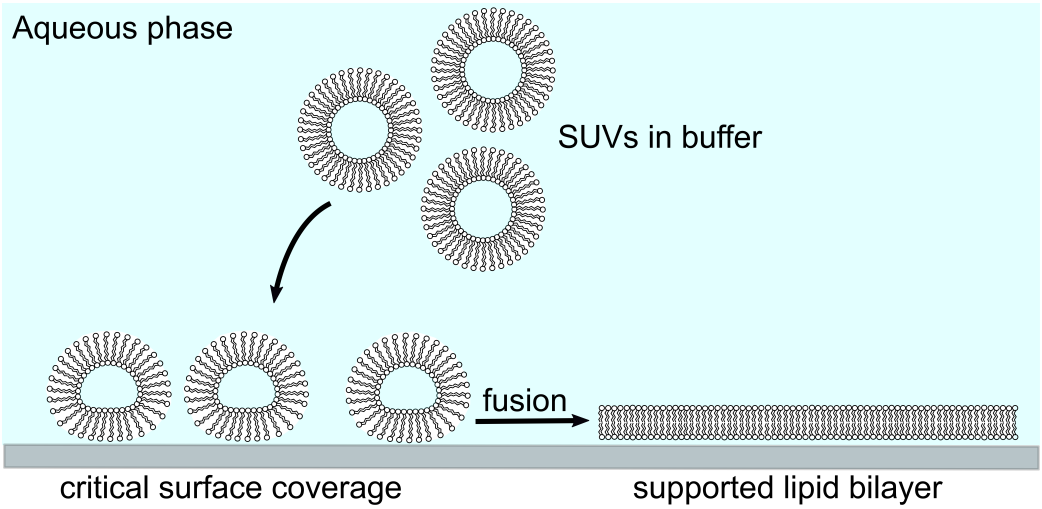

Figure 1.7: **Schematic of a SLB.** Formation of an SLB from SUVs via vesicle fusion.

smooth and hydrophilic surface (such as plasma cleaned glass or mica). The vesicles settle to the surface and at a critical coverage rupture to form a bilayer. This has been confirmed optically [78] and via quartz crystal microbalance dissipation (QCMD) measurements [77].

Although easy to form, there are questions around the impact of the surface on the behaviour of the bilayer and one side of the bilayer remains inaccessible to experimental manipulation. Unsupported techniques including floating [79] and tethered bilayers [80] overcome these issues allowing greater flexibility in the application of the bilayer. A floating bilayer is formed by three successive Langmuir-Blodgett depositions followed by a Langmuir-Schaeffer deposition. This results in two stacked bilayers where the membrane of interest is the upper-most and therefore not in contact with the solid substrate. For tethered bilayers, polymers are covalently attached to functionalised substrates which then provides a cushioning layer between the surface and the bilayer. In this technique, the lipids are also covalently attached to the polymer layer and therefore careful tuning of the pinning site density is required to ensure the bilayer is not perturbed too greatly. A similar method uses low concentrations of incorporated lipids with polymer modified head groups to provide the desired elevation from the substrate [81]. Here the polymer is adsorbed to the surface without covalent attachment. This method has found popularity in ensuring membrane proteins have sufficient space to reconstitute into supported lipid bilayers [82].

An alternative method used to prevent interactions with the underlying substrate is to form the SLB on mica [83]. Mica, immediately after cleavage, is atomically smooth and hydrophilic providing an ideal surface for bilayer formation.

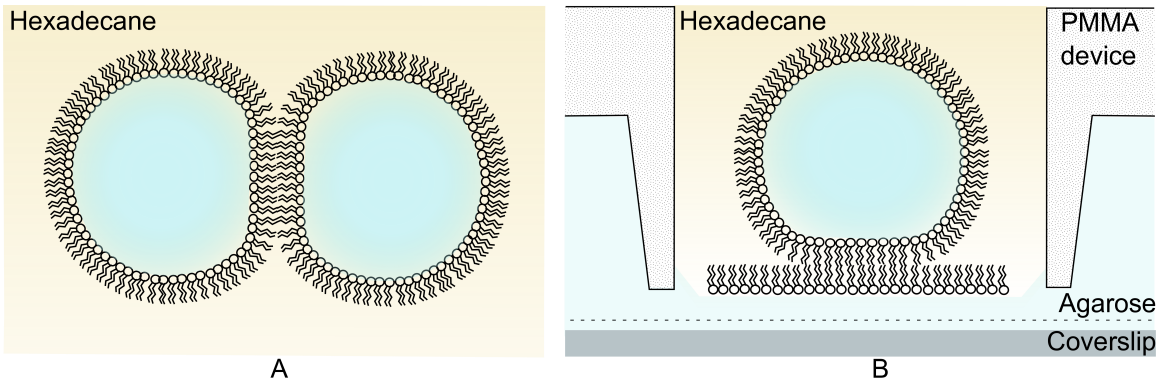

Figure 1.8: **Schematic of droplet interface bilayers. (A)** droplet-droplet type DIB and **(B)** droplet on hydrogel type DIB.

1.4.3 Droplet Interface Bilayers, DIBs

Notably, droplet interface bilayers (DIBs) have surfaced as a promising method for high throughput, reliable unsupported model membranes [84]. DIBs can be produced by two techniques, namely *lipid-in* and *lipid-out*. Both depend on the orientation of lipid molecules at the oil-water interface of mobile droplets to form a monolayer. Where two such monolayers are brought into contact, they spontaneously associate forming a bilayer. Much work has been completed on optimising the DIB protocols [85]. It was found that the synthetic lipid DPhPC (see Section 1.1, Figure 1.2) makes the most stable and usable DIBs.

The DIB platform can be further categorised into two distinct forms; the *droplet-droplet* (Figure 1.8A) and *droplet-hydrogel* (Figure 1.8B) type DIBs. Multiple droplets of type A, have been produced in microfluidic devices [86] and incorporated into networks [87] with the aim of developing protocells and tissues. The bilayer can then be manipulated mechanically [88, 89], electrically and via the injection of molecules, for example bio-relevant polymers [90], into one droplet. The ability to modulate the bilayer tension by mechanical manipulation of the droplet allows for mechanosensitive channels such as MscL to be studied [91]. With the insertion of electrodes into the droplets, electrophysiology can be used to study the membrane as one would with a whole cell.

The droplet-hydrogel type are produced within a PMMA device, from one monolayer coated droplet and one monolayer formed on an agarose surface (see Section 2 for method details). Bilayers within these devices can also be probed electrically but unlike the droplet-droplet type, they are more easily accessible to optical microscopy using inverted microscopes. The hydrogel support not only produces means of incorporating proteins from the lower leaflet, but also provides a cushion which can be

hydrated to ensure membrane protein mobility. Thus far, this technique has been used extensively for the study of α-hemolysin a prototype pore forming protein, as well as other biologically relevant molecules [84] and phenomena, including electroporation [92], transient phase separation [29] and DNA sequencing via optical methods [93].

1.5 Techniques for studying diffusion in model membrane systems

A number of techniques are popular for the study of diffusion in membranes. These can be broadly categorised as bulk techniques and single particle techniques [94]. The latter is favoured since, as outlined in Section 1.2, the membrane is heterogeneous so averaging over bulk properties can mask some intricacies in the behaviour. Here, single molecule optical methods relevant to this work are described.

1.5.1 Total Internal Reflection Fluorescence, TIRF

TIRF microscopy (TIRFM) is a well established microscopy technique which is widely used in membrane biophysics and cell biology.

1.5.1.1 Total Internal Reflection, TIR

Incident light is totally internally reflected at the interface between media of different refractive indices, n_1 and n_2, if the angle of incidence, θ, is greater than the critical angle, θ_c (Snell's Law, Equation 1.4).

$$\theta_c = \sin^{-1} \frac{n_2}{n_1} \tag{1.4}$$

The principal of using totally internally reflected light to illuminate a sample was first described by Ambrose in 1956 [95]. Here, a prism was used to refract a mercury arc lamp beam at the interface between the prism and a microscope slide optically connected my immersion oil. The light totally internally reflects yet a small amount penetrates the sample and is scattered by the cell surface in close contact with the microscope slide. This scattered light was collected from above using a microscope objective (Figure 1.9).

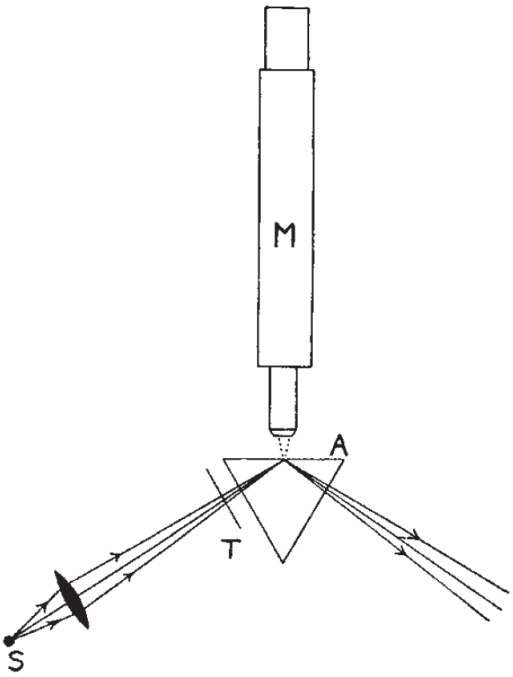

Figure 1.9: **Scheme of early TIRF microscopy.** Source (**S**) passes through a slit (**T**) such that it is focussed at the top surface (**A**) of a 60° prism. Scattered light from a sample places at this surface is collected by the microscope (**M**). Reproduced from [95].

1.5.1.2 Evanescent fields for fluorescence microscopy

In 1982, Axelrod [96] further developed the TIR technique such that the incident light is used to selectively excite fluorophores only within a small depth of the sample. This is owing to the production of an exponentially decaying evanescent field parallel to the imaging plane (z direction) whose intensity ($I(z)$) is expressed as:

$$I(z) = I_0 e^{\frac{-z}{d}} \tag{1.5}$$

The depth of propagation (d) of this wave can be calculated from Equation 1.6 where λ_0 is the wavelength of light which is incident at angle θ.

$$d = \frac{\lambda_0}{4\pi\sqrt{n_1^2 \sin^2\theta - n_2^2}} \tag{1.6}$$

For a typical experiment where n_1 is 1.52, the refractive index of a coverslip, and n_2 is 1.38, the refractive index of cytosol [97], Equations 1.4 and 1.6 can be used to assert that, for visible light, the evanescent field does not penetrate more than 100 nm above the interface. Therefore, the fluorescence collected is not compromised

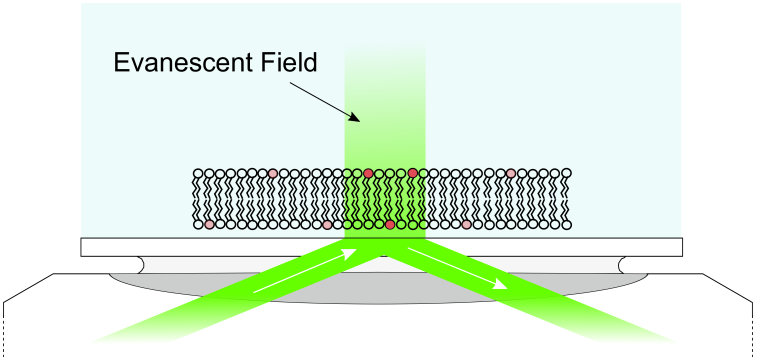

Figure 1.10: **Scheme of a single molecule TIRFM experiment.** The evanescent field illuminates a small number of fluorophores in the sample.

by signal from out of focus objects further within the sample. This makes TIRFM particularly useful for the study of single molecule events at membranes of adherent cells and coverslip supported lipid bilayers as illustrated in Figure 1.10.

Wider usage of TIRFM stemmed from the development of commercial objective-type TIRF in which the incident light is refracted from within the microscope objective which therefore both illuminates the sample and detects the fluorescence signal [98]. Such a set-up was used for the experiments detailed in the following chapters and is described in Section 2.3.1.

1.5.2 Interferometric Scattering, iSCAT

It is advantageous to detect scattering rather than fluorescence because, in theory, the scattered signal is only limited by the incident laser power and is not subject to photophysical effects such as photoblinking or photobleaching. These limit the accessible time resolution of fluorescence, which is not a problem for scattering. In experiments analogous to TIRF, it is possible to use both prism and objective type TIR to detect light scattered from the sample [99].

Scattering amplitude, $s(\lambda)$ can be calculated as:

$$s(\lambda) = \eta\alpha(\lambda) = \eta\epsilon_1(\lambda)\pi\frac{d^3(\epsilon_2(\lambda) - \epsilon_1(\lambda))}{2(\epsilon_2(\lambda) + 2\epsilon_1(\lambda))} \tag{1.7}$$

where α is the polarisibilty of the particle, η a detection efficiency parameter related to the set-up used, ϵ_1 and ϵ_2 are the complex dielectric constants of the medium and particle respectively and d is the diameter of the particle.

The detected signal in such experiments is a combination of background intensity, I_r (usually reflected light) and scattered intensity, I_s as follows:

$$I_{det} = I_r + I_s = (E_r + E_s)^2 = E_I^2(r^2 + s^2 - 2|rs| \sin \phi) \tag{1.8}$$

where E_I^2 is the incident field, E_r and E_s are the reflected and scattered fields respectively, r^2 the pure reflected term and s^2 the pure scattering term.

The scattering amplitude of nanosize objects is very small and can be hidden beneath spurious reflections and background signal. Considering both Equations 1.7 and 1.8, it can be seen that the pure scattering term scales with d^6 causing this signal to diminish quickly as particle size decreases. Therefore, in practice, dark field type microscopy, in which the incident light, reflections and stray light are excluded from the detector, is necessary to ensure the pure scattering signal is detectable. Even with this, it is most common to detect nanoparticles using dark field microscopy due to their larger scattering cross-section and contrast enhancement via plasmon resonance [100]. Dark field microscopy is still being optimised and remains an important technique particularly for imaging on nanoparticles within cells [101].

Interferometry was acknowledged as a way to ensure more detectable signals from such experiments. It can be seen from Equation 1.8 that the cross-term, $2|rs| \sin \phi$, utilises the large reflected signal to return a detectable signal which scales with d^3, thus, diminishing at a slower rate than the pure scattering signal.

Reflectance interference contrast microscopy (RICM sometimes referred to as ICM and IRM) is a technique first developed in 1964 by Curtis [103] in which the interference between light reflected from multiple interfaces is detected (Figure 1.11). RICM was developed with the study of live cells in mind [103] and was used extensively to image the 3D morphology of cells adhered to a surface (before the emergence of superresolution techniques) [102, 104].The reflected light from the adhered membrane interferes with the light reflected from the coverslip support. The difference in refractive indices is sufficient to produce good contrast, with thee interference pattern interpreted to give size and positional information about the scattering object.

The antiflex technique (Figure 1.12) was developed as a method to enhance the contrast by reducing stray light [105]. A quarter wave plate, polarising beam splitter and polarizers are introduced to select signals which undergo a change in polarisation upon reflection. If these optics can be introduced above the objective then this would reject any reflections from the internal optics and back apperture which can account

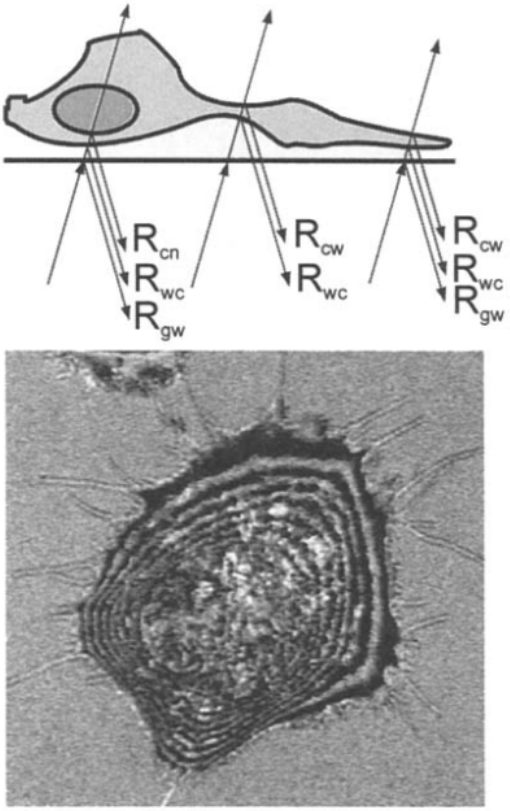

Figure 1.11: **RICM of a cell.** Various reflections interfere to produce an image of the cell. c, cytoplasm; n, nucleus; w, water; g, glass. Reproduced from [102].

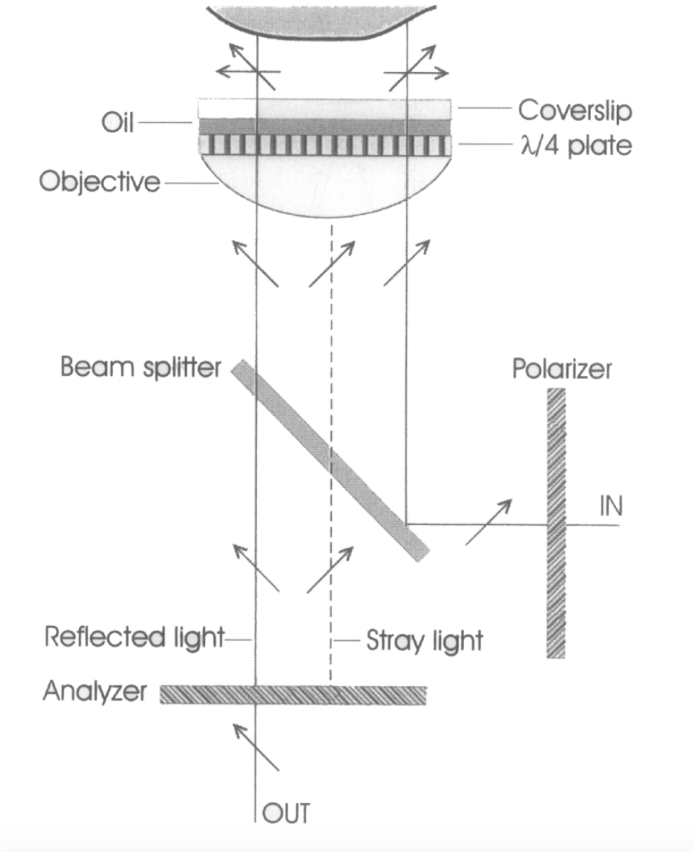

Figure 1.12: **Scheme of the antiflex technique.** Stray light, often from reflections within the objective, is excluded from the detector by the addition of a quarter wave plate. The quarter wave plate transforms plane polarised light into circularly polarised light which changes rotation during reflection from the sample. The returning light has opposite polarisation and is therefore separated from the incoming light towards the detector. Reproduced from [102].

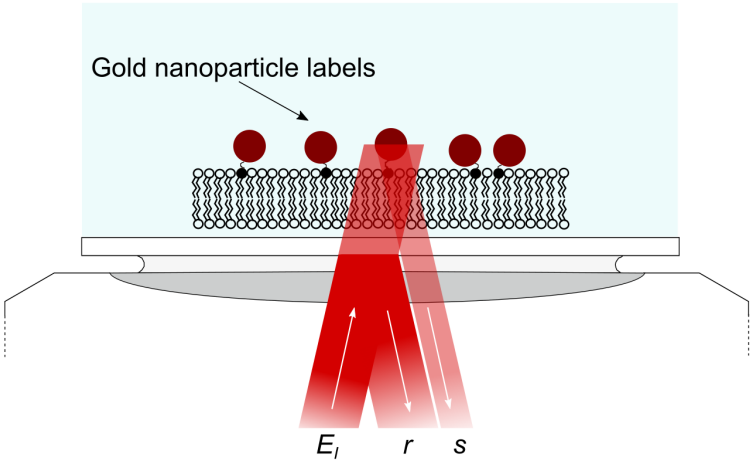

Figure 1.13: **Scheme of a single molecule iSCAT experiment.** The incident field E_i is reflected from the coverslip interface (r) and scattered from gold particles conjugated to the bilayer (s).

for 0.1 % of the incident light [99]. However, in most configurations this is not possible owing to the working distance of the objectives used for single particle tracking.

The RICM concept reemerged in 2004 [106] and was developed as interferometric scattering microscopy (iSCAT) in the lab of Vahid Sandoghdar [107]. If one again considers Equation 1.8 and assumes that the pure scattering term s^2 diminishes for particles $\leq$ 40 nm, the detected intensity becomes:

$$I_{det} = I_r + I_s = (E_r + E_s)^2 = E_I^2(r^2 - 2|rs|\sin\phi) \tag{1.9}$$

The contrast of images detected in this way is calculated as:

$$\begin{aligned} C &= \frac{I_{det}}{I_r} \\ &= 1 - \frac{2|rs|\sin\phi}{r} \end{aligned} \tag{1.10}$$

This illustrates the dependance of the detected signal on the strength of the incident field and the ability to normalise images produced with a constant background signal. These factors increase the sensitivity of the technique allowing for detection of smaller particles including the potential for label free detection of individual proteins [99].

Use of the iSCAT technique for the detection of gold nanoparticles has thus far elucidated lipid dynamics in membranes [108], including within phase separated compositions [69, 109] and in platforms exhibiting anomalous behaviour [68, 110]. In

a recent collection of work, Andrecka *et al.* have used nanoparticles conjugated to myosin-5a molecules to observe the classical 'myosin walk' upon actin filaments and dynein upon microtubules [111, 112]. Although particles of 20- 40 nm diameter are most commonly used, particles down to 5 nm have been detected [107]. As with pure scattering techniques there is also the potential to exploit the plasmon resonance of these particles to enhance contrast [99].

The label free imaging of molecules is highly desirable owing to the unperturbed nature of any dynamic or functional measurements. Label free imaging of larger objects such as whole cells [113], bilayer edges [78], micron scale phase separation [29] and macromolecules including microtubules [114], are fairly facile using iSCAT. However, highly sensitive iSCAT instruments have also allowed for the detection of single virions label free [115, 116] as well as the imaging of single proteins at the coverslip interface [117, 118]. The difficulty lies in imaging such low contrast objects within or associated to the membrane. Owing to the close refractive indices of proteins and membrane the contrast is very low. Such imaging is not impossible however as de Wit *et al.* proved by imaging highly dynamic nanoscale lipid domains within a DIB label free [29]. The contrast here was on the order of 1 to 2 % and to ensure sufficient signal to noise, requires background signal suppression to less than 0.1 % [99].

Label free iSCAT imaging of particular note includes detection of proteins secreted from live cells [119]. In this work, cells from an Epstein-Barr virus (EBV)-transformed B cell line, Laz388, were monitored at the coverslip interface using iSCAT. The cell itself exhibited high contrast, yet within the vicinity single proteins of 100-1100 kDa were also detected with 0.03-0.3 % contrast. This illustrates the potential of iSCAT to be used in sensing platforms [120, 121, 122] and to monitor reactions [123].

A further advantage of interferometric detection is the ability to gain positional information in 3D [124]. The phase term ϕ in Equation 1.8, is a complex factor accounting for the Gouy phase (ϕ_{Gouy}) but also importantly, phase changes caused by a difference in path length of the scattered and reflected light [99]. Considering the phase as a function of the distance between the reflecting interface and the particle, $\phi(z)$ can be expressed as:

$$\phi(z) = \phi_{Gouy} + \phi_{scat} + \frac{4\pi z n}{\lambda} \tag{1.11}$$

where n is the refractive index of the surrounding medium, ϕ_{scat} the scattering phase and λ the illumination wavelength.

Thus, for a particle moving relative to a fixed reflecting interface, the contrast varies as $\sin\phi(z)$ allowing z to be calculated. This has been useful for tracking the rotation of particles [111, 116] and the motion of proteins associated with the membrane of a giant unilamellar vesicle [108]. To obtain such information from fluorescence, more complex set-ups and techniques such as confocal sectioning and lattice light sheet microscopies are required, while for iSCAT, 3D information requires calibration and careful analysis.

As iSCAT microscopes are not yet commercially available, small variations exist in many of the instruments used in the research mentioned above. Simultaneous iSCAT and fluorescence [125] is particularly popular as these platforms allow for the direct comparison of traditional TIRF images with iSCAT. Bulk fluorescence can be used to locate an area of interest before using iSCAT to probe single molecules over long timescales, which would not be possible using fluorescence due to photobleaching. iSCAT has also been combined with raman [126], dark field imaging [127] and STED-FCS techniques [128].

There are however, a number of limitations to the iSCAT technique. Of greatest significance is the background signal often caused by stray light, reflections and optical aberrations. As mentioned, very low noise is required to detect low contrast objects such as single proteins. Scanning the incident beam can control the spatial coherence of the illumination fields making normalisation more effective. To achieve this, acoustooptic deflectors can be employed but these results in around an order of magnitude loss in intensity (via undesired diffraction) which must also be accounted for. Increasing incident laser power to improve contrast also risks damage to samples as local heating becomes more significant. To account for this, longer wavelengths (particularly red light) can be used.Some of these limitations are further discussed in Chapter 3. There, the development of an iSCAT microscope for high speed single particle tracking is also described. The applications of this microscope in the study of anomalous diffusion are then illustrated in results Chapters 4, 5 and 6.

Chapter 2

General Methods

This chapter details the materials used and the general methods relevant to the presented work. The two main microscopy techniques, TIRF and iSCAT, are described along with the two main bilayer platforms, SLBs and DIBs. Further methods relevant to only parts of this thesis can be found at the start of the relevant chapters. Concluding this chapter is a description of the single particle tracking methods used.

2.1 Materials

Unless otherwise stated, all chemicals and solvents were of analytical grade and used without further purification.

2.1.1 Lipids

1,2-Dioleoyl-*sn*-glycero-3-phosphocholine (DOPC), 1,2-diphytanoyl-*sn*-glycero-3- phosphocholine (DPhPC) and 1,2-dioleoyl-*sn*-glycero-3-phosphoethanolamine-N-cap-biotinyl (biotin-DOPE) were purchased from Avanti Polar Lipids (Alabaster, USA). Texas Red™1,2-dihexadecanoyl-*sn*-glycero-3-phosphoethanolamine triethylammonium (TR-DHPE) and 1,2-dipalmitoyl-*sn*-glycero-3-phosphoethanolamine-N-[methoxy(polyethylene glycol) - 1000/2000/5000] ammonium salt (PEG(1K)/(2K)/(5K)-DPPE) were purchased from Invitrogen (Eugene, USA). Atto-488-1,2-dioleoyl-*sn*-glycero-3-phosphoethanolamine (Atto488-DOPE) was purchased from ATTO-TEC, (Siegen, Germany).

Lipids were dissolved in a mixture of 9:1 chloroform:methanol to 50 mg ml^{-1} and stored at -20°C for up to one month during use. Single molecule dilutions at 1 µg ml^{-1} in the same solvent were prepared from the TR-DHPE and biotin-DOPE 50 mg ml^{-1} stocks. Bulk DOPC and single molecule stocks were used to prepare the lipid mixtures detailed below.

2.1.2 Nanoparticles

Goat antibiotin-conjugated 20 and 40 nm gold nanoparticles (OD10 suspensions) were purchased from BBI (Cardiff, UK). Streptavidin-conjugated 10 and 100 nm gold nanoparticles (OD3 suspensions) were purchased from Stratech Scientific (Newmarket, UK).

2.1.3 Other materials

Chloroform, propan-2-ol and methanol (all HPLC grade) were purchased from Sigma-Aldrich (St. Louis, USA). Standard phosphate-buffered saline tablets (P4417), hexadecane (296317) and silicone oil AR 20 (10836) were also purchased from Sigma-Aldrich. Herein, *water* refers to 18.2 MΩ cm (25°C) water (Direct-Q 3 UV, Merck Millipore, Billerica, USA) used to prepare all solutions. PBS at pH 7.0 was prepared from one tablet in 200 ml of water and is referred to as *buffer*. DECON-90 surfactant was purchased from VWR International (Lutterworth, UK).

2.1.4 Microscopy materials

Glass coverslips (Menzel Glaser #1) were purchased from VWR International (Lutterworth, UK) and were cleaned as detailed in the following protocols. Immersol 518-F objective immersion oil was also purchased from VWR.

2.2 Model membrane platforms

2.2.1 SLBs

SLBs were prepared on glass coverslips by vesicle fusion [129] from SUVs of 1 mg ml^{-1} DOPC with <0.001 mol% each TR-DHPE and biotin-DOPE unless detailed otherwise.

Lipid mixtures were dried under nitrogen and placed under vacuum overnight. The dried lipids were hydrated in water and vortexed before tip sonication (Vibracell VCX130PB with CV188 tip, Sonics & Materials, Newtown, USA) for 15 minutes at 25% amplitude. The resulting clear vesicle suspension was centrifuged (3 minutes; 14000g) before the supernatant was separated from any titanium residue and retained. SUV preparations were stored at 4°C for up to 48 hours.

Glass coverslips were rigorously cleaned using stepwise bath sonication with DECON-90, water, and propan-2-ol for 20 minutes in each. Immediately before use, the glass

was dried under nitrogen and cleaned with oxygen plasma for 3 minutes (Femto, Diener Electronic, Ebhausen, Germany). A well was created on each coverslip using vacuum grease (Dow Corning high vacuum grease, VWR). 50 µl of SUV stock were diluted 1:1 in buffer (PBS pH 7 unless otherwise stated) and added to the chamber immediately. The vesicles were incubated for 60 minutes and the resultant membranes were washed thoroughly with degassed water followed by buffer.

2.2.2 DIBs

DIBs were prepared following the protocol outline in Leptihn *et al.* 2013 [85]. Both *lipid-in* and *lipid-out* methods were used as specified in the following chapters.

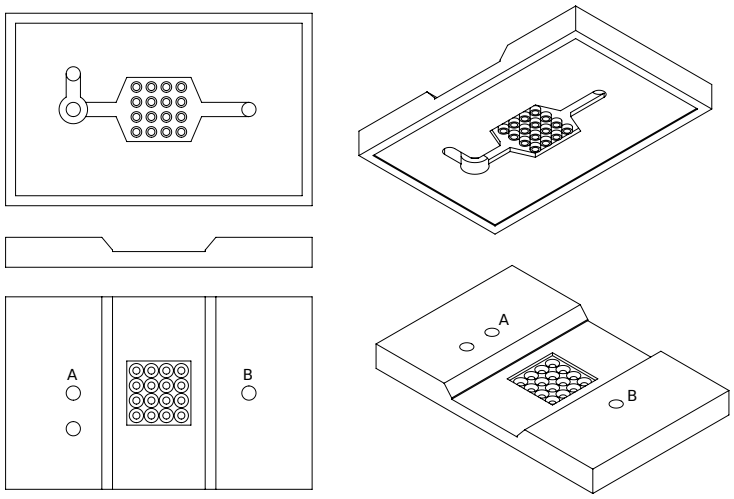

Figure 2.1: **Schematic of a DIB custom device.** Views are shown from the bottom face (to which the coverslip is fixed), the side and from the top face. the rehydration agarose is pipetted into the hole **A** and allowed to flow through to **B**. Droplets are added to the 16 wells in the centre of the device.

Preparation of the device platform (Figure 2.1) is common to both methods. Spin coat agarose was prepared by dissolving ultra-low melt agarose (Sigma Aldrich, A2576) to 0.75 wt% in water. Rehydration agarose was prepared by dissolving low melt agarose (Sigma Aldrich, A9539) to 2.8 wt% in buffer. The appropriate amount of DPhPC chloroform stock was pipetted into a clean, 1.5 ml glass vial. The lipid was dried under nitrogen and left under vacuum over night. The lipid film was resuspended in a mixture of of 9:1 hexadecane:silicone oil to a final lipid concentration of 8.9 mg ml^{-1}. A coverslip cleaned with oxygen plasma for 3 minutes, was fitted on a spin coater (WS-650MZ-23NPPB, Laurell Technologies, North Wales, USA), loaded with 140 µl

of spin coat agarose and spun at 3000 rpm for 30 seconds. The coated coverslip was fixed to the bottom surface of a custom microfabricated PMMA device (Figure 2.1) and filled with 170 µl of rehydration agarose via well A, such that it flowed through to well B. The filling wells A&B were sealed with tape and DPhPC in oil solution was immediately added to the sixteen small wells in the centre of the device and left to incubate at room temperature for 20 minutes.

Droplets produced by either the *lipid-out* or *lipid-in* methods detailed below were then added to the small wells in the PMMA device and left for 10 minutes to allow bilayer formation before imaging.

2.2.2.1 Lipid-in droplet preparation

SUVs were prepared as described above (Section 2.2.1) from 1 mg ml^{-1} DPhPC and <0.001 mol% TR-DHPE and diluted with buffer to a final concentration of 0.5 mg ml^{-1}. 100 nl droplets of SUV solution were pipetted into a microfabricated tank containing hexadecane and incubated for 40 minutes.

2.2.2.2 Lipid-out droplet preparation

Gold nanoparticle stocks were diluted 1:100 in buffer. An amount of DPhPC with <0.001 mol% biotin-DOPE was dried in a 1.5 ml clean, glass vial from stock solution and resuspended in the appropriate volume of 9:1 hexadecane:silicone oil for a final concentration of 8.9 mg ml^{-1}. 100 nl droplets of nanoparticle solution were pipetted into a microfabricated tank containing the lipid-oil mixture and incubated for 40 minutes.

2.3 Microscopy

2.3.1 Single molecule TIRF experiment

An Eclipse TiE inverted microscope (Nikon, Tokyo, Japan) was used for the single molecule experiments detailed in the following chapters. The particulars of the set-up are schematically represented in Figure 2.2.

For the detection of single molecules, an SLB was prepared as outlined above and mounted on the microscope. A 532 nm continuous-wave laser was focussed at the back aperture of the objective lens (60 × TIRF oil-immersion NA 1.49, Nikon, ∼1.4 kW cm^{-2}) such that total internal reflection occurred. TR-DHPE is excited and fluoresces with peak intensity at 615 nm (orange/red) which is transmitted through

bandpass filters before being imaged on an EM-CCD with 280 EM gain. Up to 2000 frames were collected at 200 Hz (5 ms exposure time) and saved in Tagged Image File (TIF) format for tracking as detailed below in Section 2.4.1.

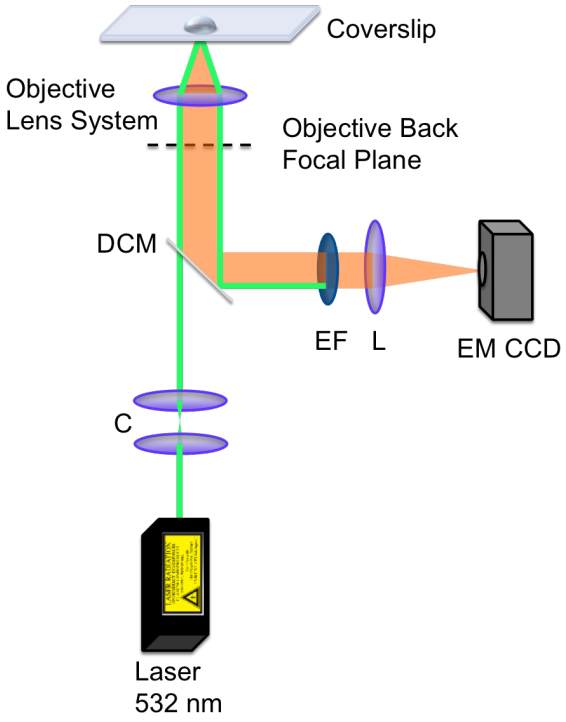

Figure 2.2: **Scheme of a TIRF microscope.** (**C**) collimation, (**DCM**) dichroic mirror 532 nm long-pass ZT532rdc (Chroma, Bellows Falls, USA), (**EF**) emission filter 605/55 nm (Semrock, Rochester, USA), (**L**) lens, (**EM CCD**) electron-multiplying CCD (iXon+ 860; Andor). Laser light (green) is focussed at the back focal plane of an objective such that, at the coverslip, the beam is above the critical angle and therefore totally internally reflects. Fluorescence (orange) returns through the objective and is sent to a detector.

2.3.2 iSCAT

A custom-built iSCAT microscope with simultaneous TIRF imaging was built following previously described principles [116, 125] and is schematically represented in Figure 2.3.

For iSCAT imaging, a 639 nm laser beam (Toptica, Munich, Germany) was collimated and reduced to 2 mm beam diameter before being passed through two acoustooptic deflectors (AODs) (Gooch and Housego, Ilminster, UK). The beam was scanned with 200 mV sawtooth waveform voltages in the x and y directions by separate phase-locked function generators (DG 1022, Rigol, Reading, UK) at 79 and 80 kHz, respectively resulting in an even square of illumination. The deflected beam was

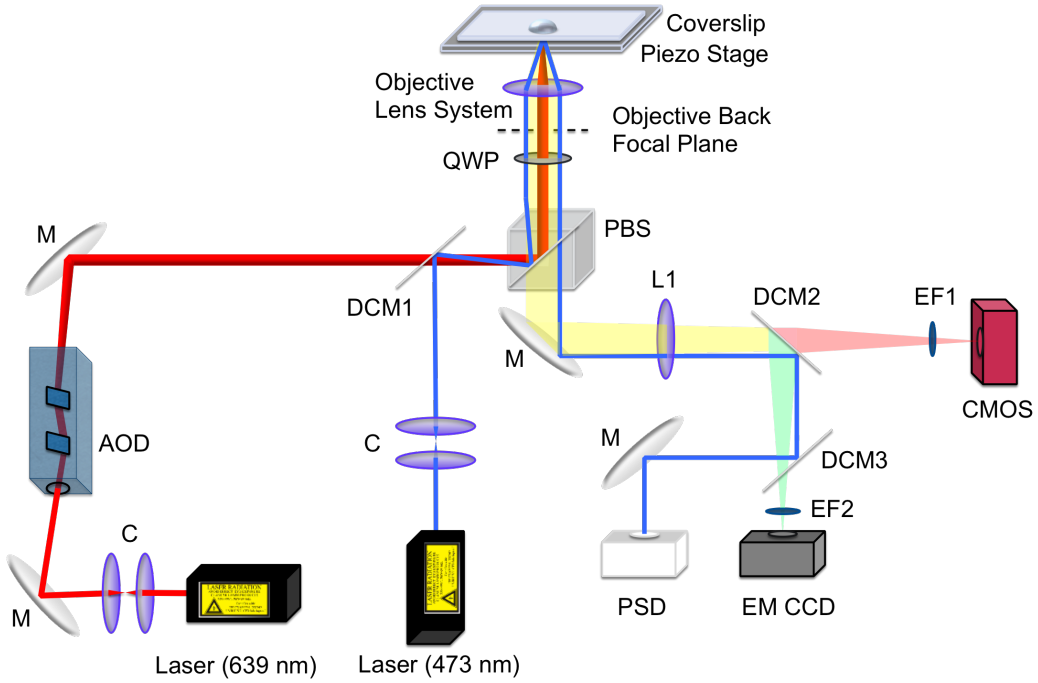

Figure 2.3: **Scheme of an iSCAT microscope.** (**AOD**) acousto-optic deflector, (**C**) collimation, (**CMOS**) Photonfocus camera, (**DCM**) dichroic mirror, (**EF**) emission filter, (**EM CCD**) Andor iXon3, (**L**) lens 200 mm, (**M**) mirror, (**PBS**) polarising beam splitter, (**PSD**) position sensitive diode, (**QWP**) quarter wave plate. The objective lens system is represented by one lens but in practice is a compound assembly of multiple lenses. Yellow represents a common path between iSCAT (red) and fluorescence (green).

directed through a polarising beam splitter and quarter wave plate (both Thorlabs, Newton, USA) before being focussed at the back aperture of an objective lens (60× oil immersion, NA 1.49). This light is focussed at the sample by the objective, reflected from the coverslip interface, and scattered from the object of interest (as illustrated in 1.13). The resultant is returned with opposite polarisation and therefore passes through the beam splitter to the emission path. L1 (200 mm) focusses the output fields at the three detectors. Fluorescence and iSCAT image signals are separated by DCM 2 (605 Edge Brightline, Semrock). The transmitted iSCAT signal with overall magnification of 174 × was passed thorough an emission filter, EF1 (640/14, Semrock) and imaged onto a CMOS camera (MV-D1024-160-CL-8, Photonfocus, Lachen, Switzerland).

To aid in locating areas of interest for iSCAT, simultaneous TIRF imaging with bulk levels of fluorophore was used. The basic principles of this TIRF imaging are the same as Section 2.3.1 except 473 nm laser light (blue) (SDL-473-LN-100T, Shanghai Dream Lasers, Shanghai, China) is incident on the sample exciting Atto488-DHPE

which fluoresces with peak intensity at 520 nm (green). The excitation paths are combined by dichroic mirror DCM1 (506 Edge Brightline, Semrock). The reflected 473 nm light and fluorescence were separated by DCM 3 (506 Edge Brightline, Semrock). Fluorescence passed through EF2 (550/88, Semrock) and imaged onto an EM-CCD (iXon3, Andor) whilst the returned laser was imaged onto a position sensitive photodiode as part of a feedback mechanism.

2.3.2.1 Image acquisition

To track AuNP-labelled lipids, a SLB was formed as described above and 5 μL of a suspension of OD10 40 nm gold nanoparticles were added to the volume of buffer above the bilayer. After 30 minutes incubation, the SLB was washed thoroughly with buffer to remove unbound nanoparticles before imaging. The live image feed on the program Labview was used to focus the particles before image stacks of 1000 frames (TIF format) were recorded at 50 Hz (20 ms exposure) unless otherwise stated.

2.3.2.2 Background subtraction

Image stacks were processed using the free software ImageJ. The macro used can be found in Appendix B.2. The background image was produced by 'flattening' the stack into a median-value projection. This method produces a sufficiently flat field if the objects of interest move over the course of the stack as these do not significantly alter the median pixel intensity values. For static objects, the background image was obtained from stacks recorded as the stage was translated manually, or from a stack recorded in an representative area of the sample containing no nanoparticles. Unless otherwise stated, the background image was produced from a stack containing nanoparticles which diffuse sufficiently to be averaged out. The image stack was then divided by the background image to produce a normalised stack.

2.4 Single Particle Tracking, SPT

Once an image stack of bright particles on a flat, dark background has seen prepared, the tracking process using TrackMate is the same for fluorescence and iSCAT data except where threshold and linking distances vary. The spot locations can be used for a number of useful analyses including for the calculation of SNR and diffusion coefficients.

2.4.1 TrackMate

TrackMate is an open source plugin for ImageJ [130]. The parameters *'estimated spot diameter'* and *'threshold'* were entered by the user and were used to detect particles in each frame using a Laplacian of Gaussian (LoG) filter. Tracks were generated by linking these detected spots together using a simple linear assignment problem (LAP) tracker which minimises the sum of square distances between particles to predict connected detections. The output from this was a collection of tracks containing space-time co-ordinates of each point in the track in XML format for analysis in MATLAB.

2.4.2 Contrast and signal to noise analysis

As outlined in Equation 1.10, the contrast can be reported as the peak intensity of a background normalised image. In ImageJ, a line profile is taken across the centre of the spot and pixel intensities listed. Theses intensities were multiplied by 100 to give percentage contrast before being graphed in Igor and subject to a 1D gaussian fit of the form:

$$f(x,y) = y_0 + A\exp\left(-\left(\frac{x-x_0}{width}\right)^2\right) \tag{2.1}$$

Contrast was reported as the peak amplitude A. Signal to noise ratio (SNR) can be calculated as follows:

$$SNR = \frac{A}{\sigma_{y_0}} \tag{2.2}$$

To reduce the number of manual operations, a custom MATLAB script (Appendix B.3.2) was written to extract the contrast and SNR from spots detected using TrackMate. The XML file containing x and y spot localisations was read into a matrix in MATLAB. The code performed one of three analyses to extract the spot intensity:

1. *Pixel intensity*; the intensity of the pixel localised by the XML co-ordinates is reported for each spot.

2. *Average*; a kernel of defined size is produced around the pixel localised by the XML co-ordinates and intensity is averaged within this kernel and reported.

3. *Gaussian fit*; a grid size is defined around the pixel localised by the XML coordinates over which a 2D gaussian fit is performed and parameters iterated to minimise the sum of square errors. The amplitude of the gaussian and fit error are reported.

For the cases *pixel intensity* and *average*, no error (σ_{y_0}) was reported so the standard deviation of the image was found in ImageJ. The maximum pixel intensity or average intensity were then divided by this number to calculate SNR.
For 2D gaussian fitting the function takes the form:

$$f(x,y) = A\exp\left[\frac{-1}{2(1-c^2)}\left((\frac{x-x_0}{\sigma_x})^2 + (\frac{y-y_0}{\sigma_y})^2 - \frac{2c(x-x_0)(y-y_0)}{\sigma_x\sigma_y}\right)\right] \quad (2.3)$$

Again, contrast was reported as the amplitude of the fit and SNR was calculated as the amplitude divided by the sum of squared errors. Full code can be found in Appendix B.

2.4.3 Diffusion analysis

Further to the contrast analysis, the XML track output was used to perform diffusion analysis. This data was subsequently used to obtain mean-squared displacements for different observation times, which in turn were used to obtain diffusivity values according to the random walk model of diffusion as in Equation 1.2.

2.4.3.1 MSD calculation

The displacements in x and y for a fixed time lag (observation time) Δt were calculated as:

$$\begin{aligned} \Delta x_i(\Delta t) &= (x_{i+1} - x_i) \\ \Delta y_i(\Delta t) &= (y_{i+1} - y_i) \end{aligned} \quad (2.4)$$

where i is the index of any frame in the image stack.

$$\Delta \mathbf{r}_i = \Delta x_i(\Delta t) + \Delta y_i(\Delta t) \quad (2.5)$$

The first moments defined by Equation 2.5, were squared to obtain the square displacement $\Delta \mathbf{r}^2$. The displacement and the square displacement were calculated along

every track for varying values of the time lag Δt. The mean square displacement was calculated as the average of all steps corresponding to a single lag time:

$$\left\langle (\Delta r(\Delta t))^2 \right\rangle = \frac{1}{n} \sum_{i=1}^{n} \Delta r_i^2(\Delta t) \tag{2.6}$$

2.4.3.2 $\langle \Delta r^2 \rangle (4\Delta t)^{-1}$ *vs.* Δt plots

The data were plotted as $\langle \Delta r^2 \rangle (4\Delta t)^{-1}$ *vs.* Δt on logarithmic axes. Because Δr^2 varies linearly with time in normal diffusion (Figure 2.4A, black), it appears as a horizontal line in Figure 2.4B (black). However, in anomalous subdiffusion (blue) Δr^2 deviates and appears as a curve with a negative gradient in Figure 2.4B.

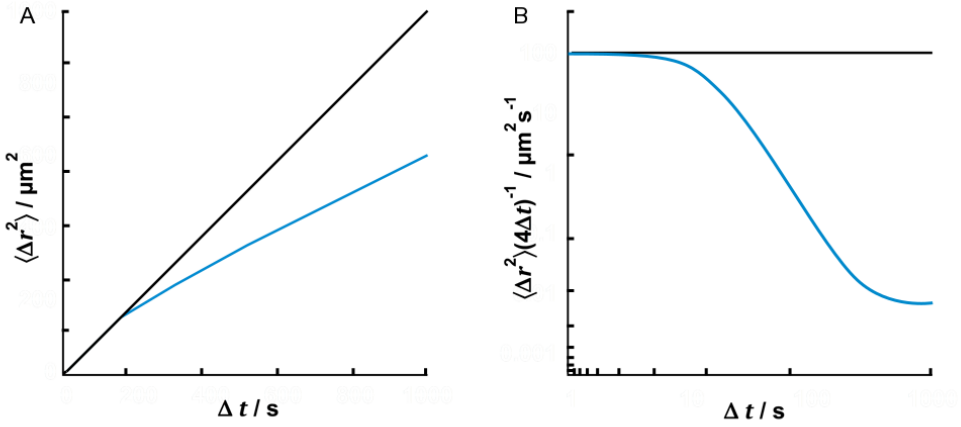

Figure 2.4: **Schematics of second moment and $\langle \Delta r^2 \rangle (4\Delta t)^{-1}$ *vs.* Δt plots.** (**A**) Variation of MSD *vs.* Δt for normal behaviour (black) and subdiffusion (blue). (**B**) Schematic $\langle \Delta r^2 \rangle (4\Delta t)^{-1}$ *vs.* Δt plot on logarithmic axes where normal behaviour (black) is a horizontal line while anomalous subdiffusion (blue) exhibits a transition to negative slope.

2.4.3.3 Extraction of the anomalous exponent (α) and anomalous transport coefficient (Γ)

Logarithmic treatment of the data and transfer to linear axes, gives access to the transport coefficient Γ and anomalous exponent α as outline in Equation 2.7.

$$\log\left(\left\langle \Delta r^2 \right\rangle (4\Delta t)^{-1}\right) = (\alpha - 1)\log \Delta t + \log \Gamma \tag{2.7}$$

The data were graphed in Igor and subjected to linear fits weighted by the errors from the diffusion analysis. α is given by addition of 1 to the gradient of the fit, with

the error in α being quoted as error of this fit parameter. The intercept of the fit is equal to $log_{10}\Gamma$ and thus Γ is calculated by $10^{intercept}$. Error in Γ is calculated from the fit error in the intercept.

2.4.4 Monte Carlo diffusion simulations

A custom MATLAB script B.3.3 was written to generate particle tracks for 200 particles per simulation. A unit cell was defined with periodic boundary conditions such that repetition of the unit cell filled the user defined image size (usually 128 $\times$ 128 pixels). The image area was converted to units of μm^2 according to a user defied pixel size in μm. A number of frames was also chosen which defined the matrix depth. A pseudorandom number generator (Mersenne Twister) was then used to chose a starting position (x & y coordinates and frame number). The pseudorandom number generator also defined the length of the track in frames. Each particle then performed a number of random walk steps where displacement coordinates in x and y were populated by the pseudorandom number generator. Length of the steps was defined by the user by input of a diffusion coefficient in μm^2 s^{-1} and an a frame time in milliseconds. This produced a matrix of time and space coordinates for each particle.

To generate simulated image stacks pixel values corresponding to particle spots and background noise were defined. A gaussian distribution of pixels with the desired width were given higher pixel intensity than the average pixel value (which was fixed at one). This was repeated for all co-ordinates in each frame, corresponding to the particles. Laser noise was added by multiplication of the image matrix with values which had a standard deviation defined *'noise'* level chosen by the user. Overall, user definition of the SNR altered the amplitude of the gaussian describing the spots as well as the level of background noise. The image data was exported in a TIF format for review using FIJI. The raw tracks or simulated image stacks were subsequently processed in the same way as experimental data.

Chapter 3

iSCAT Single Particle Tracking Experiment Optimisation

Chapters 1 and 2 introduced the principles of iSCAT and the general method of use for millisecond time resolution experiments. However diffusion processes occur on times scales from a few microseconds upwards and therefore it was necessary to optimise the set-up for the high speed tracking experiments necessary to properly probe these processes.

3.1 Experimental requirements

Figure 3.1 illustrates the need for careful understanding and control of the requirements for a particle tracking experiment at high time resolution. In practical terms, high time resolution means increasing the frame rate and therefore reducing the exposure time. The left hand panel (A) shows experimental data where 40 nm gold particles were tracked on the same SLB while the exposure time was decreased from 10 ms (black), through 100 µs (purple), to 8 µs (teal). It can be seen that these experiments each sample a different range of observation times but also that the apparent diffusion behaviour is different. At short exposure times the diffusion here appears much more anomalous than at millisecond time resolution. It is however known from the literature that this behaviour, where the transport coefficient reaches almost 100 $\mu m^2\ s^{-1}$, is unrealistic for an SLB [9, 68].

In an analogous experiment (Figure 3.1 B), exposure time was kept constant at 20 µs while the laser power through the objective was reduced from 2.5 to 0.8 mW (black to teal). Again, although the SLB is the same, the diffusion behaviour appears different depending on the laser power. This cannot be due to local heating as a temperature change of $\sim$ 3 K [99] is insufficient to cause a magnitude change in

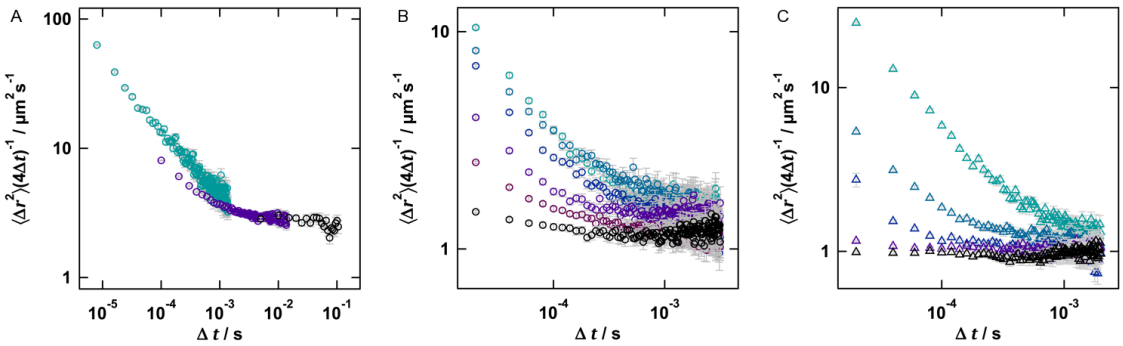

Figure 3.1: **Effect of SNR on MSD analysis.** (**A**) reducing exposure time 10 ms (black), 100 µs (purple), 8 µs (teal); (**B**) 20 µs exposure while reducing laser power 2.5 to 0.8 mW (black to teal) and (**C**) diffusion analysis of simulations with noise parameter (see Section B.3.3) changed to produce high SNR (black) to low SNR (teal).

diffusion coefficient as per the Stokes-Einstein relation which states that diffusion coefficient is proportional to temperature. In addition, lower laser powers, for which there will be less energy delivered to the sample, show apparently faster diffusion. The common factor in these two experiments is a decrease in signal to noise ratio (SNR).

To elucidate the effect of SNR on tracking artefacts, Monte Carlo simulations were carried out in MATLAB such that particles diffusing at 1 µm^2 s^{-1} were simulated with varying signal to noise ratios (Figure 3.1 C). The diffusion analysis of a true random walk must result in normal behaviour and this was confirmed by MSD analysis of the raw position data (black). The coordinates were then used to produce an image stack of bright spots, as described in the previous chapter, which were subjected to the same TrackMate procedures as experimental data. It can be seen that steep tails become more apparent as the SNR decreases (purple to teal). It is likely that these tails are an artefact of the tracking process when the SNR is low which results in poor localisation precision. Data such as this cannot be used for diffusion analyses as anomalous diffusion is apparent at short timescales which is artifactual and not a true representation of the diffusion process occurring.

Therefore, to ensure robust high speed tracking experiments the following requirements were addressed by microscope, experiment and processing optimisation:

1. *localisation precision*; sufficiently detailed point spread function including good signal to noise and appropriate spot magnification.

2. *fast imaging speeds*; sufficient laser power to allow short exposure times and appropriate protocols for handling larger volumes of data.

3. *robust tracking*; TrackMate handling of large image files with reliable output checked for tracking artefacts.

3.2 Microscope improvements

3.2.1 Magnification

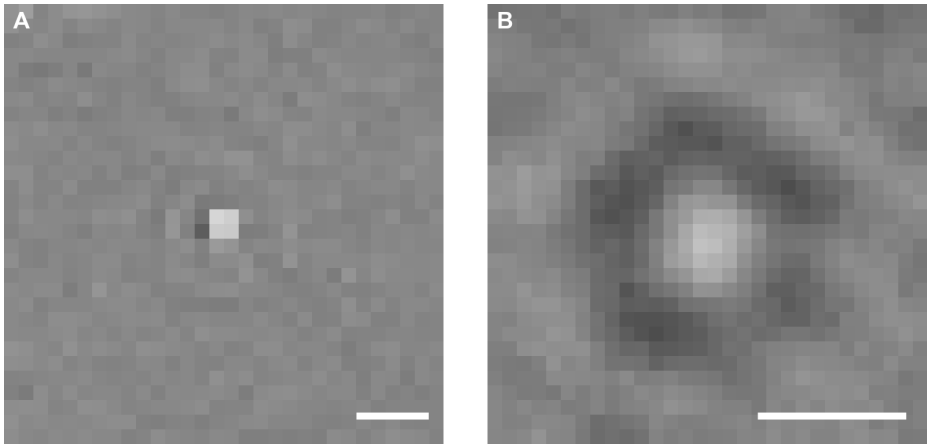

Figure 3.2: **Increase in magnification** (**A**) 174× magnification of a 40 nm gold particle with the original iSCAT set-up and (**B**) 354× on the optimised set-up. Both scales 500 nm.

It is important to be able to perform sub -pixel localisation on spots to get accurate diffusion information. The initial set-up had a low magnification resulting in the point spread function (PSF) of a 40 nm gold particle only registered over around three pixels (Figure 3.2 A) of the CMOS sensor. The first optimisation was to increase the magnification to 354× so that the PSF spanned 10 to 20 pixels (Figure 3.2 B). This also made the magnification similar to the fluorescence channel allowing for easier registration.

To achieve this magnification, five extra lenses were introduced (see Figure 3.3); where L1 = 75 mm, L2 = 75 mm, L3 = 125 mm, L4 = 50 mm and L5 = 200 mm. Although a similar magnification could be achieved with fewer lenses, this combination was chosen to give access to the conjugate back focal planes and conjugate image planes as indicated in Figure 3.3. The laser was directed through L1 and L2 such that it was collimated at the back aperture of a 100× oil immersion objective (NA 1.49, Nikon, Japan) resulting in a focus in the plane of the sample.

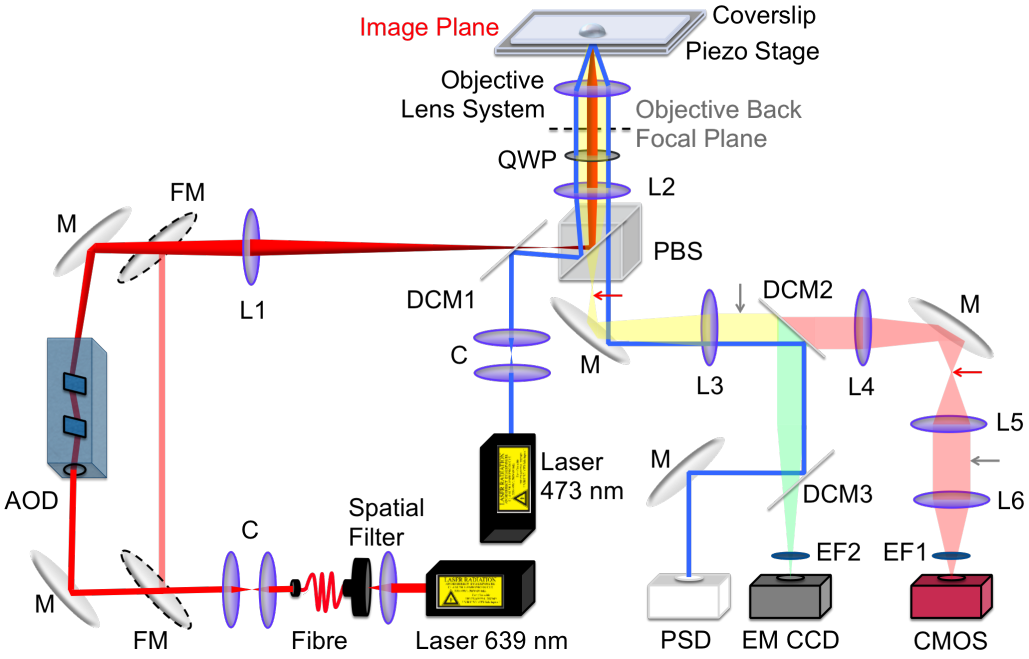

Figure 3.3: **Scheme of the optimised iSCAT microscope.** (**AOD**) acousto-optic deflector, (**C**) collimation, (**CMOS**) Phantom Miro camera, (**DCM**) dichroic mirror, (**EF1-2**) emission filters (**EM CCD**) Andor iXon3, (**FM**) flip mirror, (**L1-6**) lenses (details in text), (**M**) mirror, (**PBS**) polarising beam splitter, (**PSD**) position sensitive diode, (**QWP**) quarter wave plate. The objective lens system is represented by one lens but in practice is a compound assembly of multiple lenses. Yellow represents a common path between iSCAT (red) and fluorescence (green). Arrows; (**red**) conjugate image planes and (**black**) conjugate focal plane.

3.2.2 Imaging speed and illumination

To achieve the desired frame rates, new hardware was required. An ultra-fast Phantom CMOS camera (Phantom Miro M310, Vision Research, Wayne, NJ.) was introduced, which records images at up to 650000 frames per second. However, at such high imaging speeds, the AODs became unsuitable due to an order of magnitude loss of power and an uneven, undulating illumination field resulting from the slow scan rate compared to the acquisition rate of the new camera. To account for this, flip mirrors were introduced to create two illumination paths, either via the AOD or bypassing it to allow a higher light intensity at the sample from the unmodulated beam. This allows for both slower experiments using the scanned beam as well as fast experiments with high light intensity.

For the fast experiments the beam was not rastered resulting in a small area of illumination with an intensity pattern dependant on the beam profile. Thus, without AOD scanning it was imperative to have a stable and flat illumination profile from

the laser. To achieve this, a spatial filter and an optical fibre were introduced. This served to eliminate any pointing instability from the laser source and to clean the beam. The resultant illumination field filled 128 by 128 pixels of the camera chip, which allowed a maximum frame rate of 120700 frames per second. Multiple image stacks were recorded per sample to ensure at least 50 particles were detected in this small field of view.

3.3 Experiment improvements

Further to these microscope improvements, experimental factors were considered for an optimal SPT experiment.

3.3.1 Scattering cross-section

In Section 1.5.2 the cubic relation of the detected interferometric signal with particle volume was introduced. Thus, one method of ensuring high SNR is to use the largest particle label suitable for the experiment. Figure 3.4 shows an image from various gold nanoparticles conjugated to a SLB and the associated intensity profiles through the spot.

It is noted that the iSCAT theory dictates that the interferometric signal from a gold bead should produce an image which appears as a dark spot on a bright background [99]. This is true for scattering signals much smaller than the reflected signal, where the interference cross term is detected, rather than the pure scattering term which would produce a bright spot on a dark background as in dark-field. However, it is also demonstrated by Ortega-Arroyo *et al.*, that both types of image are measurable for 40 nm gold particles similar to those used for this thesis. Certainly for large, > 50 nm, particles the pure scattering term would be detected resulting in a bright spot. As TrackMate only detects bright spots it was favourable to produce images that resemble those from dark-field. This was achieved by either collecting signals enhanced by the scattering term or by inversion of the purely interferometric signal. This is acceptable for the study of diffusion processes, as the phase of the particles in the image has no impact on localisation precision.

Values for contrast and SNR from one line profile per image from Figure 3.4, were calculated as described in Chapter 2. In addition to this, an ensemble of more than 100 particles were analysed using MATLAB (also outlined in Chapter 2). This analysis demonstrates that using a larger gold particle ensures a better SNR (Table 3.1). However, using such large particles is not always desirable in diffusion experiments.

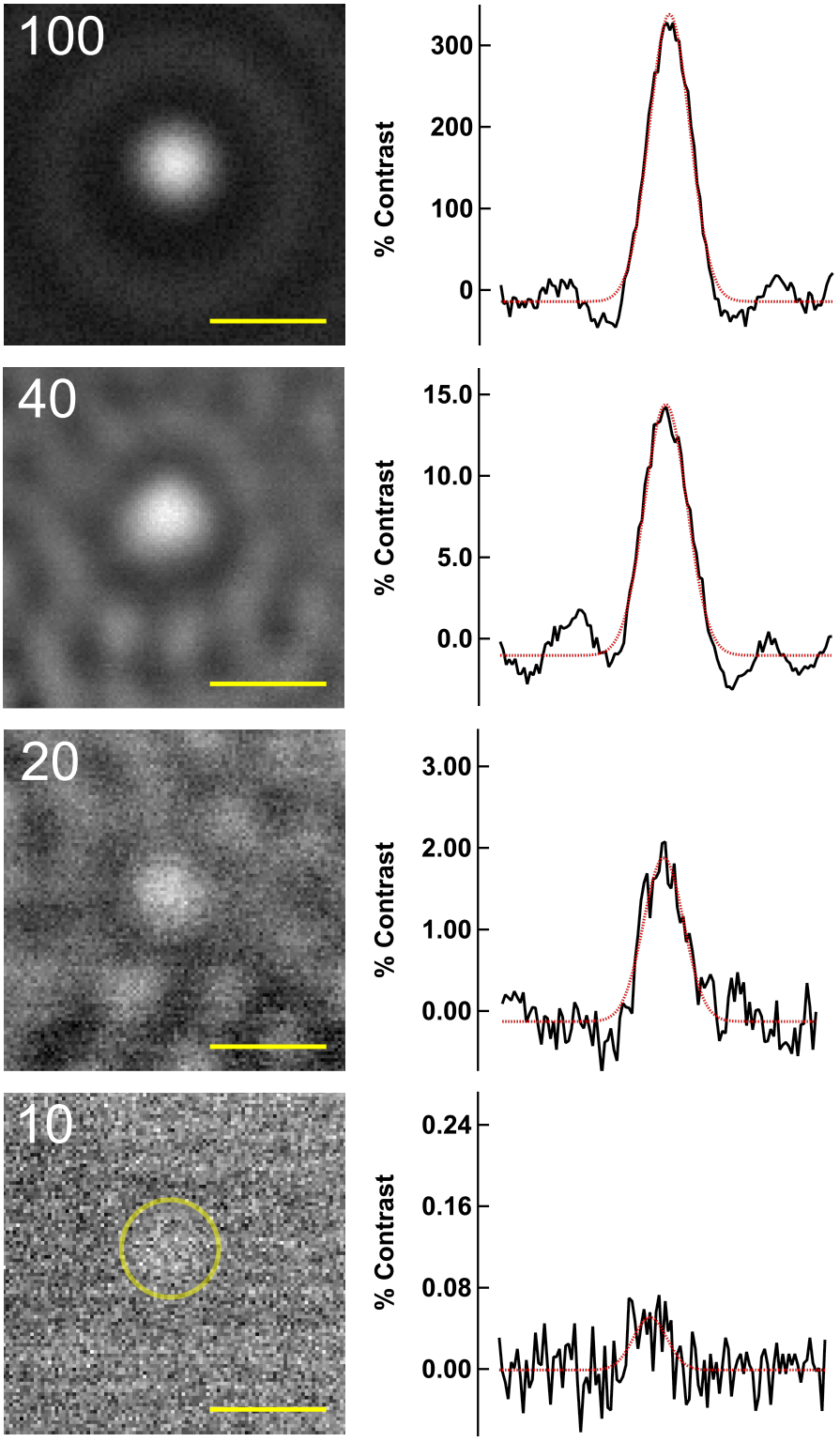

Figure 3.4: **Effect of gold label size on contrast and SNR.** From top to bottom: 100 nm, 40 nm, 20 nm and 10 nm gold particle with associated line profiles fit with a 1D gaussian (red lines, see Section 2.4.2). Scale bars all 1 µm. 20 µs exposure, Phantom camera.

Table 3.1: **SNRs Extracted From iSCAT Images of SLBs Labelled With Gold Nanoparticles of Various Sizes.** SNRs extracted from the line profiles in Figure 3.4 or using Gaussian fitting by custom MATLAB code. Refer to Section 2.4.2 for method details.

Size /nm	Single Profile		MATLAB Method	
	Contrast (%)	SNR	Contrast (%)	SNR
10	0.1	19	0.4	1
20	2.1	62	1.8	3
40	15.4	117	11.7	4
100	352.1	172	555.6	25

Large particles will have some effect on the diffusion of the lipid anchor [55]. To explore this under experimental conditions relevant to this thesis, 10, 20, 40 and 100 nm gold particles were conjugated to an SLB and tracked at 20 µs time resolution. The $\langle \Delta r^2 \rangle (4\Delta t)^{-1}$ *vs.* Δt plots produced from the MSD analysis are shown in Figure 3.5A.

It can be seen that 10 nm particles do not have sufficient SNR to be reliably tracked. The 20 nm particles show some signs, as previously discussed, of poor localisation at short observation times. By grouping 5 or 10 frames and averaging the data before tracking (Figure 3.5B) one can see that the apparent diffusion becomes more normal. For 100 nm particles, as one might expect, the diffusion appears to be slower. The diffusion also appears to be more anomalous. This is unlikely to be a localisation artefact because the SNR is high and the anomalous behaviour presents at longer time scales rather than short. This is indicative that the particle is actually confined and not freely diffusing. This was confirmed by tracking at 20 ms time resolution which showed $\alpha = 0.0$. Therefore this label cannot be used for diffusion studies despite having the highest SNR.

The most reliable data comes from tracking of 40 nm particles; the diffusion appears to be normal even without averaging. Therefore, 20 to 40 nm gold particles were chosen for the experiments which follow in Chapters 4 and 6. These are the smallest particles with sufficient SNR with and without image averaging respectively. Specific imaging and data processing details are given in each chapter. Owing to

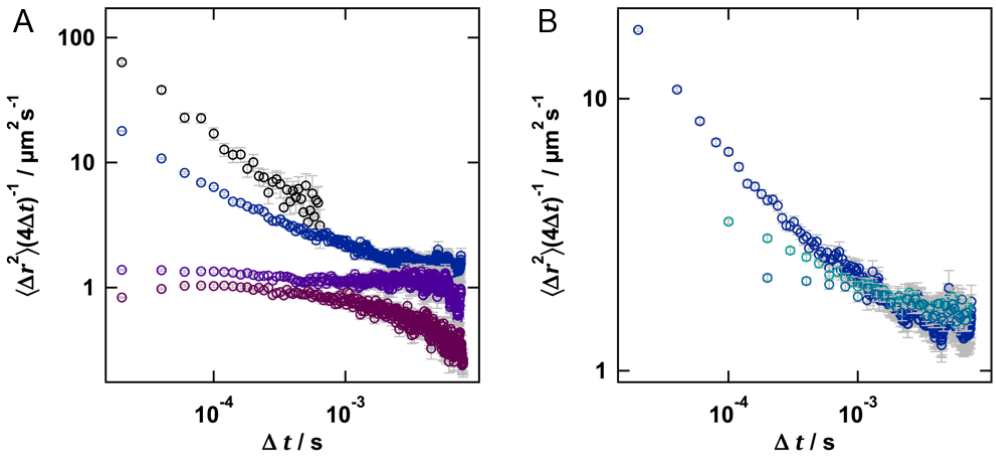

Figure 3.5: **Effect of gold label size on diffusion.** (**A**) diffusion analysis at 20 μs time resolution of 10 nm (black), 20 nm (blue), 40 nm (purple) and 100 nm (burgundy) particles. Particles with higher SNR show slower diffusion which is not anomalous compared to smaller particles. (**B**) Frame averaging can be used to increase SNR. Diffusion analysis of 20 nm particles with images ungrouped (dark blue), averaged by 5 frames to give 100 μs time resolution (teal) and averaged by 10 frames to give 200 μs time resolution (light blue).

the different methods of calculation, the absolute values of SNR vary between the profile and ensemble methods. However, the trend remains the same. The values presented in Table 3.1 can loosely be used as 'standards' for comparison with SNRs from different experiments also analysed with a particular method. For example, one can conclude that when analysing line profiles, a SNR greater than 60 is necessary, while ensemble analysis showing SNRs greater than 3 can be used with confidence.

3.3.2 Reducing reflected and stray light

One factor limiting the ability to increase the incident laser power (improving SNR and allowing faster imaging speeds) is the large reflected signal from the coverslip interface. This signal can saturate the detector and swamp the desired signal. One method of reducing this signal is using antireflective substrates. Originally designed for Surface Enhanced Ellipsometric Contrast (SEEC) microscopy, *Nanolane surfs* (Eolane, Montfort le Gesnois, France) are coated silicon dioxide substrates of 145 μm thickness. The material is optimised for an incident wavelength of 550 nm and an angle of incidence of 25-50°. To explore the applicability to the iSCAT set up with 639 nm incident light, the surfs were used in place of standard coverslips. They were carefully cleaned with the same sonication protocol and treated to a short oxygen plasma cycle. This allowed for the formation of DIBs and for the fusion of GUVs on

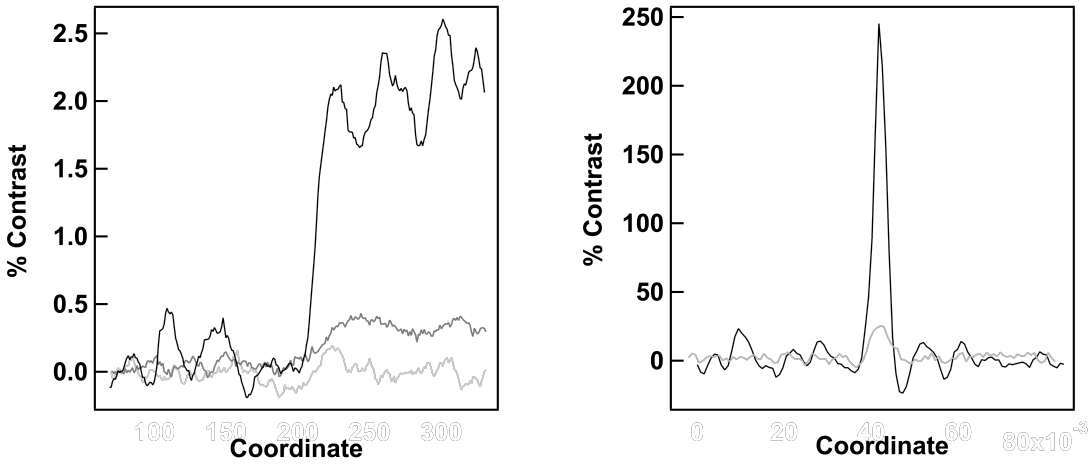

Figure 3.6: **Contrast enhancement using Nanolane substrates.** (**A**) bilayer edge, (**B**) 40 nm gold nanoparticle. light grey - on glass, grey - on Nanolane with same light intensity, black - on Nanolane under saturating conditions. Coordinate represents the distance along the line profile in pixels.

the surfaces in two separate experiments.

3.3.2.1 Bilayer stacks

DPhPC with 0.2 mol% Atto488-DOPE and 10^{-5} mol% biotin-DOPE was prepared at 2 mg ml^{-1} in chloroform. Bilayer stacks were formed by spreading 5 µl of the lipid mixture onto a coverslip or surf heated to 40 °C. Once the chloroform had fully evaporated a well of vacuum grease was created around the dried lipids and 100 µl of buffer was added. The sample was then transferred to a hydration chamber and left to hydrate at 60 °C for 48 hours. The buffer was then exchanged ten times to remove any free lipids. A bilayer edge was located and individual frames captured with 20 ms exposure time. A background image for subtraction was recorded in an area with no bilayer. Figure 3.6A shows low contrast ($\sim$ 0.2 %) for a bilayer on glass. This is consistent with previously published data [78] . On the Nanolane substrate there is a modest increase in contrast for the same experimental conditions. However, as the substrate is antireflective, the chip is no longer saturated with background signal. This allows for a 10 $\times$ increase in laser power incident on the sample which gives an order of magnitude increase in contrast.

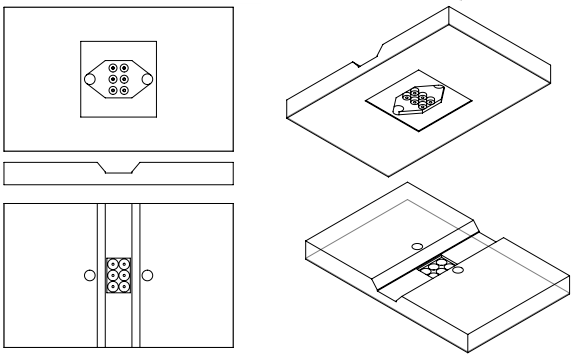

Figure 3.7: **Schematic of the custom device for Nanolane substrates.**

3.3.2.2 DIBs

In the second experiment, DIBs containing 40 nm gold labelled lipids were formed as outlined in Section 2.2.2 on both glass coverslips and on the Nanolane substrate. A custom PMMA device was machined to fit the small 10×10 mm substrates (Figure 3.7) and was used in place of the usual device (refer to Figure 2.1). Tracking and contrast analysis were performed as outlined in Sections 2.4.1 and 2.4.2. Representative line profiles for a particle on the glass and Nanolane substrate are shown in Figure 3.6 B (grey and black respectively). Again, there is a order of magnitude increase in the contrast from the glass sample to the particles on the Nanolane substrate.

This data is very encouraging, suggesting that such substrates may allow greater contrasts from biomolecules such as single unlabelled proteins [29, 117, 112, 118], which are known to have low contrast on conventional substrates . However, there were some practical considerations which prevented the substrates from being used for the experiments described in the following sections. The substrates cost approximately £10 per 10×10 mm substrate. This cost was deemed too great to use the substrates for a single experiment. Reuse required careful cleaning which, eventually, destroyed the coating. As mentioned above a bespoke PMMA device was created for the DIBs however the following experiments required the SLB platform. The conventional vacuum grease well method leaves a residue which is particularly difficult to clean and therefore not suitable for use on the Nanolane substrates. The coating was also sensitive to scratching from tweezers whilst handling. Once the coating was disrupted, there was no longer an enhancement to the contrast.

3.4 Optimisation of acquisition and analysis

It is desirable to probe diffusion processes over at least five orders of magnitude in observation time, from tens of microseconds to several seconds. It is possible to do this by reviewing data from multiple experiments at different exposure times however it would be advantageous to achieve this in a single experiment to minimise errors and discontinuity. Therefore to record at microsecond time resolution for at least a second over all, image stacks on the order of 10^5 to 10^6 frames are needed. Such large files are computationally demanding and required development of the background subtraction protocol outlined in Section 2.3.2.

3.4.1 Image collection and initial processing

For a typical 128×128 pixel image stack of 100,000 frames, the size of a multipage TIF stack was over 2 GB, whereas the preferred CINE file format output was ~ 1 GB. It was therefore favourable to save directly in the CINE format. However, these files cannot be directly loaded into ImageJ for analysis. Therefore a Python script (see Appendix B) was written to read and convert the CINE files into TIFs. This script also allowed for automated background subtraction and averaging outside of ImageJ.

3.4.2 Tracking

The limiting factor in the image processing then became TrackMate. The built-in plugin runs a *Hyperstack Displayer* which allows visualisation and manual editing of the detected spots in the input image stack. For a 100,000 frame stack this is computationally very demanding and could take upwards of 20 minutes to complete. To circumvent this, the TrackMate script which runs the GUI was instead run directly from the ImageJ command line. This GUI free version of the tracking programme did not perform the *Hyperstack Displayer* routine and was therefore much faster than using the interface.

3.5 Summary

The microscope was optimised for fast single particle tracking experiments by increasing the magnification and ensuring delivery of a flat, high intensity illumination fields. Studies into optimal contrast and signal to noise ratio means that subsequent experiments can confidently be tracked with limited artefacts. This allows for more

confidence in the diffusion behaviours detected. In the following chapters, for any tracking at greater than 2 ms frame rates, the optimised set-up described above was used. The configuration in which the AODs were bypassed results in 3.5 mW delivered to the sample when not attenuated with optical filters.

Chapter 4

Controlling Anomalous Diffusion in Artificial Membranes Using PEG-lipids

Work presented in this chapter was completed in collaboration with M.R. Cheetham and forms the basis of the paper cited in Appendix A. MRC produced bilayers and performed the TIRF imaging, HLEC produced bilayers, completed the gold labelling, iSCAT imaging and performed all analyses. AFM imaging was supervised by Y. J. Wang.

4.1 Introduction

There are still inconsistencies with the definition, analysis and modelling of anomalous diffusion. This hinders the full understanding of this behaviour *in vivo*. In 2012, Saxton proposed that a *'positive control'* was needed to standardise some of the experimental aspects of the physical models and techniques which are used to study anomalous diffusion [131]. The eight criteria proposed were;

1. Simple to produce.
2. Stable fluorescence.
3. The anomalous regime to extend over 2-3 orders of magnitude, and if transient anomalous subdiffusion, that normal and anomalous regimes are distinct.
4. A tuneable subdiffusion exponent with a well understood mechanism, such as percolation.
5. Biologically relevant length and time scales.

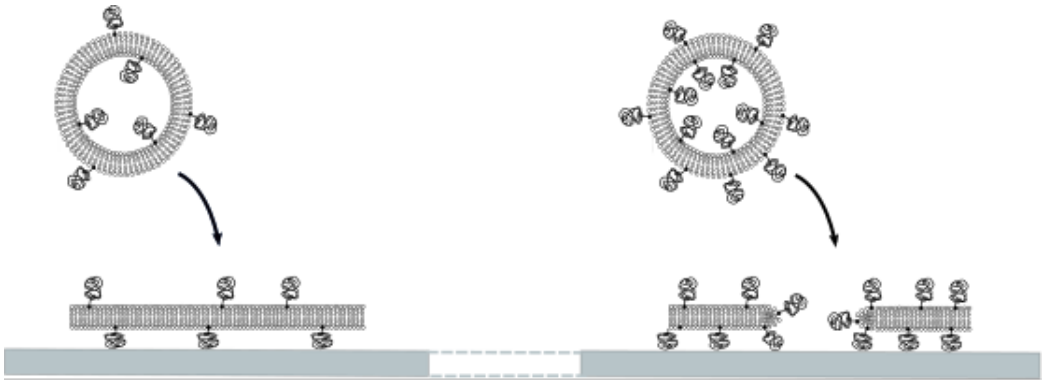

Figure 4.1: **Schematic of SLB disruption by PEG-DPPE.** As the mole fraction of PEG-DPPE lipids increases (left to right), defects form in the bilayer that that act as obstacles, generating anomalous diffusion.

6. Tracers detectable by both nuclear magnetic resonance (NMR) and fluorescence.
7. Transparent and non-fluorescent medium.
8. Either (i) spatially homogeneous, or (ii) inhomogeneous at all length scales for a fractal substrate.

This chapter describes the production and characterisation of a simple SLB model which aimed to address these criteria. PEG modified lipids are known to disrupt the formation of SLBs [132]. This was exploited to produce bilayers as depicted in Figure 4.1, which contained defects that were expected to act as immobile obstacles and therefore induce anomalous behaviour.

4.2 Specific methods

4.2.1 Lipids

Table 4.1: **Ranges of PEG-DPPE used in this chapter to form SLBs.**

PEG / kDa	mol%
1	$2.0 - 10.0$
2	$1.0 - 5.0$
5	$0.5 - 3.5$

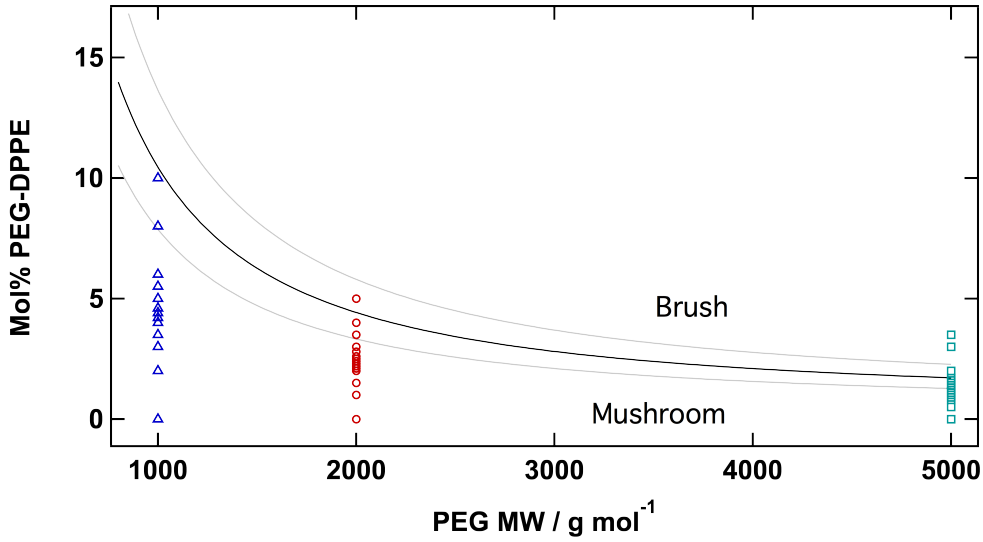

Figure 4.2: **Position of PEG-DPPE levels used in relation to the mushroom-brush transition.** Adapted from [132] where black line is the theorised transition for an area per lipid of 60 Å^2 and a monomer size of 3.7 Å, lower grey 50 Å^2 and a monomer size of 3.9 Åand upper grey 70 Å^2 and a monomer size of 3.5 Å. Mole fractions for each experiment containing PEG(1K)-, PEG(2K)- and PEG(5K)-DPPE are represented in blue triangles, red circles and green squares respectively.

SUVs were produced as outlined in Section 2 from 1 mg ml^{-1} DOPC only and DOPC with PEG(1K)/(2K)/(5K)-DPPE in the range of compositions detailed in Table 4.1. Polymers exhibit different morphology dependent on the area they are able to occupy. The mushroom-brush transition can be estimated using theory outlined by Kaufmann *et al.* [132]. Briefly, The Flory radius (R_F) of the polymer can be estimated using Equation 4.1,

$$R_F = aN^{\frac{3}{5}} \tag{4.1}$$

where a is the length of the monomer and N is the number of monomer units in the polymer chain. The distance between two polymers (s) is then estimated using Equation 4.2,

$$s = \left(\frac{A}{m}\right)^{\frac{1}{2}} \tag{4.2}$$

where A is the average area per lipid and m is the mole fraction of PEG-lipid in the bilayer. The mushroom regime is defined as $s > R_F$, while the brush regime is

defined as $s < R_f$. Levels of PEG-DPPE used in this study generally correspond to the polymer mushroom regime (Figure 4.2).

4.2.2 Atomic Force Microscopy, AFM

AFM was carried out using a BioScope Resolve (Bruker, Billerica, USA). An SNL-10B cantilever was used with a spring constant of 0.12 N m^{-1}. The instrument was run in peak-force tapping mode with a maximum applied force of 40 pN.

4.2.3 Fluorescence Recovery After Photobleaching, FRAP

FRAP experiments were carried out as described by Axelrod *et al.* [133]. A DOPC only and DOPC plus 2.6 mol% PEG(2K)-DPPE SLB were made as per the general method with 0.5 mol% TR-DHPE. Using the TIRF microscope illustrated in Section 2, a 532 nm laser was confined to a small area using an iris and used to bleach this region of the sample for 30 seconds. The illumination intensity was reduced, the iris opened and the bilayer immediately imaged every 5 seconds for the following 10 minutes. The intensity of the recorded image was analysed over time to produce recovery curves. The curve from the DOPC only sample was fit with a Bessel function [134] to quantify the diffusion constant.

4.2.4 DIBs

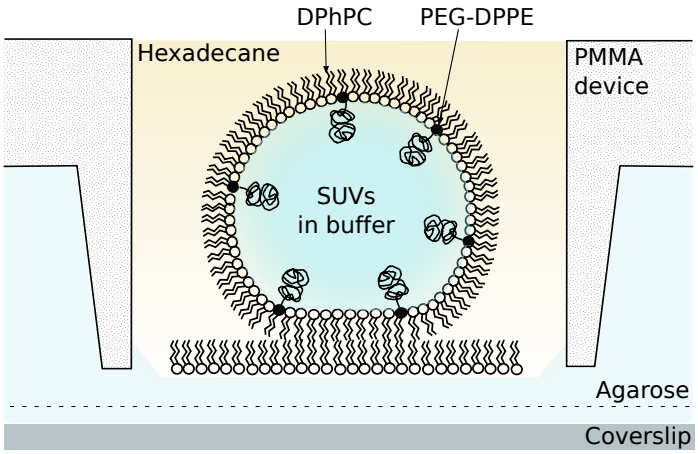

Figure 4.3: **Schematic of the asymmetric PEG-DPPE containing DIB.** DIBs were prepared following the method outlined in Section 2.2.2.

DIBs were prepared following the lipid-in method described in Chapter 2 using SUVs of DPhPC only and DPhPC + PEG(2K)-DPPE. The DIB experiment is represented schematically in Figure 4.3.

4.2.5 Tracking

TIRF imaging was completed as per the general method. To track gold nanoparticle-labelled lipids using iSCAT, the optimised optical set-up from Chapter 3 was used with the laser bypassing the AOD. SLBs were produced from the lipid compositions mentioned above. After incubation and rinsing, 5 μL of OD10 20 nm gold nanoparticles were added to the buffer above the SLB and incubated for a further 30 minutes. The SLBs were washed thoroughly with buffer before image stacks of 100000 frames were recorded at 100 kHz. Image stacks were then temporally-averaged using a Python code (Appendix B) to 5 kHz before tracking.

4.2.6 Monte Carlo simulations

Simulated image stacks were created showing 200 simulated particles described by two separate random walks in the x and y directions (see Section 2.4.4). An immobile obstacle was introduced by exclusion of a circle of radius r within the simulation unit cell of size s. Periodic boundary conditions were used to repeat the unit cell to fill the desired image size (128 × 128 pixels at 0.4 μm px^{-1}). A schematic of the unit cell is shown in Figure 4.12A. With each step of the random walk, the new coordinates were tested to see if they were inside an obstacle or not. If they were, then that step was rejected, and a new one generated. The resulting sets of co-ordinates for each simulated particle were subsequently processed in the same way as experimental data obtained from tracking labelled particles.

4.3 Theory

Unlike a pure diffusion coefficient, the transport coefficient Γ is more difficult to interpret as it has dimension of $[\text{Length}]^2/[\text{Time}]^\alpha$. Therefore the dimensions change for different degrees of anomalous behaviour. This can be overcome by de-dimensionalising the observation time [41] by introducing a characteristic time scale parameter or *'jump time'*, τ as follows:

$$\left\langle \Delta r^2 \right\rangle = 4D\Delta t \left(\frac{\Delta t}{\tau} \right)^{\alpha-1}. \tag{4.3}$$

By combining with Equations 1.2 and 1.3 (see Chapter 1), the relationship between the ratio of transport coefficient and pure diffusion coefficient with τ is:

$$\frac{\Gamma}{D} = \tau^{1-\alpha}. \tag{4.4}$$

τ can then be found from the gradient and intercept of a plot of $log_{10}\frac{\Gamma}{D}$ *vs.* α. One can interpret τ in terms of a characteristic length scale (λ) associated with the anomalous behaviour using the diffusion equations introduced in Section 1.3.1 which in 2D becomes $\lambda = \sqrt{4D\tau}$.

4.4 Results

4.4.1 AFM shows interfacial defects

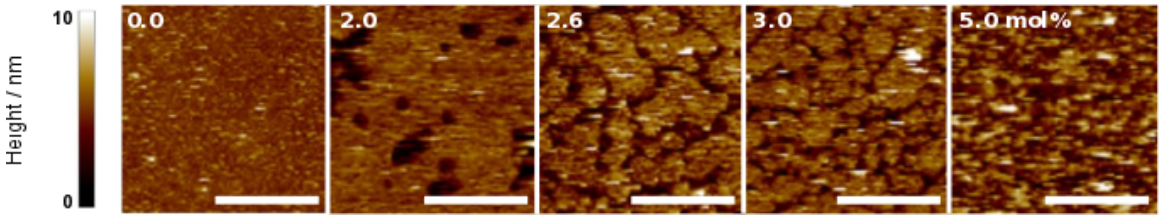

Figure 4.4: **AFM imaging of PEG(2K)-DPPE containing SLBs.** AFM shows an increase in defect area fraction with increasing mol% PEG-(2K)DPPE (scale 500 nm).

AFM was used to visualise the physical character of the bilayer in reference to our hypothesis. It can be seen in Figure 4.4 that increasing levels of PEG-DPPE results in a larger number of bilayer defects, eventually resulting in isolated bilayer patches.

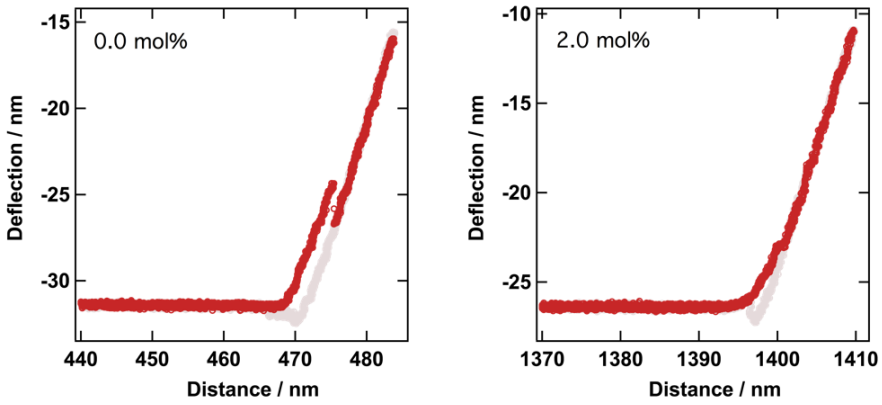

Figure 4.5: **AFM force curves.** AFM force curves show characteristic *'punch through'* behaviour for a DOPC SLB and one containing 2.0 mol% PEG-(2K)DPPE. Downward trajectory (red), return curve (grey).

Force curves confirm the presence of bilayers for a DOPC SLB and one containing 2.0 mol% PEG-(2K)DPPE (Figure 4.5). Curves for higher concentrations of PEG-DPPE were not completed; this is discussed further below.

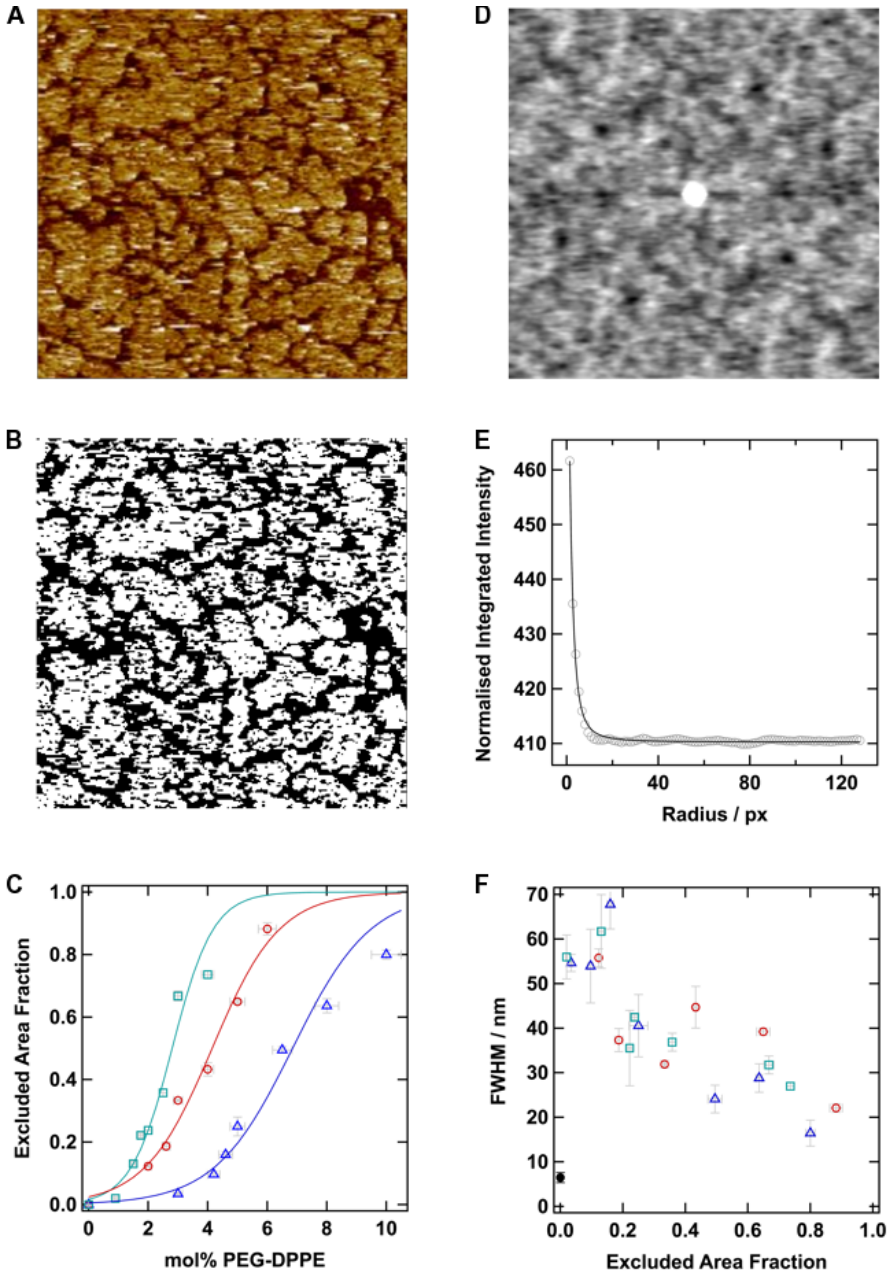

Figure 4.6: **Thresholding and autocorrelation of AFM images.** The original AFM image for an SLB containing 2.6% PEG(2K)-DPPE (**A**) was was applied with an auto-threshold and binarised in ImageJ (**B**). The area associated with the detected defects as a fraction of the total area gives the excluded area fraction. This analysis was undertaken for every lipid composition to give the EAF to mol % calibration curves (**C**). An autocorrelation (**D**) was calculated from the binarised image using the FD Math function of ImageJ. Radial profile analysis of the autocorrelation results in a profile (**E**) which is fit with a Lorentzian form to extract the FWHM. There is a modest decrease in length scale as the excluded area fraction increases (**F**). The solid black data point is DOPC only SLB. For (**C&F**) PEG(1K)-, PEG(2K)- and PEG(5K)-DPPE are represented in blue triangles, red circles and green squares respectively.

Figure 4.6 illustrates the steps involved in the analysis of the AFM images. Firstly, TIFF images were exported from the NanoScope Analysis software and loaded into FIJI (A). Thresholding was applied at the automatic level with the default function resulting in selection of the pixels corresponding to defects. The image was then binarised based on this selection (B) and the number of pixels associated with the defects (black) reported as a fraction of the total area to give the excluded area fraction (EAF). This was completed for a subset of mole fractions of all PEG lengths. When compared to the mol% PEG-DPPE content of the bilayer, a calibration curve (C) was produced. The curves for each PEG length were fit with a single sigmoid as shown. Auto-correlation of the images was performed using the FD Math function in FIJI to estimate the defect size. The resultant plot (D) was then radially averaged using a radial profile function before fitting with a Lorentzian function (E) in Igor of the form;

$$\frac{(y_0 + A)}{((x - x_0)^2 + B)} \tag{4.5}$$

The parameter B was extracted and is related to the full width half maximum (FWHM) as:

$$FWHM = 2\sqrt{B} \tag{4.6}$$

Panel F shows the correlation of FWHM with EAF. It can be seen that there is a modest decrease in the correlation size as EAF increases.

4.4.2 PEG bilayers exhibit anomalous behaviour

The single particle TIRF and iSCAT microscopy data were analysed as outlined in the general methods. The generated $\langle \Delta r^2 \rangle / 4\Delta t$ *vs.* Δt plots are shown in Figure 4.7. There is a plot for each PEG length for both fluorescence (left hand plot) and iSCAT (right hand side). Firstly the plot from analysis of the fluorescence data from PEG(2K)-DPPE (Figure 4.7A) shows increasingly anomalous behaviour on all time scales as the PEG mol% is increased from 0.0 to 5.0 mol% as detailed in the inset legend. A similar trend is seen for PEG(1K)-DPPE and PEG(5K)-DPPE (Figure 4.7C and E respectively). Similarly B, D and F show the iSCAT data for PEG(2K),(1K) and (5K). However, as the iSCAT data was recorded at a higher sampling rate, a

Table 4.2: **Pure diffusion coefficients (0.0 mol% PEG-DPPE) for each series of experiments.**

PEG / kDa	D_0 / μm^2 s^{-1}	
	Fluorescence	iSCAT
1	2.858 ± 0.026	1.368 ± 0.003
2	2.460 ± 0.017	1.585 ± 0.005
5	2.565 ± 0.024	1.793 ± 0.005

different diffusive behaviour is observed at short observation times. Between approximately 200 μs and 1 ms the diffusion is largely normal, after which there is then a crossover to anomalous behaviour. It can be seen that the position on the y axis is slightly lower for the iSCAT than for the fluorescence data.

The PEG(2K) data plotted as $\log\left(\langle\Delta r^2\rangle/4\Delta t\right)$ *vs.* $\log(\Delta t)$ is shown in Figure 4.8. Similar plots were produced for the other PEG lengths. They were fit with a straight line of the form $y = bx + a$ weighted by the error bars in Igor, as described in the general methods, to extract α and Γ values. Owing to the two diffusive modes in the iSCAT data, the curve was fitted from -2.0 to -0.5 corresponding with timescales between 10 and 316 ms. Example fits are shown in the figure with their reported fitting parameters.

Γ is equivalent to D when $\alpha = 1$. Therefore, the pure diffusion coefficients (D_0) were determined from the Γ value extracted for the data corresponding to 0.0 mol% PEG-DPPE (black markers in each plot in Figure 4.7). These are summarised in Table 4.2.

4.4.3 Anomalous exponent can be finely tuned

The anomalous parameters α and Γ extracted as described above were correlated with mol% PEG and EAF (Figure 4.9). In all cases a single sigmoid was fit to the data. The iSCAT data is well correlated with the fluorescence data in panel A which shows the switch in α from free diffusion at low PEG concentrations to confined diffusion at higher mole fractions. Each PEG length has a different midpoint where longer PEG chains require lower mole fractions to cause a significant change in the α value (see Table 4.3 for values). This is the same trend for the reduction in Γ as the mol% of

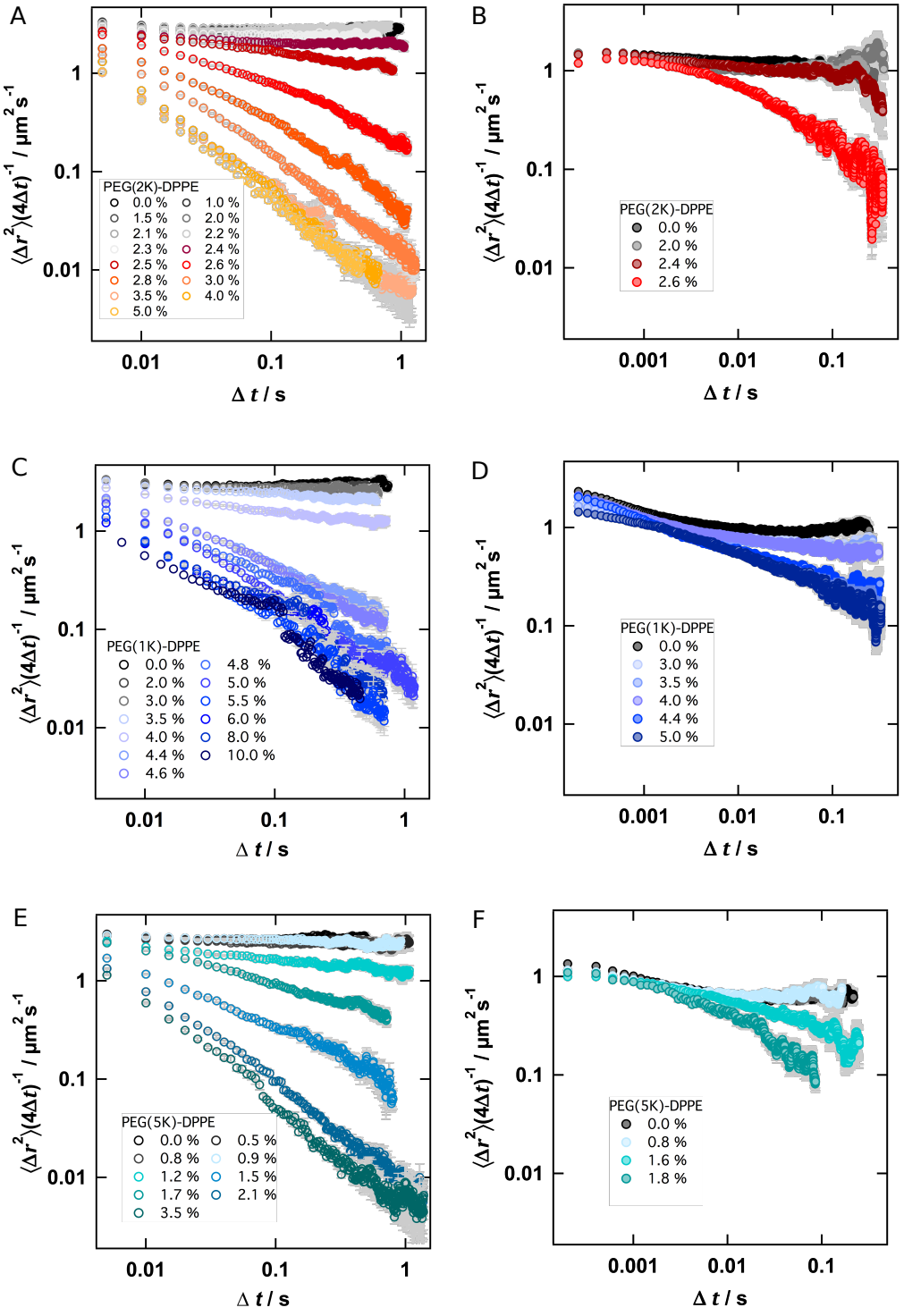

Figure 4.7: **Anomalous diffusion in PEG bilayers.** The $\langle \Delta r^2 \rangle / 4\Delta t$ *vs.* Δt plots show that anomalous sub-diffusion increases as mol% PEG-DPPE increases. PEG(2K)-DPPE; (**A**) fluorescence and (**B**) iSCAT. PEG(1K)-DPPE; (**C**) fluorescence and (**D**) iSCAT and PEG(5K)-DPPE; (**E**) fluorescence and (**F**) iSCAT. The same behaviour is seen for all three PEG molecular weights. Error bars throughout represent standard errors.

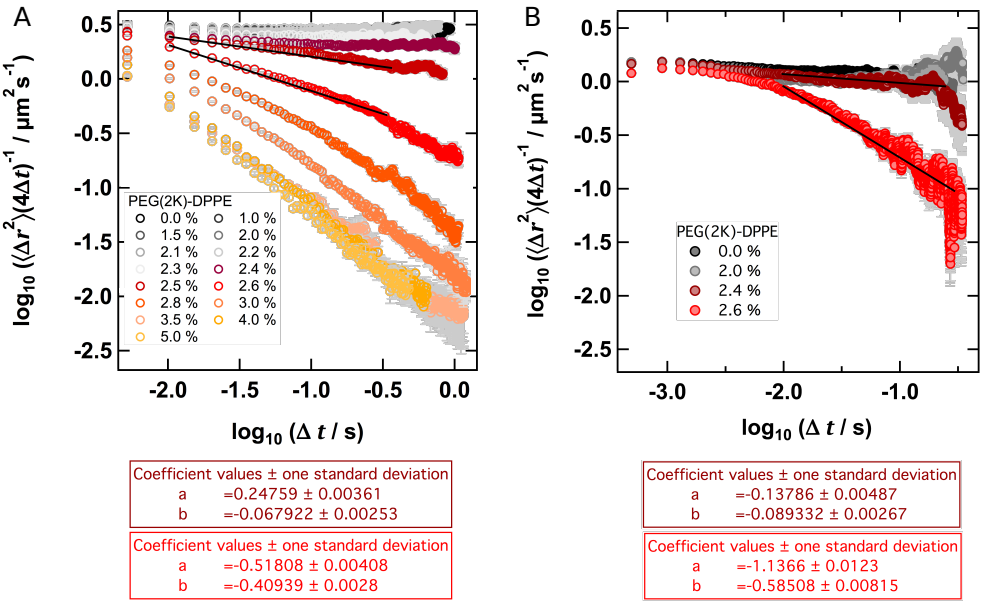

Figure 4.8: **Extraction of α and Γ.** Straight lines are fit to $\log\left(\langle\Delta r^2\rangle/4\Delta t\right)$ *vs.* $\log(\Delta t)$ plots or select levels of PEG(2K)-DPPE for both (**A**) fluorescence and (**B**) iSCAT data to extract α $(1+b)$ and Γ (calculated from parameter a as 10^a). The same analysis was carried out for the other data shown in Figure 4.7.

added PEG is increased. The y intercept corresponds to the pure diffusion coefficient of a contiguous bilayer containing no PEG-DPPE. Thus here the iSCAT data does not fully coincide with the fluorescence data and exhibits a slower coefficient owing to a significantly larger tracer (see Section 3.3.1).

Table 4.3: **Experiment sigmoid fit midpoints.** Midpoints extracted from the sigmoid fit of the α *vs.* mol% PEG-DPPE plots (Fig. 2D) for both fluorescence and iSCAT data. In each case the midpoint agrees very well and can be regarded as an indicator of the percolation threshold.

PEG / kDa	mol% (fluorescence)	mol% (iSCAT)
1	4.556 ± 0.004	4.785 ± 0.053
2	2.700 ± 0.002	2.545 ± 0.019
5	1.745 ± 0.001	1.745 ± 0.005

Plotting α against EAF (Figure 4.9C) however, results in a correlation in which all data from the three PEG lengths can be fit by a single sigmoid. Again both the

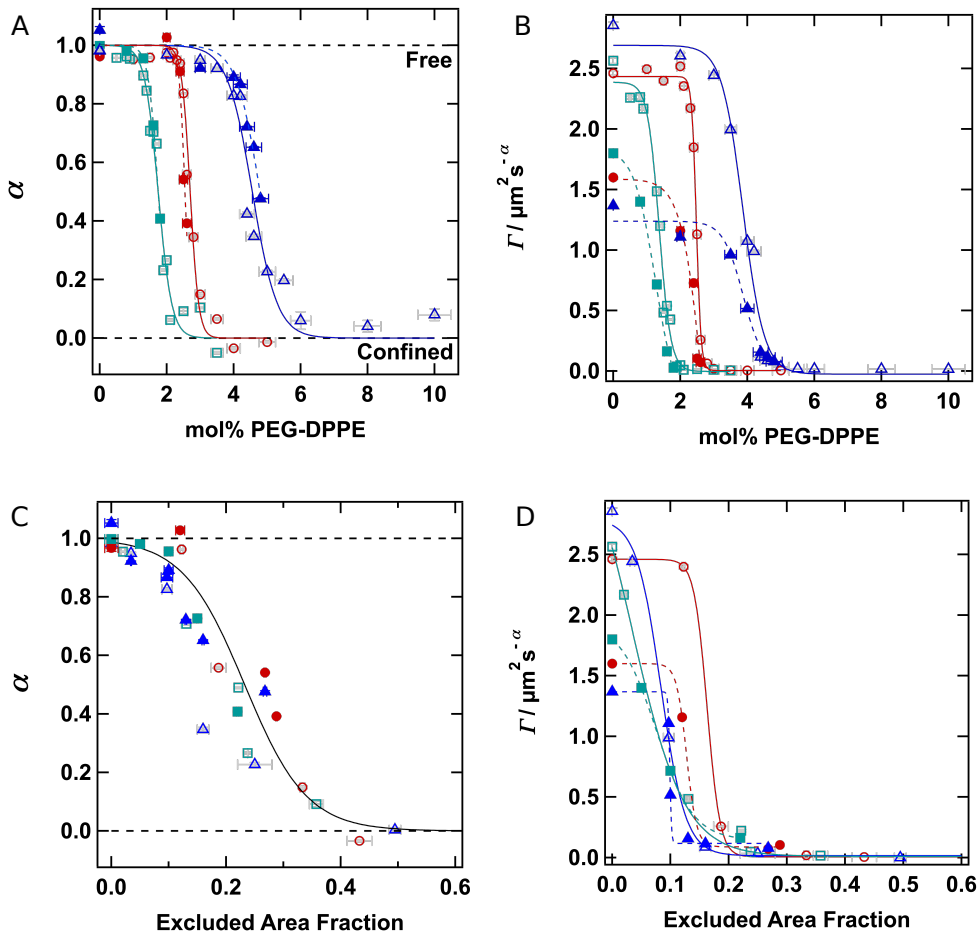

Figure 4.9: **Variation of α and Γ with mol% PEG and EAF.** (**A&B**) Variation of α and Γ respectively with mol% PEG. (**C&D**) Variation of α and Γ respectively with EAF. PEG(1K)- (blue triangles), PEG(2K)- (red circles) and PEG(5K)-DPPE (green squares) including both fluorescence data (open markers, solid fit lines) and iSCAT data (closed markers, dashed fit lines). Error bars throughout represent standard errors.

iSCAT data and fluorescence data are in good agreement. However, although the sigmoidal relationships of Γ *vs.* EAF (panel D) begin to overlap, they cannot be fit as a single data set as for α. This is discussed further below.

4.4.4 Controls

To verify that the membrane defects were causing the anomalous behaviour two of controls were performed.

4.4.4.1 Rescue of anomalous behaviour

An SLB containing 2.6 mol% PEG(2K)-DPPE and single molecule levels of TR-DHPE was formed and imaged using TIRFM as per Chapter 2. DOPC only SUVs were then added to the volume above the SLB and incubated for 10 minutes. Excess vesicles were washed away and the SLB was again imaged using TIRFM. Figure 4.10A shows the change in diffusive behaviour to normal behaviour after the addition of the SUVs. This result was also confirmed by FRAP (B) where after incubation the recovery profile returns to that of a DOPC only SLB and can then be fit with a Bessel function to assess diffusivity. This fitting method is only applicable to bilayers exhibiting normal diffusion and as such, the bilayer containing PEG(2K)-DPPE at 2.6 mol% was not quantified.

4.4.4.2 DIBs do not exhibit anomalous behaviour

DIBs were formed which included 0.0, 2.6 or 5.0 mol% PEG(2K)-DPPE and single molecule levels of TR-DHPE. TIRFM and diffusion analysis were completed as detailed in Chapter 2. Figure 4.11A shows that in each case the diffusive behaviour is normal. For reference, the equivalent plots for the SLB are shown in panel B. It can be seen that for the same lipid composition the diffusive behaviour is much more anomalous in SLBs.

4.4.5 Monte Carlo simulations

Using the unit cell described in Section 2.4.4 and depicted in Figure 4.12A, all diffusion analysis previously described was carried out on simulated data. Panel B shows that the simulations of increasing EAF exhibit the same $\langle \Delta r^2 \rangle / 4\Delta t$ *vs.* Δt behaviour as iSCAT in that there are two diffusion modes; normal diffusion at short timescales undergoes a crossover transition to exhibit anomalous behaviour in the millisecond to seconds regime.

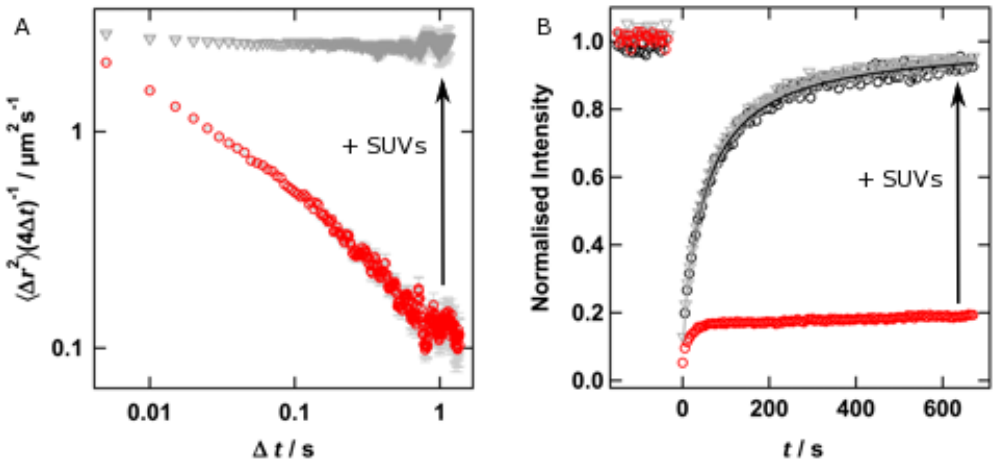

Figure 4.10: **Normal diffusive behaviour can be rescued.** (**A**) Single-particle tracking of anomalous diffusion was repeated on a SLB exhibiting anomalous behaviour (red). This bilayer was then incubated with DOPC SUVs. The additional vesicles ruptured within the defects, repaired the bilayer and returned normal diffusive behaviour (grey). (**B**) FRAP shows similar behaviour, with 2.6% PEG(2K)-DPPE bilayers exhibiting a large immobile fraction (red). Upon addition of DOPC SUVs, diffusion again recovers (grey triangles, $D = 1.75$ μm^{2}s^{-1}, mobile fraction 0.99) to values comparable to a pure DOPC bilayer (black circles, $D = 1.81$ μm^{2}s^{-1}, mobile fraction 1.00).

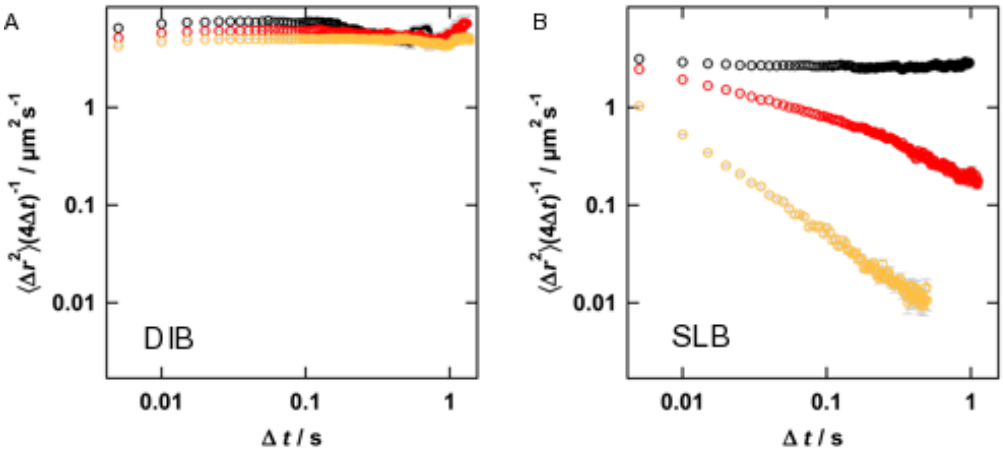

Figure 4.11: **Diffusive behaviour in DIBs remains normal.** (**A**) Droplet interface bilayers (DIBs) [84, 85] were used to create unsupported lipid bilayers and confirm that PEG-lipids alone do not cause anomalous behaviour. In DIBs, defects would result in conductance across the bilayer, unstable droplets and ultimately bilayer rupture [92]. Following our previous methods [85], 'lipid-in' DIBs (2.6 or 5.0 mol% PEG(2K)-DPPE; $\sim 10^{-6}$ mol% TR-DHPE) were formed. Single-particle tracking using TIRF microscopy showed normal diffusion even for 5.0 mol% PEG-DPPE, well above the threshold value for anomalous behaviour in SLBs. Bilayers containing 0 (black), 2.6 (red) and 5.0 (yellow) mol% PEG(2K)-DPPE all exhibit normal diffusion. (**B**) For reference the plots for equivalent compositions in SLBs exhibit anomalous behaviour.

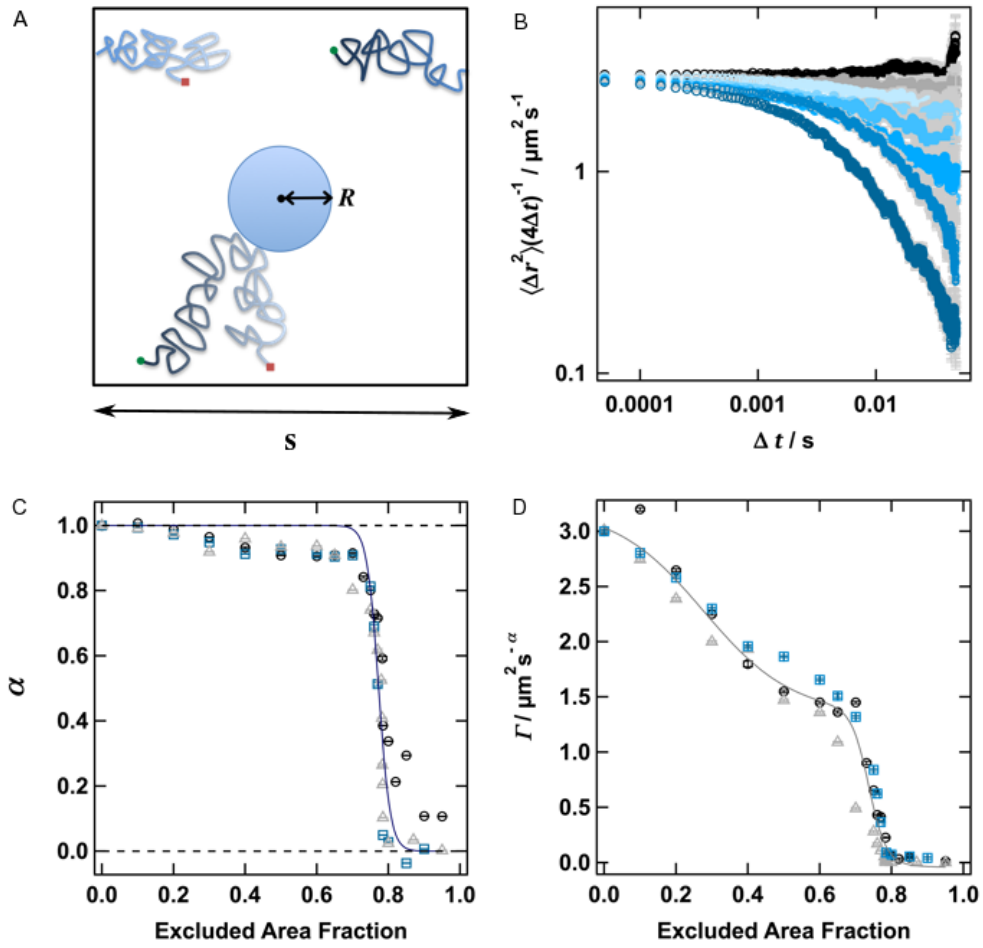

Figure 4.12: **Monte Carlo simulations of anomalous diffusion**. (**A**) Schematic of the unit cell. (**B**) Diffusion analysis of the resultant tracks from simulations with excluded area fraction increased from 0 (black) to 0.9 (bottom most curve, dark blue). These showed similar behaviour to experiment. (R = 500 nm, D = 3 μm^{2}s^{-1}). A similar trend to experiment was also present for α (**C**) and Γ (**D**) for R = 150 nm, 500 nm and 1 μm (grey triangles, black circles, teal squares respectively).

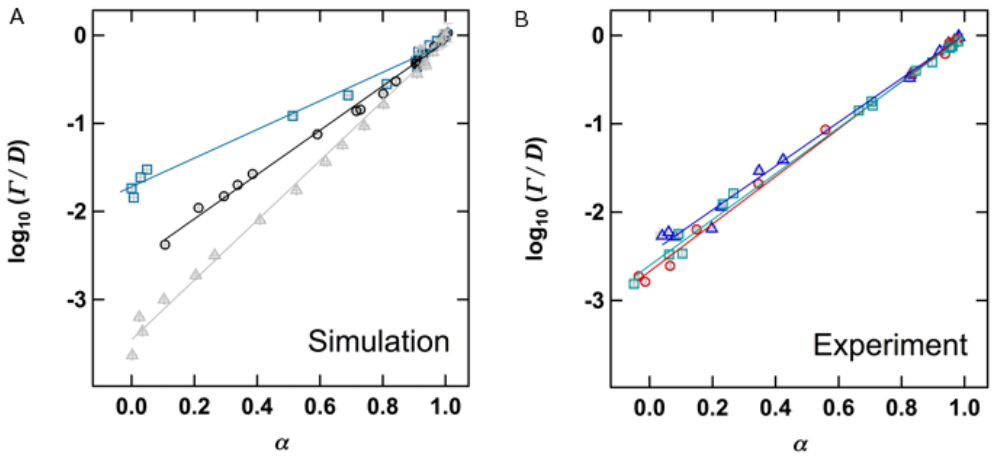

Figure 4.13: **De-dimensionalisation of the data.** (**A**) Plots of $\log_{10}(\Gamma/D)$ *vs.* α show the expected linear relation, dependent on obstacle size. $R = 150$ nm (grey triangles), 500 nm (black circles) and 1 µm (teal squares). (**B**) Similar plots for our experimental data show an essentially static linear relationship for different PEG lengths. PEG(1K)- (blue triangles), PEG(2K)- (red circles) and PEG(5K)- (green squares).

Similarly, for three different series of simulations with different obstacle sizes, the data follow a sigmoidal trend in α *vs.* EAF which overlay and can be fitted with a single sigmoid (refer to Figure 4.9C for equivalent experimental data). However, in the case of Γ, the data for all obstacle sizes can be fit by one double sigmoid function. The fit midpoints can be found in Table 4.4.

Table 4.4: **Simulation sigmoid fit midpoints.** Midpoints extracted from the sigmoid fit of the α *vs.* excluded area fraction (EAF) (Figure 4.12C) and Γ *vs.* EAF (Figure 4.12D) plots. Figure 4.12C was fitted with a single sigmoid, whereas Figure 4.12D was better fit by a double sigmoid.

	EAF 1	EAF 2
α	-	0.773 ± 0.002
Γ/ µm^2 s$^{-\alpha}$	0.277 ± 0.001	0.737 ± 0.001

4.4.6 De-dimensionalisation

De-dimensionalisation of both the experimental and simulated data was completed as described in Section 4.3. Figure 4.13 shows different linear relationships for the

three simulated obstacle sizes, this results in three characteristic length scales as summarised in Table 4.5. These are approximately half of the diameter specified in the simulation. The experimental data on the other hand, largely fits on a single line and when each is fit with a straight line, the λ values are similar. This is also true of the average FWHM values from the AFM auto-correlation however the values are smaller (see Table 4.5).

Table 4.5: **Anomalous length scales (λ) for simulation and experiment.** Length scales extracted from the linear fit of the $\log_{10}(\Gamma/D)$ *vs.* α plots for simulation and experiment (Figure 4.13A and B respectively).

Simulation			
R / nm	150	500	1000
λ / nm	65 ± 3	177 ± 7	479 ± 24
Experiment			
PEG / kDa	1	2	5
λ / nm	196 ± 4	145 ± 2	160 ± 3
AFM FWHM / nm	54 ± 8	56 ± 2	62 ± 8

4.5 Discussion

We successfully exploited disruption of bilayer formation by PEG-lipids to form lipid bilayers which exhibit anomalous behaviour. AFM imaging confirmed that the introduction of PEG(2K)-DPPE resulted in defects and patches and the same trends were confirmed for PEG(1K)- and PEG(5K)-DPPE containing bilayers. Force curve testing was completed on the 0.0 and 2.0 mol% PEG(2K)-DPPE samples which confirmed that a bilayer was present (Figure 4.5). Owing to the coverage of the defects at concentrations greater than this, force curve tests were not completed. For small membrane patches, the cantilever easily displaced the material and did not show the typical *punch through* behaviour. The shape, size and height of the features seen at high PEG mole fractions are not consistent with individual vesicles and therefore it was reasoned that the features were indeed bilayer patches. In the previous work by

Kaufmann *et al.* it was shown that the PEG-lipids must be below the concentration which induces a mushroom-brush transition in the polymer chains. Using the theory outlined above, it was confirmed that the majority of the concentrations used in the present study were below the predicted transition and therefore likely to produce bilayers rather than an adsorption of vesicles. The appearance of the bilayers for the two experiments, 3.0 and 3.5 mol% PEG(5K)-DPPE, which appear to enter the brush regime, did not differ from the upper concentrations of the other PEG lengths by AFM imaging. As the levels of PEG(1K)- and PEG(2K)-DPPE are all below or within this transition it is assumed that bilayer patches do form for 3.0 and 3.5 mol% PEG(5K)-DPPE and confinement at these concentrations is not a result of adsorbed vesicles. Concentrations corresponding to the interesting transition in anomalous behaviour, and biologically relevant α values, fall below the brush transition for all three PEG lengths.

For consistency, thresholding was completed to the automatic level as outlined in the methods. The sigmoid fits of the excluded area fraction calibration were required to limit at zero and one, however the exact PEG-DPPE fraction which resulted in no bilayer formation was not found experimentally. Radial profiling was chosen instead of line profiles so that any large inhomogeneity in the sample, or imaging artefacts (such as stripe artefacts in the direction of tip movement), did not skew the results. It was determined that the Lorentzian fit was better than a Gaussian fit and therefore was taken forwards for analysis of all radial profiles. Owing to the slight decrease in FWHM as PEG-DPPE fraction increases it was thought that this metric reports the smallest correlated feature size. It is possible that defects are correlated when there are large homogeneous patches of bilayer (at low PEG-DPPE fractions), but at once defects become percolated, the smaller patches could be correlated instead. Therefore further work would need to be completed in optimisating the correlation to find an accurate relationship of PEG-DPPE fraction with defect size. This was not completed here, as the data still show that the different lengths of PEG do not result in different correlation lengths, which was the purpose of the analysis. As the trend in FWHM *vs.* EAF for each PEG length are largely the same (Figure 4.6), average FWHM values were reported from comparison with the other extracted length scales in Table 4.5.

The $\langle \Delta r^2 \rangle / 4\Delta t$ *vs.* Δt plots show curves of increasingly anomalous character as more PEG-DPPE is introduced. Yet as expected, these plots varied for equivalent experiments run using fluorescence and iSCAT owing to the different timescales

sampled. The fluorescence experiments sample a timescale in which the diffusive behaviour is alway anomalous. Towards short time scales this suggests that the sampling rate is not sufficient to detect a cross over from normal diffusion seen in cells [48] and in SLBs using iSCAT [68]. This result was confirmed by iSCAT imaging undertaken on the PEG bilayers which shows the transition between normal behaviour below 1 ms and anomalous behaviour above. Due to the limitations surrounding data volume, discussed in Chapter 3, the iSCAT data cannot sample more than 3 orders of magnitude in time. Therefore it was necessary to combine this technique with fluorescence to see the cross over and confirm anomalous behaviour over several seconds.

For a particular mole fraction of PEG, the fluorescence and iSCAT data in the $\langle \Delta r^2 \rangle / 4\Delta t$ *vs.* Δt plots and in the analysis of Γ values do not line up owing to the slow initial rate of diffusion for the large gold nanoparticle compared to the fluorescent probe. As previously mentioned, this also resulted in a limit to the mole fractions which could be studied using iSCAT. Insufficient movement of the particle resulted in poor background subtraction and therefore poor SNR and localisation. However as the iSCAT data demonstrated that the cross over time for a number of mole fractions each for PEG(1K),(2K) and (5K) was the same, no information was lost in the limited sampling range.

Timescales beyond the onset were chosen for analysis of α and Γ to allow a comparison between fluorescence and iSCAT data. Despite the limitations mentioned above, when α values were compared the iSCAT data overlaid with the fluorescence sigmoids. Table 4.3 illustrates that the midpoints of the sigmoids for iSCAT are within 6% of the corresponding fluorescence fit. When α is related to excluded area fraction, a single trend could be seen for all PEG lengths for both iSCAT and fluorescence data (Figure 4.9C). It is therefore reassuring that the same diffusive behaviour can be detected via two optical techniques which goes somewhat to addressing Saxton's request for reproducibility between methods. However, because the pure diffusion coefficient of the tracers has slight variation (see Table 4.2) the plots for Γ correlate less well. As expected, iSCAT shows slower pure diffusion coefficients, which later tend towards the sigmoid produced by fluorescence. For this reason, it was not appropriate to fit a single sigmoid to both the fluorescence and iSCAT data when the relationship between Γ and EAF was graphed.

Several pieces of evidence support the assertion that it is the bilayer defects which cause the anomalous behaviour and not the presence of the PEG-DPPE itself acting as an immobile obstacle. Firstly, normal diffusion was rescued by filling in the bilayer defects. This was confirmed by both single molecule and bulk fluorescence techniques

(Figure 4.10). Secondly, no anomalous diffusive behaviour was seen in DIBs for PEG-DPPE levels corresponding to significant anomalous behaviour in SLBs. In DIBs the bilayer must be contiguous with a GΩ seal or the droplet will be unstable and immediately burst. As the droplets were stable for over an hour it can be assumed that the bilayer was contiguous. Thus the presence of PEG-DPPE is not sufficient to cause anomalous behaviour. Finally, for the experimental data, de-dimentionalisation resulted in characteristic lengths varying by less than 20%, compared to the large variation of the three distinct lines seen for the simulation of different obstacle sizes. The simulation shows that varying obstacle (defect) size should result in different characteristic length and timescales (Figure 4.5A). Therefore for the experiment we expect there to be a length scale which remains largely the same across SLBs despite a change in PEG-length. This is consistent with the trend in reported length scales from FWHM analysis of the AFM data (although the magnitude is not the same).

Further understanding of the relationship between α and excluded area fraction was supplied by study of the simulations. For a square lattice model, confinement occurs when the obstacle diameter is equal to the size of the unit cell, s. This is equivalent to an excluded area fraction of $\frac{\pi}{4}$ (0.785) and it can be seen that a transition in α *vs.* EAF is evident close to this threshold (0.773 for the midpoint and 0.808 for $\alpha = 0$). If a parallel is drawn with the experimental system the equivalent transition occurs at an excluded area fraction of 0.232 ± 0.054. In the experimental case, there is no lattice so it is expected that this value is different to the simulation. By treating α as a measure of the probability of being confined, it can be reasoned that the mid-point is indicative of the percolation threshold. Thus the experimental percolation threshold occurs around an excluded fraction of 0.232.

In previous molecular dynamics simulations [60] and experiments in cell membranes [48, 135, 136, 137, 51], it has be shown that α values in membranes span a wide range (typically 0.45 - 0.7). Therefore it is necessary for a model to dial-in almost any value of α. Using this model, specific and controlled changes to excluded area can be made which allows this, providing an opportunity to use this simple model to recreate the levels of anomalous diffusion observed *in vivo*. As such, overall the SLB system satisfies most of the requirements set out by Saxton and listed at the start of this chapter. Firstly, the simplicity of an SLB system satisfies point 1, with the buffer being sufficiently pure to satisfy point 7. Four orders of magnitude in time, from hundreds of microseconds to seconds, were spanned by the combination of iSCAT and fluorescence (points 2 and 3). iSCAT could differentiate between the normal diffusive mode at short time scales and the crossover to anomalous behaviour

(point 8). The anomalous exponent was highly tuneable by careful control of PEG-DPPE levels which evidence suggests is a result of immobile obstacles in the form of bilayer defects (point 4). Although no NMR analysis was undertaken for this study, detection by a number of techniques using different tracers partially addresses point 6. Recent production of a single fluorescent tag-gold construct [128] for conjugation to lipids, would allow for simultaneous imaging and direct comparison of the two data sets.

Although the timescales are biologically relevant, as the characteristic timescale is related to the defect size and not diffusible area, point 5 is only partly addressed by this model. It is also important to stress that the model does not mimic the mechanisms of anomalous behaviour *in vivo*, rather just the extent. Confinement in cell membranes cannot be created by membrane defects as this would compromise cell integrity. However, it is likely that the excluded area created by membrane proteins and their interactions with lipids contributes to the anomalous behaviour and therefore a parallel is drawn with this work.

It is predicted by theory that the return to normal behaviour at long timescales, albeit with a reduced diffusion coefficient, is a consequence of finite hierarchy [138]. Such transitions were observed at around 100 ms for compartments in cells [48] of comparable size to those extracted from this model. As a second crossover back to normal behaviour was not observed for this system, it only satisfies one sub-case of criterion (8). In this way, the PEG-SLB model differs from cells which must exhibit a finite hierarchy of compartment sizes. For this to be true of the PEG-SLB model, additional control of bilayer defect formation would be necessary. This may be possible by engineering compartments of defined size by for example, nano-patterning of the substrate before SLB formation [139], such that a defined excluded area and hierarchy of compartments results in predictable anomalous behaviour.

4.6 Conclusion

In this chapter, a simple experimental model was presented which exhibits defined anomalous behaviour chosen by incorporation of particular quantities of PEG-lipids. The mechanism by which the PEG-lipids cause this behaviour was determined to be disruption of bilayer formation resulting in excluded area which acts as immobile obstacles. This model part answers the call for a simple and reproducible experimental model with readily tuneable anomalous behaviour over the length scales observed *in vivo*. It would also be possible to further expand on this work by using the relationship

of α with excluded area to produce further, more complex models in which area is excluded by different means, for example by an immobile protein fraction, meshwork or impassable lipid domains.

Chapter 5

Controlling Anomalous Diffusion in Artificial Membranes Using Urea

Work presented in this chapter was completed in collaboration with E.E Weatherill and forms the basis of the paper cited in Appendix A. EEW produced the bilayers and performed the TIRF imaging, HLEC completed all analyses.

5.1 Introduction

In the preceding chapter, defect formation within the bilayer was shown to induce anomalous behaviour in lipids. It was argued that this experimental model could be used to select a particular α value for example to mimic the extent of anomalous behaviour apparent in biological membranes. Here, urea was used as a chaotropic agent to disrupt the bilayer after formation. Urea is often used as a denaturant in protein folding studies. It is known to alter the physical properties of bilayers, in particular exerting a stabilising effect on liquid crystalline lipid phase [140, 141, 142, 143]. This chapter describes initial work into the effect of urea on the diffusion of lipids within supported lipid bilayers, both in a time and concentration dependent manner. The feasibility of using urea to control the extent of anomalous behaviour is discussed.

5.2 Specific methods

5.2.1 Materials

1,2-dicapryl-*sn*-glycero-3-phosphocholine (DCPC) was purchased from Avanti Polar Lipids (Alabaster, AL). All other materials are detailed in Chapter 2. Temperature

during formation and imaging was maintained at 37 °C to ensure that the bilayer was in the liquid phase.

5.2.2 SLBs

The general SUV and SLB preparation methods are detailed in Section 2.2.1. Changes to these methods are as follows: SUVs were prepared from 1.77 mM DCPC with 1.0 mol% PEG(5K)-DPPE and 3×10^{-6} mol% TR-DHPE. For SLB formation, the coverslip was heated to 37 °C before immediate addition of 50 µl of SUV stock diluted 1:1 in buffer (250 mM NaCl, 10 mM EDTA, 20 mM Tris pH 7.0). The vesicles were incubated for 30 minutes at 37 °C before the membranes were washed thoroughly with degassed MilliQ water followed by buffer.

Urea was added or removed by buffer exchange, which involved removing all but $\sim$ 50 µl of fluid from the sample well and replacing it with 200 µl of the new buffer (containing 0.2, 0.5 or 1M Urea), a minimum of 5 times. Bilayers were imaged 15 seconds after buffer exchange.

5.2.3 TIRF imaging

The microscope objective was heated to maintain 37 °C at the sample. TIRF imaging was completed as per the general method (Section 2.3.1) except with 20 ms exposure time and stacks of 5000 frames.

Image stacks were tracked as outlined in Section 2.4.1 and MSD analysis undertaken as in Section 2.4.3.1.

5.3 Results

Highly mobile supported lipid bilayers were successfully formed from DCPC. These bilayers, when cushioned by 1 mol% PEG(5K)-DPPE, exhibited a diffusion coefficient of around 6 $\mu m^2\ s^{-1}$ and an anomalous exponent of 1.01 $\pm$ 0.01, indicating normal behaviour. $\langle \Delta r^2 \rangle\,(4\Delta t)^{-1}$ *vs.* Δt plots were produced to illustrate the diffusive behaviour and the parameters α and Γ were extracted as previously described.

5.3.1 Urea slows diffusion in a concentration dependent manner

Urea was titrated into the buffer surrounding the SLB incrementally from 0 to 1 M. This caused the diffusion to slow as shown in Figure 5.1A. However, over this

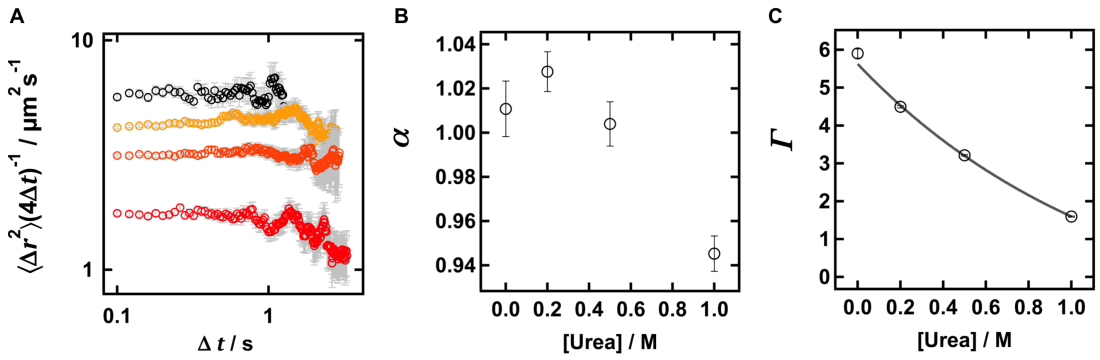

Figure 5.1: **Effect of urea concentration on lipid diffusion. (A)** $\langle \Delta r^2 \rangle (4\Delta t)^{-1}$ *vs.* Δt plot showing diffusion slows as urea concentration increases from 0 (black) to 1 M (red) with 0.2 M (yellow) and 0.5 M (orange). **(B)** α shows a modest decrease as concentration increases, but suggests that the diffusion is largely normal. **(C)** Γ decreases exponentially, with Γ halved at 0.55 M urea. Error bars throughout represent standard errors from a minimum of 250 tracks.

concentration, the behaviour remained normal (panel B) with only a slight decrease in α from 1.03 to 0.94. This could be fit with a line revealing a rate of 0.1 M^{-1} once urea was added. As expected for a linear relationship in α, Γ decreases exponentially.

5.3.2 Urea induces anomalous behaviour in a time dependent manner

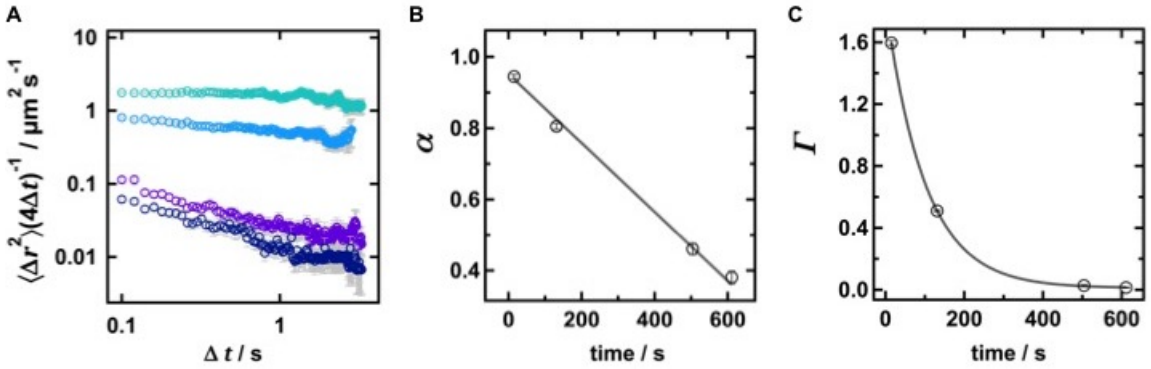

Figure 5.2: **Time dependence of anomalous behaviour induced by 1 M urea. (A)** $\langle \Delta r^2 \rangle (4\Delta t)^{-1}$ *vs.* Δt plot showing anomalous subdiffusion increases over time from 15 seconds (turquoise), through 131 s (light blue), 504 s (purple) to 611 seconds (dark blue). **(B)** α decreases linearly with a rate of 9.7 x 10^{-4} s^{-1}. **(C)** Γ decreases exponentially, $t_{\frac{1}{2}}$ = 69 s. Error bars throughout represent standard errors from a minimum of 250 tracks.

Upon the addition of 1M urea to the buffer above the SLB diffusion became more anomalous in a time dependent manner, as evident in the $\langle \Delta r^2 \rangle (4\Delta t)^{-1}$ *vs.* Δt plot

(Figure 5.2A). α decreased linearly with time from 0.95 to 0.38 at a rate of 9.7 x 10^{-4} s^{-1} (panel B). Again, an exponential decrease in Γ to 0.01 μm^2 $s^{-\alpha}$ accompanied this trend in α (panel C). Very low Γ values (less than 0.03 μm^2 $s^{-\alpha}$) did not correspond to an α value of 0 indicative of confinement, but rather α = 0.38 to 0.46. This is discussed further below. The effect of the urea was irreversible, with anomalous behaviour exhibited even after 3000-fold dilution during buffer exchange.

5.3.2.1 Confinement evident in the particle locations

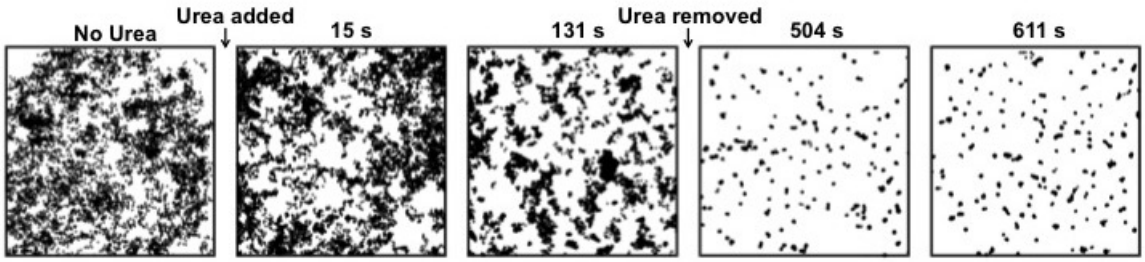

Figure 5.3: **Time course of spot locations from tracked particles.** Before addition of 1 M urea (left) and for four time points after addition. Image size 3×3 μm.

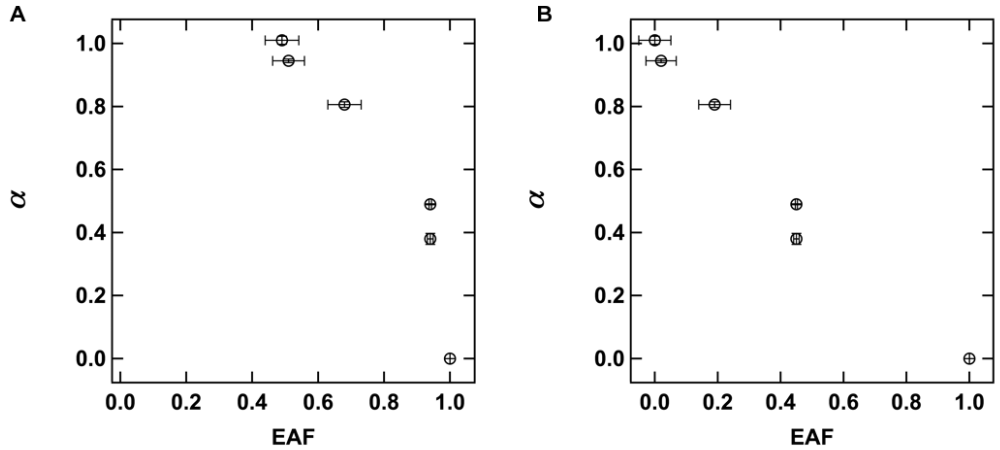

Figure 5.4: **Relationship of the anomalous exponent with estimated EAF. (A)** EAF was estimated by thresholding of the particle track images shown in Figure 5.3. **(B)** Points normalised for expected tracer density artefacts. In both panels the data point at (1,0) is theoretical and not confirmed experimentally.

Visualisation of the particle locations from the time course experiment suggest confinement. It can be seen in Figure 5.3 that over time particles exhibit smaller displacements and do not traverse a significant proportion of the image. This confirms the trends seen in the MSD analysis (Figure 5.2). Image autothresholding, similar

to that described in Chapter 4, was completed on the spot location images as an estimation of excluded area fraction. It is evident from Figure 5.4 that this results in a complex behaviour not easily fit with a single sigmoid (as for the PEG-lipid model in the previous chapter). This method of estimation suggests that there is a significant excluded fraction within the bilayer even before addition of urea. This is likely to be an artefact of the tracer density (discussed further below) and normalisation for this (by subtraction of 0.49) results in a shift of the data points as shown in Figure 5.4B.

5.3.3 De-dimensionalisation

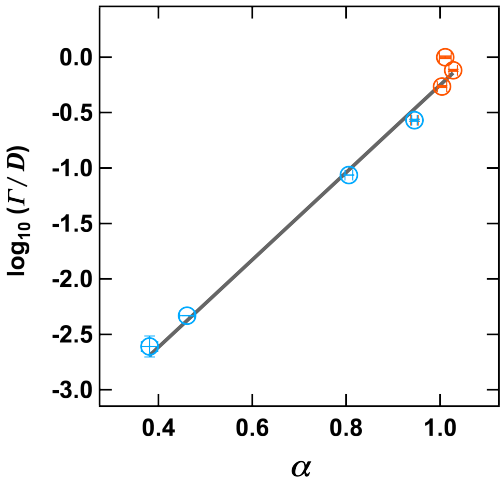

Figure 5.5: **De-dimensionalisation of the data to extract a length scale.** Time course (blue) and titration (orange) data are fit with a single line to extract the time scale τ and corresponding length scale λ.

Following the de-dimensionalisation theory outlined in the previous chapter, characteristic time and length scales were extracted from the data (Figure 5.5). Both data sets were used for the fit revealing a time scale (τ) of 86 μs and corresponding length scale (λ) of 45 nm.

5.4 Discussion

The concentration dependence observed between 0 and 1 M urea could be used to modulate Γ without a large change in α. Further work would need to be completed to assess any time dependance of α at low concentrations of urea and determine if anomalous behaviour is eventually induced. If a time dependance is not evident, or is sufficiently slow, this urea SLB model may be useful to dial in a particular reduction

in the diffusion coefficient in the absence of anomalous behaviour. This could be used to modulate the motion of particles for imaging at slower frame rates or to control the rate of reactions of bilayer associated molecules.

A time dependent increase in anomalous behaviour was observed upon the addition of 1 M urea. The extent of the anomalous behaviour, exhibited some time after urea addition, can be easily predicted from the linear relationship. The effect is evident over seconds to tens of minutes which makes this a workable model over experimental timescales. However, the effect on the diffusive behaviour was irreversible and seemed to progress despite the removal of urea from the bulk solution. Either the dilution procedure for removal was not sufficient, or there is a direct interaction of urea with the bilayer. It is possible that urea associates with the bilayer with high affinity resulting in an off rate slower than the half-life for the process as determined by the decay of Γ (Figure 5.2C). Although urea is unable to permeate lipid bilayers, there is some evidence to suggest that urea remains in the vicinity of the bilayer in multilamellar systems [141] which might extend to SLB systems.

A complex trend was evident for α in Figure 5.4 when compared to estimated excluded area. This suggests that EAF is not accurately estimated from the particle tracks. One would expect that the untreated bilayer would exhibit an EAF of approximately zero (as shown for the PEG bilayers in the previous chapter). Here however, the EAF for $\alpha = 1$ was 0.49. It is possible that the SPT method introduces this artefact as low concentrations of tracer were used to ensure single molecule spot detection. Thus artificially low EAF could be a result of low tracer density. One might expect that with equilibration and long imaging times in highly mobile bilayers, particle locations would show a good representation of the surface accessible to diffusion. However here, because of the time dependance of the effect of urea, it is not possible to achieve this. If it is assumed that this EAF of 0.49 is an artefact of tracer density and is actually representative of a contiguous, defect free bilayer, it is possible to adjust the EAF values. As such, Figure 5.4B was obtained. From this the percolation threshold might be expected around an EAF of 0.45. More data points would be needed to fully elucidate that trend. It is important to note that this results in a rough estimation of EAF and further work using a method such as AFM or SEM would be needed to fully understand the structures of the bilayers. This could not be completed in time for this submission. As such, direct comparison with the PEG system in terms of EAF is difficult, owing to this speculative approach used to calculate EAF.

Some of the α values were calculated to be greater than 1, indicative of slightly super-diffusive behaviour. This is unusual for lipid bilayer systems and, considering the errors in these values, is likely to be an artefact of the fitting. Large errors in the MSD analysis for times greater than 1 second could account for this. Few tracks are long enough for analysis over this observation time and therefore statistical errors are greater. More data would be required, which if photobleaching is the limiting factor, could be completed using iSCAT. Despite this, importantly no anomalous behaviour was seen at urea concentrations lower than 500 mM. Refolding studies of B-barrel proteins often employ urea as a denaturant. This work highlights a phenomenon which should be considered when designing model membrane experiments where urea is used at concentrations above 500 mM and therefore could exert unwanted effects.

The results outlined in this chapter suggest that the mechanism by which urea induces anomalous behaviour is different to that of the PEG system. The slowing of Γ to less than 0.03 $\mu m^2 s^{-\alpha}$ during the time course experiment, without α values corresponding to confinement, may indicate another interaction with the lipids of the bilayer. This could be a mechanism of association which reduces the transport coefficient but does not induce anomalous behaviour until a sufficiently high concentration at the bilayer. It would be interesting to determine local urea concentrations at the bilayer to assess this. In addition to this, different time scales were extracted from the de-dimensionalisation for each model. It is therefore likely that disruption of a bilayer during formation (PEG model) results in different defects and patch sizes compared to a bilayer disrupted after formation (urea model). The progression of anomalous behaviour after urea removal suggests a general destabilisation of the bilayer rather than discrete defect formation. In the previous chapter, reversibility was demonstrated by the addition of further SUVs. This method could be tested on this model to determine whether it is possible to (a) halt the progression of the anomalous behaviour at a particular level or (b) 'heal' the bilayer to reverse the destabilisation and return to normal diffusive behaviour.

DCPC is a short chain lipid which is thought to improve insertion of certain membrane proteins by reducing hydrophobic mismatch [144, 145]. An alternative interpretation of the results suggests a mechanism by which urea alters the lipid phase behaviour of these lipids, inducing phase co-existance [140]. The decrease in the area fraction of mobile lipids could correspond to stabilisation of less mobile liquid ordered regions. However, the literature suggests that urea stabilises the liquid disordered phase [140, 141], suppressing phase separation, rather than encourage it. It is possible that urea does not interact with the bulk lipid, but with the PEG-lipids

introduced to elevate the membrane from the substrate. This was not determined in this study and further controls (without PEG-lipids) would need to be undertaken to resolve this. Additionally, a number of other SLB forming lipids, such as DOPC, and more biologically relevant compositions, could be tested to determine if urea can be used to induce anomalous behaviour in these bilayers.

5.5 Conclusion

This chapter presents preliminary findings demonstrating another approach to induce anomalous subdiffusion and modulate slower normal diffusion in SLBs. This behaviour can be activated on demand by simple buffer exchange and results in a biologically relevant characteristic length scale. Unlike the PEG system, a complex time dependant behaviour makes this model more difficult to tune a particular anomalous behaviour. Further work would be needed to determine if there is a critical urea concentration at which anomalous behaviour is induced without the time dependant nature of the effect interfering with experimentation.

Chapter 6

Topography *vs.* Topology

Work presented in this chapter was completed in collaboration with M.R. Cheetham and M.C. Blosser, and forms the basis of the paper cited in Appendix A. MRC produced bilayers, performed the TIRF imaging and wrote the sine wave simulation. MCB wrote the rectangular wave simulation. HLEC produced bilayers, completed the gold labelling, iSCAT imaging and performed all analyses.

6.1 Introduction

Biological membranes can exhibit complex topography including nanotubules [146], coated pits [147] and within inner membranes such as the endoplasmic reticulum (ER) and Golgi [148]. It has been suggested that the 3D structure of cells introduces artefacts to SPT experiments which only measure a 2D projection of these surfaces [149]. In particular it has been warned that topography could cause apparent anomalous diffusion of components in cell membranes which, in reality, exhibit Brownian behaviour. As such, any SPT data suggesting anomalous behaviour should be analysed with care [150, 151]. Here, Monte Carlo simulations and a SLB based model were employed to systematically test the effect of membrane structure on SPT.

6.2 Theory

It is reasoned that topography alone *cannot* cause apparent anomalous diffusion but would result in a decrease in the observed diffusion coefficient. This has been seen previously for FCS analysis of diffusion of inner membranes (Golgi and ER) [152], but as yet has not been proven in a systematic experimental model and applied so SPT.

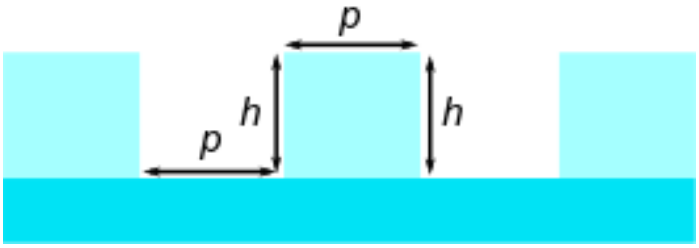

Figure 6.1: **Schematic of a rectangular wave** with height (h) and spacing (p).

In topographical systems, $\frac{\langle \Delta r^2 \rangle}{\Delta t}$ of many small time windows will be equal to that of a single large time window (normal diffusion). For topology, it will be reduced at long times due to the impassable barriers.

Equation 6.1 is the generalised form of Equation 1.2 which was introduced in Chapter 1.

$$\langle \Delta r^2 \rangle = 2nD_{ij}\Delta t \tag{6.1}$$

The experimental system was simplified by considering topographical surfaces in which the pattern was aligned along the x axis and the y direction was flat. This can be treated as a 2D surface being projected into one dimension along the x axis. Analysing tracks anisotropically, i.e. separately for the x and y directions, allows the separation of the effect of topography along each axis. The apparent path length (L*) of the particle will be shorter in the x direction than the actual path length (L) along this axis, or measured in the y direction, resulting in a different apparent diffusion coefficient D*. Thus D must be equal to D_{yy} and $D*$ is D_{xx}. As the diffusion is considered in one dimension only, $n = 1$.

$$\begin{aligned} L^2 &= \langle \Delta r^2 \rangle = 2nD\Delta t \\ L^{*2} &= \langle \Delta r^2 \rangle = 2nD^*\Delta t \end{aligned} \tag{6.2}$$

Equating for Δt and cancelling $2n$ results in the general equation;

$$\frac{L^2}{D_{yy}} = \frac{L^{*2}}{D_{xx}} \tag{6.3}$$

which can be used to determine the effect of different path lengths on the diffusion coefficients along each axis. Alternatively, measured diffusion coefficients can be used to estimate the path length of a topographical surface.

$$\sqrt{\frac{D_{yy}}{D_{xx}}} = \frac{L}{L^*} \tag{6.4}$$

6.2.1 Rectangular wave model

For a random walk in two dimensions over a rectangular wave, a particle would traverse one path length in the x direction over the distance $2p + 2h$ (Figure 6.1). However, if this is projected into one dimension, the apparent distance is $2p$. This can be substituted into Equation 6.3 to give the final form used for the rectangular wave model;

$$\begin{aligned} \sqrt{\frac{D_{yy}}{D_{xx}}} &= \frac{2p + 2h}{2p} \\ &= 1 + \frac{h}{p} \end{aligned} \tag{6.5}$$

Thus we can apply the rectangular wave model to simulation and experimental data by plotting $\sqrt{\frac{D_{yy}}{D_{xx}}}$ *vs.* $\frac{1}{p}$ to give an intercept of 1 and gradient of h.

6.2.2 Sine wave model

If considering a highly curved surface, a sine wave model may be more appropriate where $z(x) = \frac{h}{2} sin \frac{2\pi x}{2p}$. Using the first term of a Taylor expansion (quadratic) to estimate the path length in 3D along a sine wave surface, Equation 6.4 becomes:

$$\begin{aligned} \sqrt{\frac{D_{yy}}{D_{xx}}} &= \frac{\int_0^{2p} \sqrt{1 + (\frac{\partial z}{\partial x})^2}}{2p} \\ &= 1 + \frac{h^2\pi^2}{16} \left(\frac{1}{p}\right)^2 \end{aligned} \tag{6.6}$$

which can be fit with a quadratic where the coefficient $A = \frac{h^2\pi^2}{16}$ and y_0 is fixed at 1. Thus the height can be estimated from the quadratic coefficient.

6.3 Specific methods

SUV solutions containing 1 mg ml^{-1} DOPC with 10^{-6} mol% TR-DHPE and biotin-DPPE were used to form SLBs on the patterned substrates described below (formation method as per Chapter 2). TIRF microscopy, 40 nm gold labelling and iSCAT microscopy were completed as previously described.

6.3.1 Patterned substrates

Patterned glass substrates were created by e-beam etching at the University of Glasgow by Andrew Greer and Nikolaj Gadegaard. These took two forms; nanopillars and rectangular wave lines termed nanowalls.

6.3.1.1 Pillars

The nanopillar samples were designed to assess the iSCAT tracking and processing methodologies for 3D samples. A schematic of the glass sample is shown in Figure 6.2. Six areas contained a grid of pillars 200 nm tall, each of a different spacing (p). Box six, with ∞ spacing corresponds to an area etched to an approximately flat surface. This serves as a control to determine any diffusive behaviour which might be a result of the roughness of the glass subjected to the etching procedure.

6.3.1.2 Nanowalls

To create the anisotropic environment mentioned above, nanowall samples were etched as depicled in Figure 6.3. These samples were chosen to have a rectangular-wave like profile in the x direction and to be flat in the y direction. Again, each glass sample contained an array of six areas corresponding to different spacings. Four chips were produced with nanowall heights of 35, 50, 100 and 200 nm.

6.3.2 Anisotropic MSD analysis

Substrates were aligned on the microscope stage such that the nanowalls were parallel to the y direction. Herein, 'anisotropic MSD analysis' or 'anisotropic analysis' refers to MSD calculation in which the x and y dimensions are treated separately, and

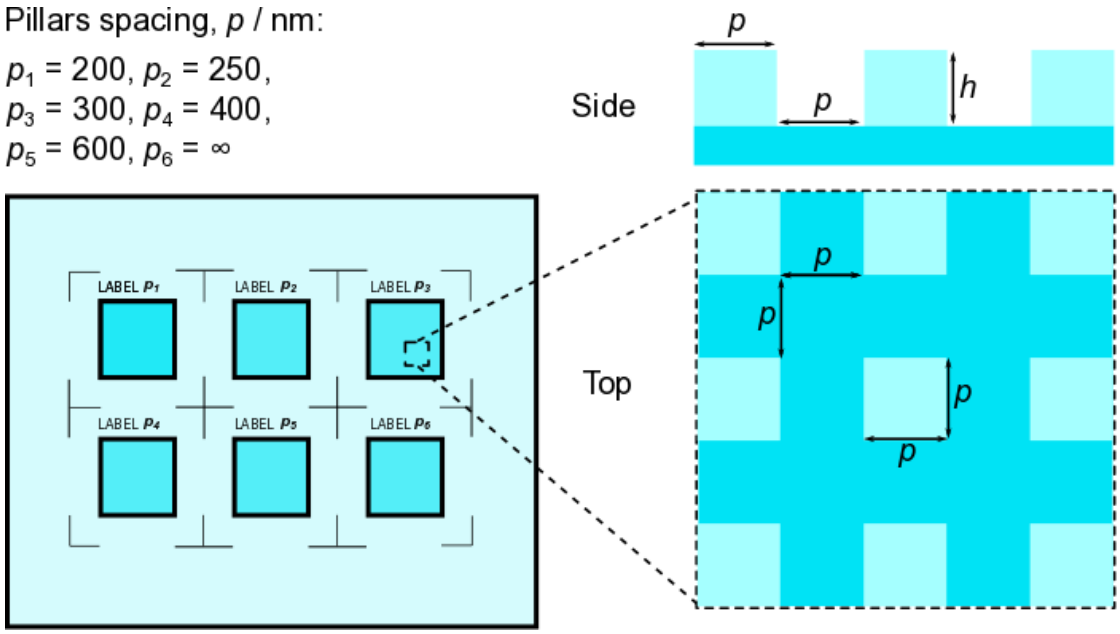

Figure 6.2: **Schematic of the pillared substrate.** Height (h) = 200 nm. Spacing (p) was varied as indicated in the legend.

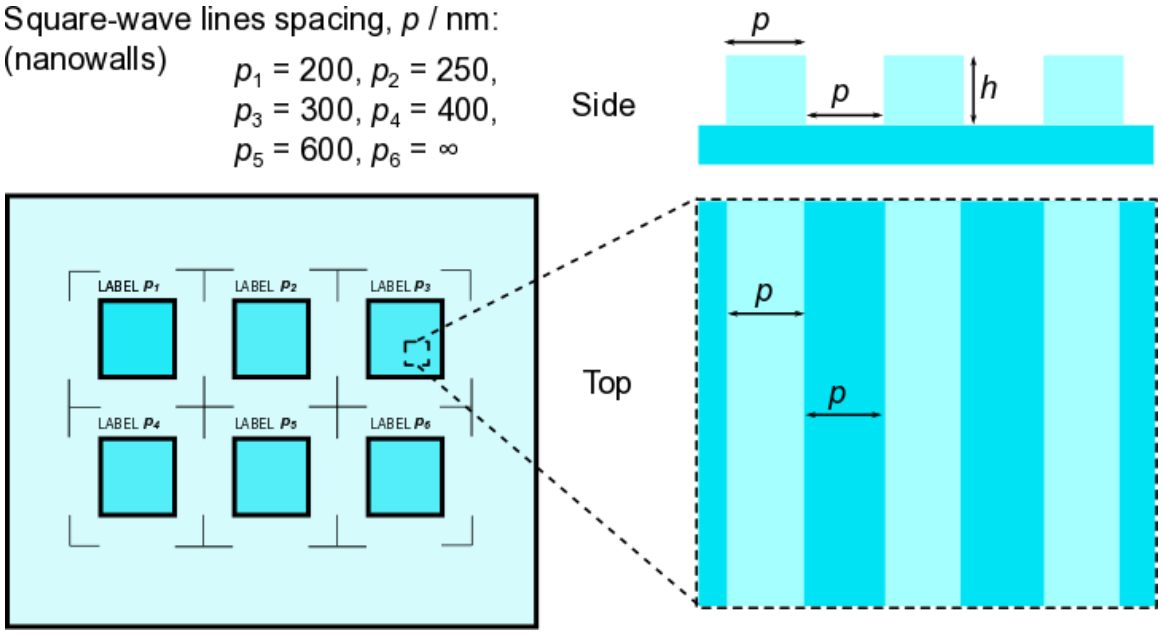

Figure 6.3: **Schematic of the nanowall substrate.** Four substrates as illustrated were produced each with a different height (h) 35, 50, 100 and 200 nm. Spacing (p) was varied as indicated in the legend.

each average second moment fit to give a separate diffusion coefficient. This was performed using MATLAB (see Appendix B) in accordance with Equation 6.1 such that the following quantities were each calculated individually and entered into a matrix as;

$$\begin{bmatrix} D_{xx} & D_{xy} \\ D_{yx} & D_{yy} \end{bmatrix}$$

With the sample properly aligned on the microscope, off-diagonal elements D_{xy} and D_{xy} were zero, if necessary, the matrix was diagonalised to find principal diffusivities in x and y, and the rotation angle.

6.3.3 iSCAT Analysis

The iSCAT instrument described in Chapter 2 was used for tracking at 2 ms time resolution to check the topography of the SLBs formed on the patterned substrates. The tracking plugin, TrackMate, is designed to track 'bright' spots on a dark background and as such, adaptation of the pre-processing was required to account for particles that change phase as they diffuse in the z-direction. After standard background subtraction as outlined in Section 2.3.2.2, the analysis methods were modified as follows;

To allow squaring of the image, the pixel intensities in each image stack were checked to ensure that the background had a pixel value of zero, the bright spots >0 and the dark spots <0. Adjustments were made as necessary using the 'Math' function in ImageJ. The pixel values were then squared such that dark spots became bright and therefore trackable. TrackMate was implemented with gap closing to negate the failure to detect spots when the particle contrast reached zero between the dark and light states. The resultant tracks were then read into a custom MATLAB script (see section B), along with the original background subtracted image (not squared). The script then used the code mentioned in Appendix B which extracts the pixel values associated with the detected spots using the maximum pixel method. These values were used to map the contours of the substrates.

6.3.4 Simulations

Differential geometry and a co-ordinate transfer functions are introduced as simple methods to simulate diffusion on sine and rectangular wave surfaces respectively.

6.3.4.1 Sine wave surface

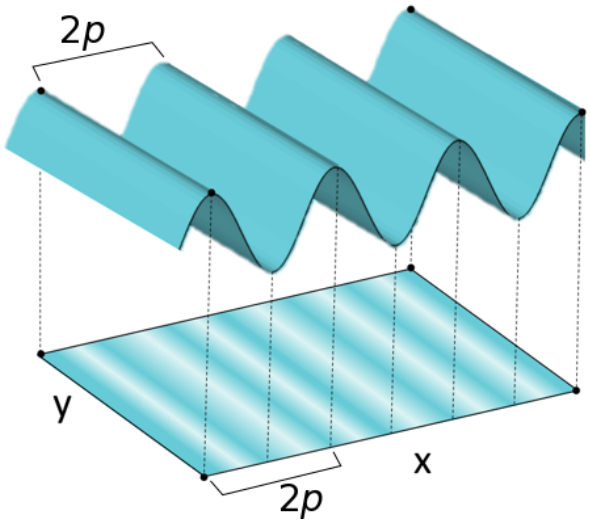

Figure 6.4: **Schematic of the projection of a sine waves onto a plane.** x and y axes as indicated with the path length equal to twice the spacing (p).

Covariant (dx_a curved space) is linked to contravariant (dx^b flat) space by;

$$dx_a = g_{ab}dx^b \tag{6.7}$$

where g_{ab} is the metric tensor of the form;

$$\begin{bmatrix} f(x,y) & 0 \\ 0 & 1 \end{bmatrix}$$

where g_{xx} is $f(x,y)$; the function which when integrated, describes the path length in the x direction. Here g_{yy} is equal to one because the surface is flat in the y direction.

Using $z(x)$ described above for the sine wave model and the amplitude set as half the height, h of the experimental sample, the metric $f(x,y)$ must be as follows;

$$\begin{aligned} f(x,y) &= \sqrt{1+\left(\frac{\partial z}{\partial x}\right)^2} \\ &= \sqrt{1+\left(\frac{\pi h}{2p}\right)^2 cos^2\left(\frac{\pi x}{p}\right)} \end{aligned} \tag{6.8}$$

Briefly, starting coordinates are generated for several particles on the 2D plane (*i.e.* in contravariant space) corresponding to the desired image. A random walk was then completed on the sine wave surface (covariant space). Each step in covariant space was converted to contravariant space using the inverse metric tensor, and added to the particle's previous contravariant co-ordinates. Images including laser and CCD noise were then generated from the tracks for tracking.

6.3.4.2 Rectangular wave surface

A similar script was created for a rectangular wave where a co-ordinate transfer function was used to created the projected particle co-ordinates. For the rectangular wave surface (depicted in Figure 6.1) p is defined as the spacing, h the height and s the arc length along the surface. Monte Carlo simulations produce trajectories in covariant space; each position is then mapped onto its corresponding position in contraviarant space using Equation 6.9:

$$x(s) = p\left\lfloor \frac{s}{p+h} \right\rfloor + \left(s - h - (p+h)\left\lfloor \frac{s}{p+h} \right\rfloor\right)\Theta\left(s - h - (p+h)\left\lfloor \frac{s}{p+h} \right\rfloor\right) \quad (6.9)$$

where floor and Heaviside theta functions are required. Each trajectory was simulated for 50 times longer than the longest lag time analysed. The mean square displacement was calculated by averaging square displacements for each non-overlapping lag time in each trajectory. Mean squared displacements from 100 trajectories are then averaged together. To derive the asymptotic diffusion coefficient, the average of diffusion coefficients over lag times greater than 0.5 seconds was used.

6.3.5 Fibronectin printing

As a control fibronectin was printed onto the top of the 200 nm height rectangular-wave sample to create immobile barriers to diffusion. Fibronectin was transferred to the samples using micro-contact printing [153]. To produce the stamp, a mixture of 10:1 Sylgard-184 elastomer and curing agent (Sigma-Aldrich) was poured over a clean glass coverslip placed in a plastic petri dish. The dish was placed under vacuum and degassed thoroughly before being removed and cured overnight at 60 °C in an oven. The stamp was carefully removed from the substrate using a sharp blade. A solution of fibronectin (Invitrogen Ltd., Paisley, UK) was prepared to 0.25 mg ml^{-1}

in PBS. The flat surface of the stamp was incubated in the solution for 15 min, rinsed with MilliQ and dried under nitrogen before immediately being brought in contact with a thoroughly cleaned nanowall substrate. The stamp was left in contact with the substrate for 5 minutes before careful removal. An SLB was then formed on the substrate following the usual procedures.

6.4 Results

6.4.1 Bilayers conform to substrate profile

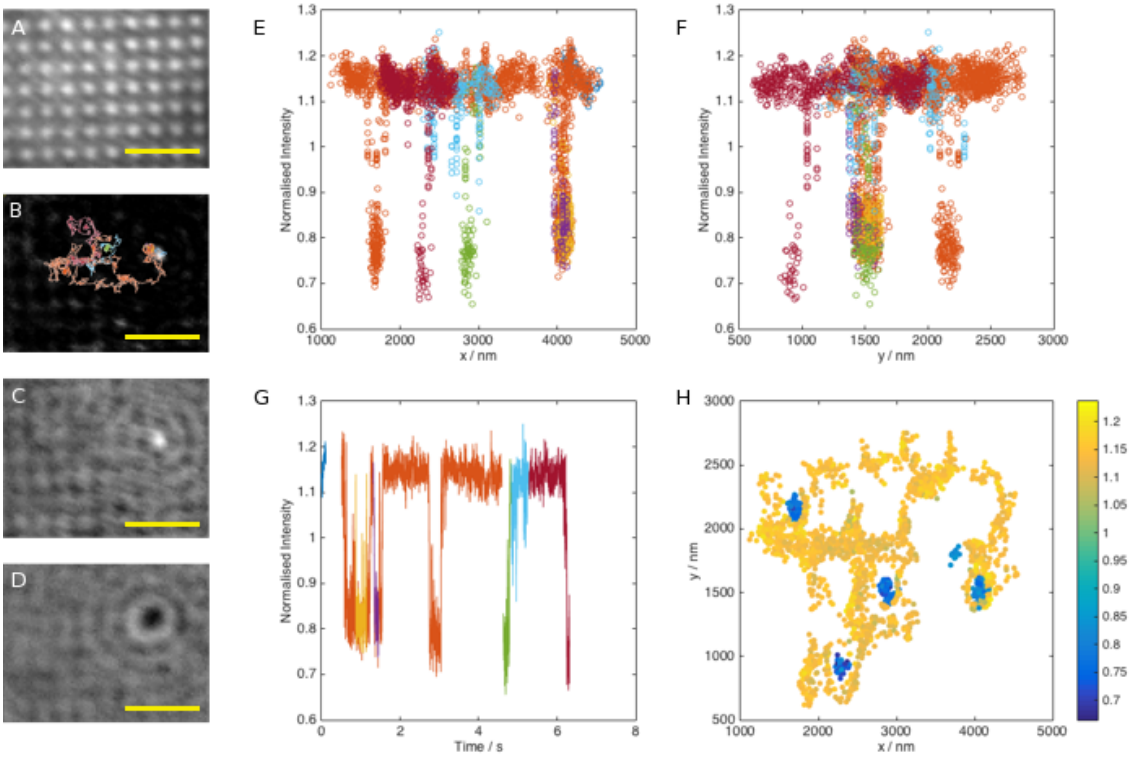

Figure 6.5: **iSCAT imaging of pillared substrate.** **(A)** Raw iSCAT image of 600 nm spacing pillar sample, height 200 nm. **(B)** Processed squared image used for tracking with an overlaid track. **(C&D)** Normalised images used for intensity extraction showing a bright spot (C) corresponding to an intensity of approximately 1.15 and dark spot (D) corresponding to an intensity of approximately 0.85. A-D scale bar 2 µm. **(E&F)** Intensity steps from dark to light as the particle traversed in the x direction (E) and y direction (F) at intervals consistent with the spacing of the pillars. **(G)** Intensity changes as tracks progress over the course of a 3159 frame video (frame time 2 ms). For B,E,F and G, colours correspond to a single track and are consistent across the four panels. It can be seen that a single track switches from light to dark as the particle travel over the pillars. **(H)** Structure of the substrate can be visualised by plotting the x and y coordinates coloured by intensity.

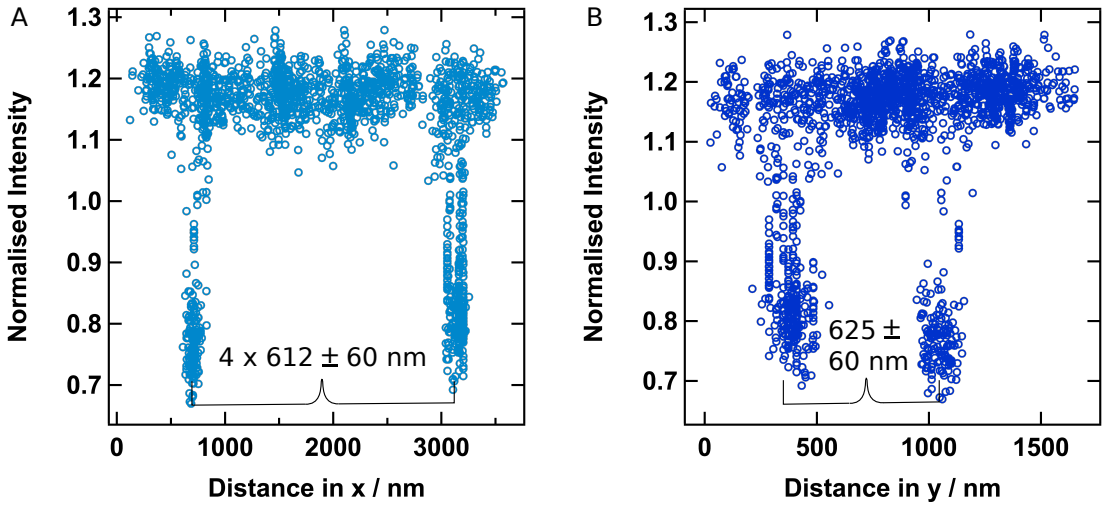

Figure 6.6: **Pillar distances estimated from tracks. (A)** selected track in the x direction shows a spacing of 612 nm or distance 4.08 x 600 nm expected spacing. **(B)** selected track in the y direction shows a spacing of 625 nm or distance 1.04 x 600 nm expected spacing.

The features on the patterned substrates can be seen using iSCAT prior to any image processing. For the 200 nm spacing nanopillar sample (Figure 6.5), the pillars appear as an array of regularly spaced bright spots (panel A). The squared image was tracked as illustrated (panel B), here it can be seen that a single track spans multiple pillars. The phase of the particle in the original background subtracted image changes from bright (panel C) to dark (panel D) as its position in z changes. Extraction of the intensity from these images results in a correlation between intensity and position (panels E & F) and intensity over time (panel G). Here measured contrasts ranged between the bright state with contrast of $\sim$ 20% and the dark state (-20%). In this example, interpolation from gap closing was used to populate intensities for spots with z displacement corresponding with zero contrast. Intensities were extracted from the appropriate frame using the last known co-ordinates of the spot. Because of the finite distance over which gap closing is allowed, only particles that traversed the pillar sufficiently quickly were tracked. This results in artifically step-like transitions in the y direction in plots of y *vs.* time. Correlation of the intensity with both x and y positions allowed visualisation of the topography as in panel H. Analysis of the distances (Figure 6.6) show estimated spacings close to the expected values in both the x and y directions.

This methodology was then applied to the nanowall samples. The spacing for the nanowall samples varied from 200 nm to 600 nm and these two extremes were chosen

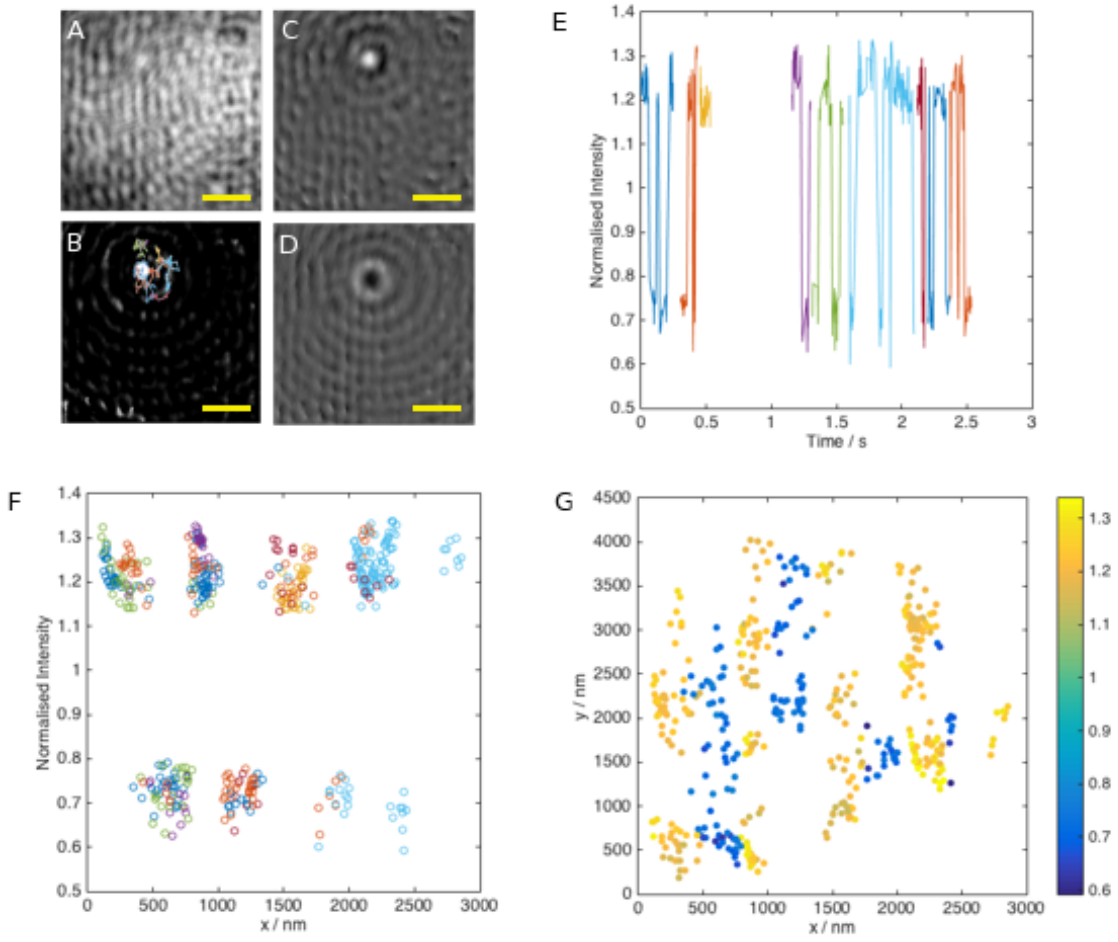

Figure 6.7: **iSCAT imaging of nanowall substrate, 200 nm spacing.** **(A)** Raw iSCAT image of 600 nm spacing nanowall sample, height 200 nm. **(B)** Processed squared image used for tracking with an overlaid track. Normalised image used for intensity extraction showing a bright spot **(C)** corresponding to an intensity of approximate 1.02 and dark spot **(D)** corresponding to an intensity of approximately 0.94. A-D scale bar 3 μm **(E)** Intensity changes as tracks progress over the course of a 3175 frame video (frame time 2 ms). **(F)** Intensity steps from dark to light as the particle traversed in the x direction. For B,E and F, colours correspond to a single track and are consistent across the three panels. It can be seen that a single track switches from light to dark as the particle crosses the nanowalls and changes its position in the z direction. **(G)** Structure of the substrate can be visualised by plotting the x and y coordinates coloured by intensity.

for the same iSCAT analysis as above. The nanowalls of 200 nm spacing showed a less well defined interference pattern pre-processing (Figure 6.7A) as expected for features below the diffraction limit. Interpolation and gap closing were not used for this experiment because the pixel method of extracting intensities (see Section 2.4.2) was used to reduce computing load which, with the estimation of pixel location using

Table 6.1: **Estimations of spacings using intensity data.** Distances between consecutive bright (or dark) states should be approximately twice the expected spacing.

Expected Spacing / nm	Average Distance Between States / nm		
	Dark states	Bright State 1	Bright State 2
200	399 ± 81	428 ± 35	-
400	853 ± 132	881 ± 43	-
600	677 ± 95	1327 ± 258	1323 ± 114

gap closing, did not give accurate pixel intensities for the undetected particles. As sufficient data was given by tracks showing multiple inversions in phase, interpolation seemed to add no further information at this stage. The observed tracks underwent sharp transitions between the dark and light states. Transitions can be seen as a function of time (panel E) and position, as the particles cross the nanowalls in the x direction (panel F). The underlying substrate structure becomes apparent when x and y directions are correlated with intensity (panel G).

The analysis of the 600 nm sample shows a slightly different behaviour (E, F & G). Instead of the two states seen in the other cases, three intensity levels were observed, two bright states and a dark state with very short residence times. This is discussed further below.

The average distance between dark states and between bright states were measured from plots of intensity against x coordinate (in nanometers). This was completed for the 200 and 600 nm data shown and for 400 nm spacing (data not shown). The values are summarised in Table 6.1. A return to the same level of intensity measures one spatial period which is expected to be $2p$ (illustrated in Figure 6.1).

6.4.2 Diffusion on nanowalls is anisotropic

Anisotropic behaviour is evident in the SPT data from nanowall substrates. Figure 6.9 illustrates the MSD analyses for the extremes in height and spacing. Each data set was analysed both isotropically (grey) and anisotropically in the x direction (light blue) and y direction (dark blue). The diffusive behaviour in the y direction is very similar to that within the area containing no pillars and is largely independent of the

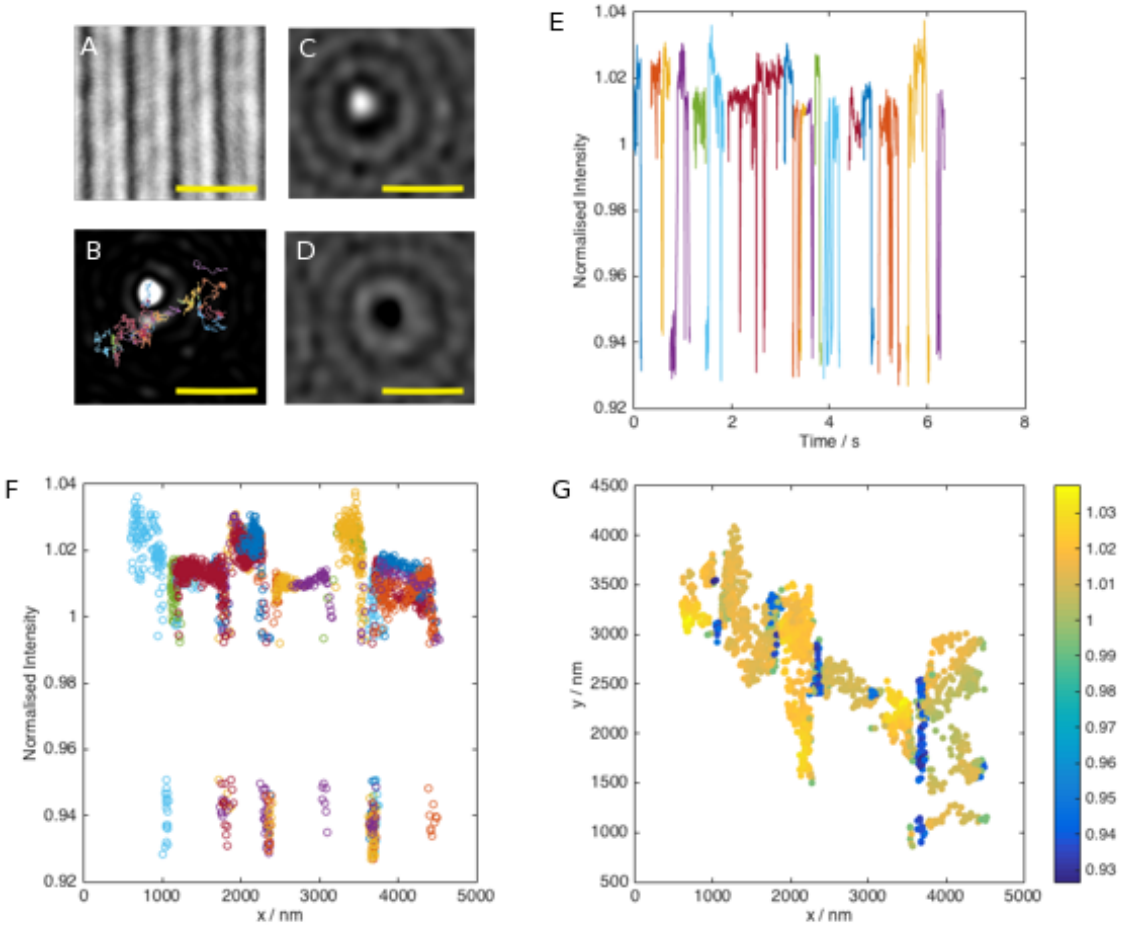

Figure 6.8: **iSCAT imaging of nanowall substrate, 600 nm spacing.** **(A)** Raw iSCAT image of 600 nm spacing nanowall sample, height 200 nm. **(B)** Processed squared image used for tracking with an overlaid track. Normalised image used for intensity extraction showing a bright spot **(C)** corresponding to an intensity of approximate 1.2 and dark spot **(D)** corresponding to an intensity of approximately 0.7. A-D scale bar 2 µm. **(E)** Intensity changes as tracks progress over the course of a 1270 frame video (frame time 2 ms). Each track is reported in a different colour. It can be seen that a single track switches from light to dark as the particle traverses the nanowalls. **(F)** Intensity steps from dark to light as the particle traversed in the x direction at intervals consistent with the spacing of the nanowalls. For B,E and F, colours correspond to a single track and are consistent across the three panels. **(G)** Structure of the substrate can be visualised by plotting the x and y coordinates coloured by intensity.

height and spacing. However, for the 35 nm height (A&B), the reduction in diffusion in the x direction is more pronounced for smaller spacings. This difference is greater still for and higher nanowalls (C&D), however at this 200 nm height, spacing causes little effect. When the spacing is much larger than the height of the nanowalls (B) isotropic and anisotropic analysis methods are effectively equivalent. The isotropic

diffusion is apparently slower than on an area of the sample with no pillars (black, shown in panel C for reference). This is owing to isotropic analysis resulting in a average of the rates in the x direction which is generally slower than in the y direction.

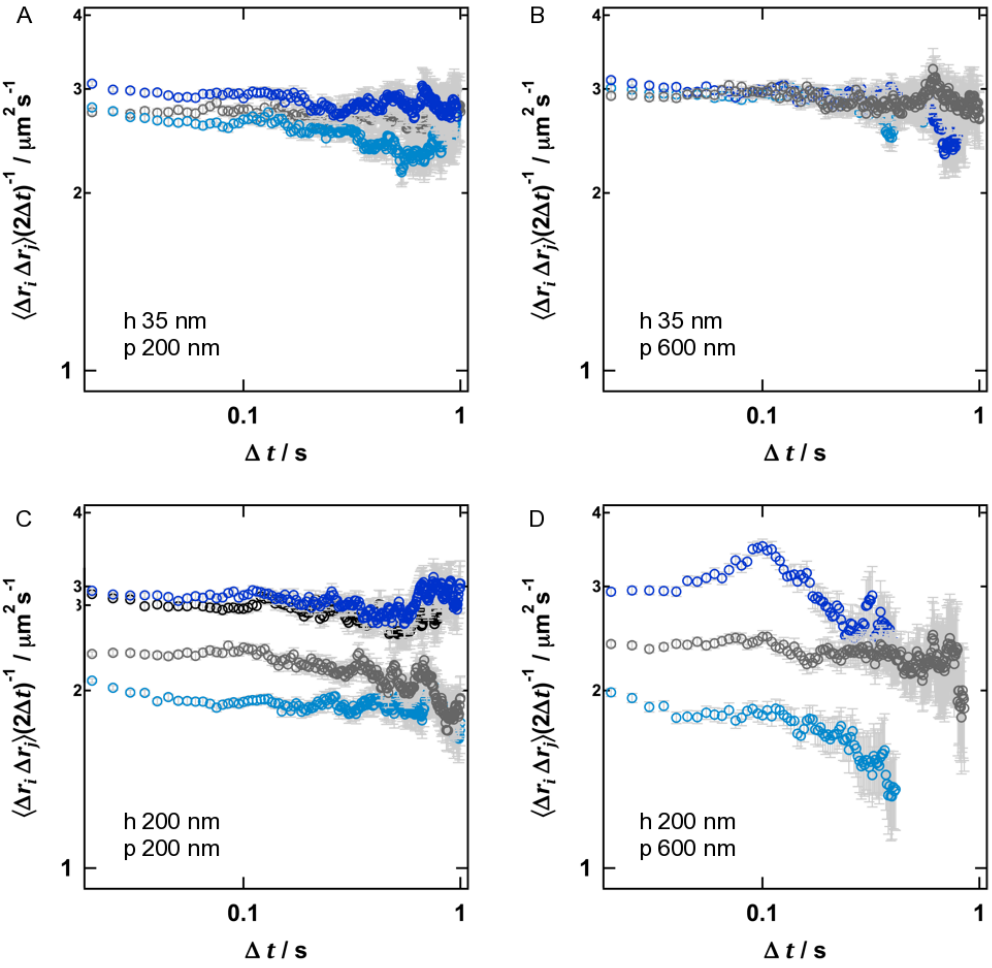

Figure 6.9: **Comparison of isotropic and anisotropic MSD analysis.** Apparent diffusion rates on samples with heights and spacings as indicated in the figure, which correspond to the extremes of the data analysed. Isotropic analysis (grey) results in a diffusion coefficient between the true diffusion coefficient D_{yy} (dark blue) and the slower coefficient seen along the principal axis, D_{xx}, which traverses the nanowalls (light blue). Diffusion on plain glass (black) shown in panel C for reference.

6.4.3 Topography does not cause anomalous behaviour

Anomalous exponents were extracted as previously described in Chapter 4. It can be seen from the examples in Figure 6.9 that the diffusion is largely normal. This was

confirmed for all heights and spacings and is summarised in Figure 6.10 where 96 % of α_{xx} values are indistinguishable from 1.0 (corresponding to free diffusion), within the 95 % confidence interval. Similarly the values for α_{yy} are all within the 95 % confidence interval and are summarised in Table 6.2.

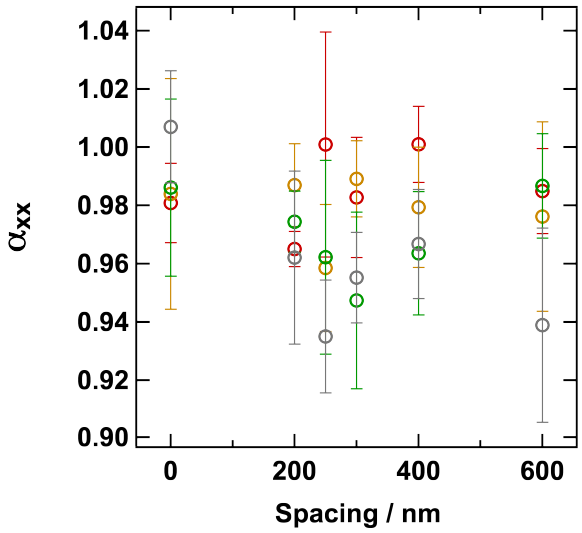

Figure 6.10: **Anomalous exponents show normal diffusion on topographical substrates.** Anisotropic analysis shows normal diffusion in the x direction, where all α values are close to 1 for each spacing and height (α_{xx} nanowalls heights 35 (red), 50 (yellow), 100 (green) and 200 nm (grey)). See Table 6.2 for α_{yy} values.

6.4.4 Using diffusion data to estimate feature height

If the bilayers conform to the rectangular-wave profile of the nanowalls then the theory in Section 6.2 should apply and the height of these features could be estimated from the gradient of a $\sqrt{\frac{D_{yy}}{D_{xx}}}$ *vs.* $\frac{1}{p}$ plot. To assess the other extreme in which the membrane is highly curved, a sine-wave model was simulated.

6.4.4.1 Model validation with simulations

When the rectangular wave simulation was tested with the rectangular wave model (Figure 6.11A), the height extracted is as expected. However, analysing the sine wave simulation (as an approximation of a bilayer with greater curvature) with the rectangular wave model results in output heights much smaller than the expected value. These values are summarised in Table 6.3.

Table 6.2: **Anomalous exponent values extracted from anisotropic analysis along the y axis** Nanowall samples for all heights and spacings.

p / nm	α_{yy} h / nm 35	50	100	200
∞	0.99 ± 0.02	0.95 ± 0.05	0.99 ± 0.01	0.99 ± 0.01
200	0.98 ± 0.04	1.01 ± 0.03	1.00 ± 0.01	0.98 ± 0.02
250	0.98 ± 0.02	0.98 ± 0.01	0.98 ± 0.01	0.99 ± 0.01
300	0.98 ± 0.02	0.99 ± 0.02	0.98 ± 0.02	0.99 ± 0.02
400	0.97 ± 0.01	0.99 ± 0.03	0.98 ± 0.02	1.01 ± 0.02
600	0.98 ± 0.02	1.00 ± 0.02	1.00 ± 0.03	1.00 ± 0.01

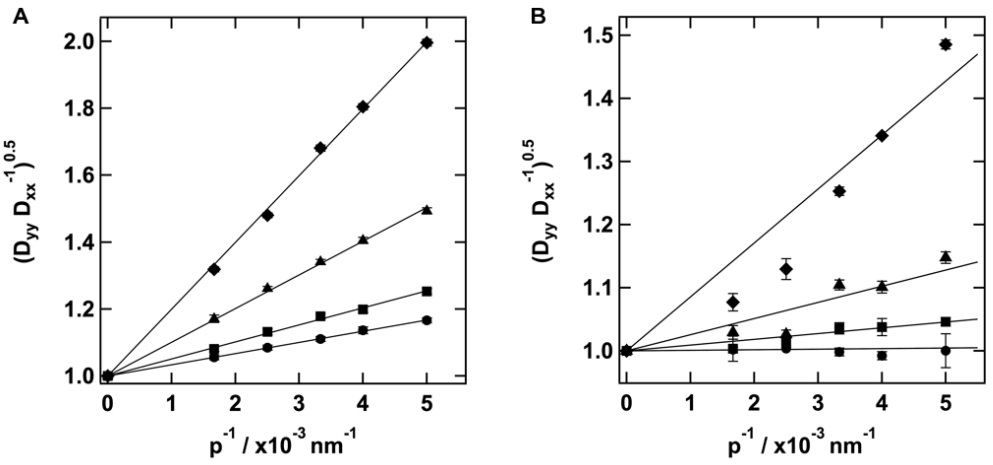

Figure 6.11: **Application of the rectangular wave model to data from simulations on rectangular wave and sine wave surfaces.** $\sqrt{\frac{D_{yy}}{D_{xx}}}$ *vs.* $\frac{1}{p}$ plots from **(A)** the rectangular wave surface and **(B)** the sine wave surface. Straight lines were fit to the data for heights 35 nm (circles), 50 nm (squares), 100 nm (triangles) and 200 nm (diamonds). Output height is found from the gradient of the fit. Lines were fixed through (1,0).

However, with a quadratic term used to estimate path length of the sine wave simulation (see Section 6.2.2), one might expect that the data are fit much better with a parabola (Figure 6.12). The height values extracted from the exponential coefficient are summarised in Table 6.12 and are much more accurate than those

estimated from the linear fits.

Table 6.3: **Heights extracted from application of the rectangular wave model to simulation data.** Linear fits of $\sqrt{\frac{D_{yy}}{D_{xx}}}$ *vs.* $\frac{1}{p}$ plots (Figure 6.11) give a height from the gradient.

	Rectangular Wave	Sine Wave
Expected Height / nm	Gradient (Output Height / nm)	
35	33.60 ± 0.18	0.91 ± 0.53
50	51.07 ± 0.70	9.14 ± 1.08
100	100.86 ± 0.86	25.63 ± 0.35
200	199.61 ± 1.65	85.49 ± 0.35

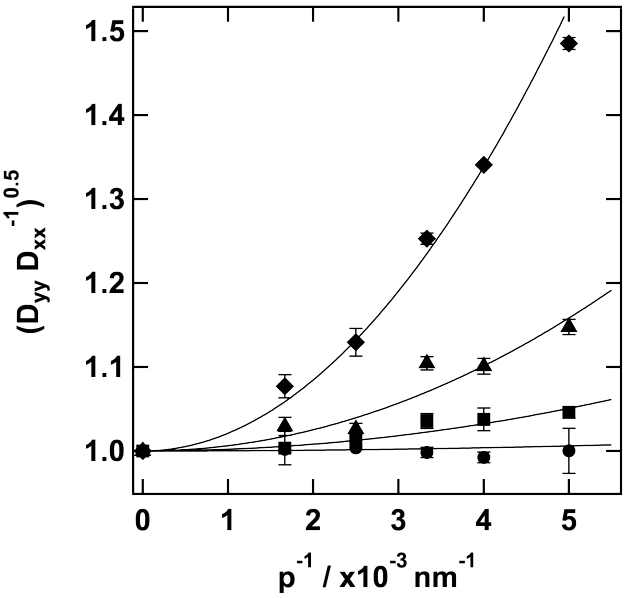

Figure 6.12: **Quadratic fitting to the sine wave simulation data.** $\sqrt{\frac{D_{yy}}{D_{xx}}}$ *vs.* $\frac{1}{p}$ plots from the sine wave surface. Parabolas were fit to the data for heights 35 nm (circles), 50 nm (squares), 100 nm (triangles) and 200 nm (diamonds). Output height is found from the quadratic coefficient. Fits were fixed through (1,0).

Table 6.4: **Heights extracted from parabolic fits to $\sqrt{\frac{D_{yy}}{D_{xx}}}$ *vs.* $\frac{1}{p}$ plots of the sine wave simulation data**

Expected Height / nm	Output Height / nm
35	19 ± 31
50	57 ± 14
100	101 ± 3
200	185 ± 2

6.4.4.2 Application of the rectangular-wave model to the experimental data

$\sqrt{\frac{D_{yy}}{D_{xx}}}$ *vs.* $\frac{1}{p}$ plots are shown in Figure 6.13. Linear fits were fixed through (1,0) and heights were extracted from the gradients (summarised in Table 6.5). It is clear that

the output height from this model is less than the expected height (approximately half). The implications of this are discussed in the following section.

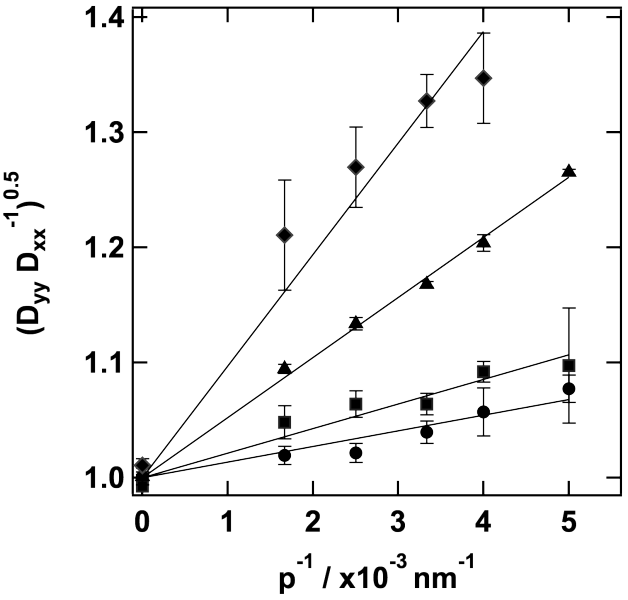

Figure 6.13: **Application of the rectangular wave model to experimental data.** Straight lines were fit to the data for heights 35 nm (circles), 50 nm (squares), 100 nm (triangles) and 200 nm (diamonds). Output height is found from the gradient of the fit. Lines were fixed through (1,0).

Table 6.5: **Heights extracted from the linear fits of $\sqrt{\frac{D_{yy}}{D_{xx}}}$ *vs.* $\frac{1}{p}$ plots of the experimental data**

Expected Height / nm	Gradient (Output Height / nm)
35	13.58 ± 0.98
50	21.37 ± 1.29
100	52.21 ± 0.69
200	96.96 ± 5.85

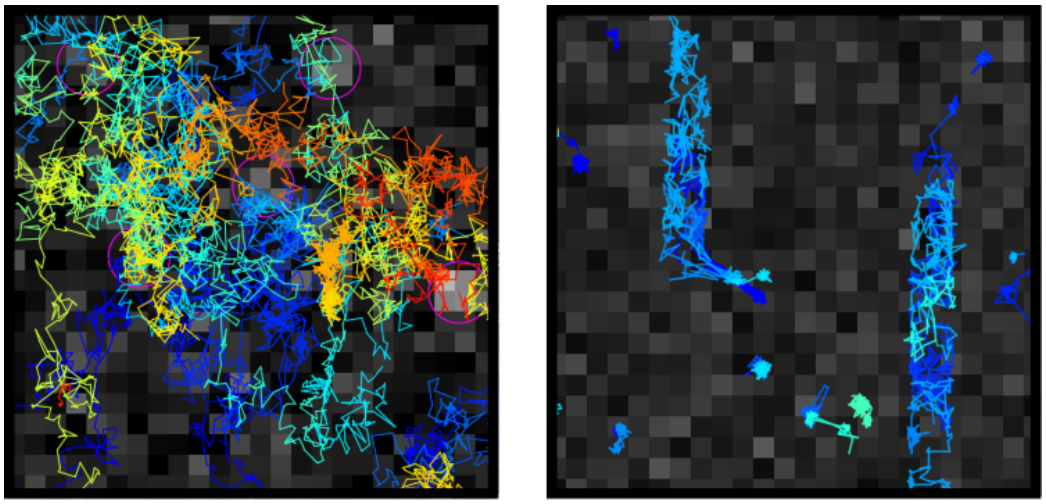

Figure 6.14: **Confinement of tracks after fibronectin printing. (A)** Tracks before printing have similar displacements in both x and y directions. **(B)** After fibronectin printing, displacements appear more confined in the x direction. Both images from 200 nm height, 600 nm spacing nanowall sample. Image size 10 × 10 microns. Individual tracks are shown in different colours.

6.4.4.3 Immobile obstacles are required to induce anomalous behaviour

In a control experiment, fibronectin was printed onto the ridges of the 200 nm height substrate prior to SLB incubation. This resulted in a switch from topographical to topological surfaces and therefore particles exhibited reduced diffusion in the x direction. This is evident from the tracks illustrated in Figure 6.14 and is mirrored in the $\langle \Delta r_i \Delta r_j \rangle (2D_{yy})^{-1}$ *vs.* Δt plots (Figure 6.15). Anomalous behaviour becomes evident, but is largely independent of the spacing (Figure 6.15A). For comparison to the equivalent topographical substrate, Figure 6.15B shows anisotropic analysis of the particles tracked over the 300 nm spacing both with and without fibronectin printing. The behaviour is much more anomalous once the particles are confined with fibronectin.

This switch to anomalous behaviour is also reflected in the α values as shown in Figure 6.16. Here the same data for the original samples (α_{xx} grey scale, refer to Figure 6.10) is shown for reference, as well as the data from the printed sample for both α_{xx} (light blue) and α_{yy} (dark blue). The values of α_{xx} for the printed samples is on average 0.50 ± 0.04 and α_{yy} 0.78 ± 0.02.

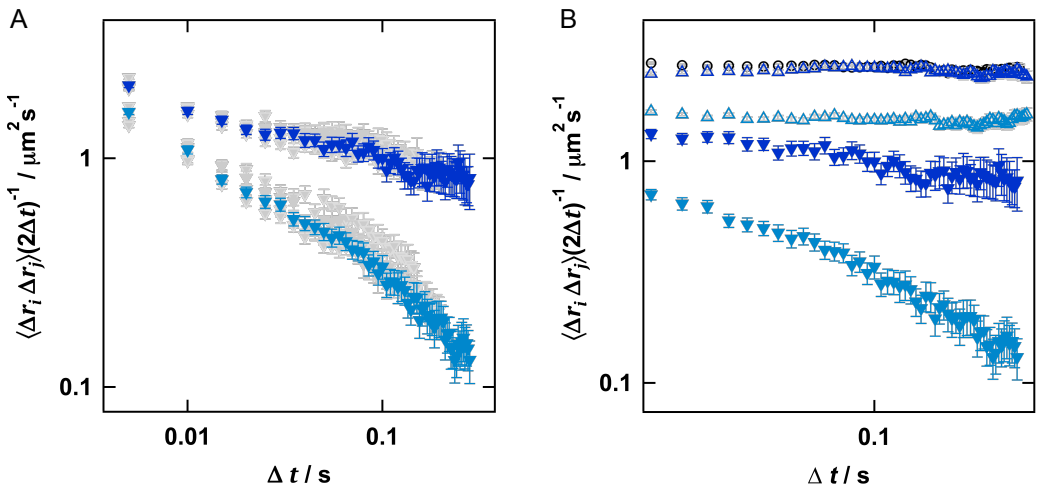

Figure 6.15: **Diffusive behaviour on 200 nm height nanowalls printed with fibronectin and comparison with topographical substrate.** $\langle \Delta r_i \Delta r_j \rangle (2D_{yy})^{-1}$ *vs.* Δt plots showing **(A)** diffusion on printed nanowalls is largely independent of spacing (200, 250, 400 and 600 nm spacing in grey, 300 nm highlighted D_{xx} light blue and D_{yy} dark blue), and **(B)** comparison of diffusive behaviour on equivalent topographical and topological substrates (closed symbols as in (A) with equivalent anisotropic analysis on sample without fibronectin (open symbols, D_{xx} light blue and D_{yy} dark blue) and isotropic analysis on plain glass (black).

6.5 Discussion

This study aimed to address if topography could cause apparently anomalous diffusion in single particle fluorescence tracking experiments. To achieve this, a number SLBs were produced on substrates of known topography. Fluorescence tracking was complicated by difficulty in visualising the patterned areas using white light owing to the small size and low scattering of the etched labels adjacent to each area. Using iSCAT however, nano patterning of glass substrates can be visualised using iSCAT prior to any background subtraction. This demonstrates another way in which the combination of fluorescence and iSCAT imaging proves to be a powerful technique. iSCAT however, could not be used on its own to complete the tracking experiments required for this study. The underlying structure made background subtraction difficult. To mitigate this, 40 nm gold particle labels were required which is not ideal for imaging on the shallow height samples. Contrast of the particles changes as a function of z position above the coverslip and despite squaring of the images, iSCAT contrast still tended to zero at certain z displacements on the nanowall and nanopillar samples. The particles were therefore not detected by TrackMate, resulting in short tracks insufficiently long to allow MSD analysis over long timescales.

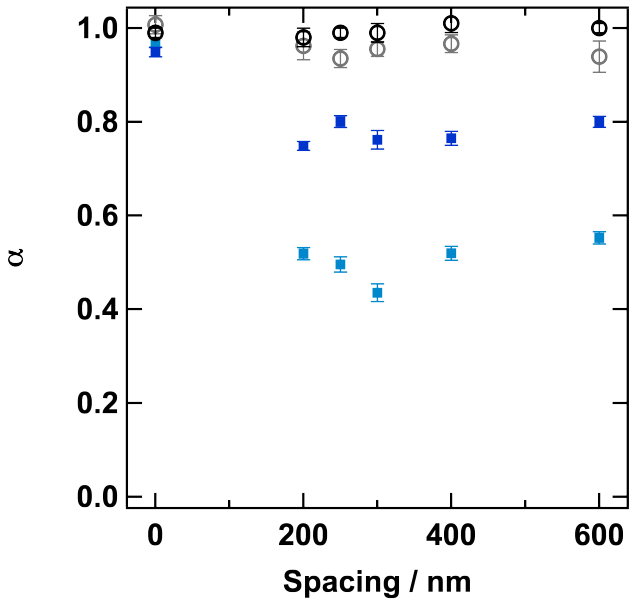

Figure 6.16: **Anomalous exponents distinguish between topography and topology.** Reduction in α values in both x and y directions after printing of topographical surfaces (200 nm height) with fibronectin. α_{xx} before printing (grey, open symbols) and after printing (light blue, closed symbols), α_{yy} before printing (black, open symbols) and after printing (dark blue, closed symbols).

The change in phase could however be used to demonstrate that the bilayers were contiguous and followed the contours of the substrates. Single particles were observed traversing distances consistent with multiple features. Additionally, the intensity of a spot was used to demonstrate that the signal phase changed at intervals consistent with the expected spacing between features. Interpolation was not used, as the extra processing was deemed unnecessary to interpret the data. Estimation of the location using the co-ordinates of the last detected spot is sufficiently accurate for short gap closing but is not a good estimation of position after several frames. Thus, extraction of the intensity from this pixel does not give reliable contrast values. Optimisation of the tracking procedure to account for gap closing, or use of the more computationally demanding fitting methods (average or gaussian, see Section 2.4.2) for intensity extraction, would be necessary to build a complete picture of the topography using contrast data.

In the 600 nm spacing nanowall sample (Figure 6.8) the distance between the dark states (Table 6.1) is close to the value of the spacing, not $2p$ as expected. This is consistent with this distance corresponding to a height up the side of the nanowalls (not the top or bottom as for the other examples) and could be attributed to the

focussing of the particle. The path difference between the detected object and the reflecting surface differs depending on the plane of the sample which is focussed upon, thus resulting in a different phase. If the focal plane chosen for the 600 nm sample was different that the other substrates, one might expect a different phase behaviour of the signal. Focus locking via a feedback mechanism could be introduced to ensure all samples are imaged from the same focal plane. Despite this, the data indicates that bilayers are contiguous and topographical.

Isotropic diffusion analysis of anisotropic SPT data results in an apparently slower diffusion. In such cases, the reported behaviour is a combination of the diffusivity along each axis. In flat space (y direction in this work) the diffusion is faster than that reported from the isotropic analysis, while along the principal axis (x) it is slower. Although, some roughness was introduced by the e-beam etching process, in all cases the diffusion was largely normal. This is as expected owing to averaging over many tracks with different positions on the topographical surface and many time windows. For topological surfaces however, all particles are hindered at a particular length or time scale resulting in deviation from the normal MSD. Similar work by Werner *et.al* [154] yielded complementary results showing anisotropic diffusion in bilayers conforming to a topographical substrate. However, this work contained no analysis for anomalous diffusion, nor mentioned the impact of this on interpretation of SPT data.

Fibronectin printing illustrates that topology is necessary for this model to exhibit anomalous behaviour. Here, bilayers cannot form in areas printed with fibronectin, therefore producing patches comparable to immobile obstacles. Printing on the 200 nm height nanowall sample resulted in a change of α_{xx} from 0.97 to 0.50 and α_{yy} from 0.99 to 0.78. As α is not reduced to zero, the word *confinement* is used carefully. It was argued in Chapter 4 that the midpoint of the sigmoid fit of an α *vs.* EAF plot, corresponding to $\alpha = 0.5$, gives some indication of the percolation threshold and the point at which bilayer patches (compartments) are created. This is consistent with α_{xx} reducing to 0.5 here as the fibronectin results in a finite length scale in the x direction. The length scale, dictated by the spacing, is likely to correspond with a time scale on the order of tens of milliseconds and should be within the range of data recorded. However, the behaviour appears anomalous on all timescales recorded and no crossover is seen, so further work would be needed to ensure that sufficient time scales were sampled. It is interesting that a reduction in α was also evident in the y direction. Although the particles should not be confined along this axis,

the reduction in α suggests otherwise. It is possible that this was caused by miss-printing of the fibronectin in which immobile obstacles were created between the walls. It would be best to visualise this whilst simultaneously recording SPT data using dual colour imaging and fluorescently labelled fibronectin. Alternatively other surface characterisation techniques such as AFM could be used.

The difference in diffusivity along each axis is dictated by the the topography of the surface and as such, it can be used to estimate feature height. The simulations not only showed that diffusion is not anomalous, but allowed validation of the respective methods to make this estimation. In both cases the height could be accurately extracted from the gradient of a $\sqrt{\frac{D_{yy}}{D_{xx}}}$ *vs.* p^{-1} plot. The estimates were within 5 % for the rectangular wave and 15 % for the sine wave (except for the smallest height). This is a reasonable error as the sine wave simulation was fit using only one term of the Taylor series.

Analysis of the sine wave simulation using the rectangular wave model was used to assess the effect of treating a highly curved membrane as a rectangular wave. In this case, the heights extracted were much lower than the input height. It was expected that in the experimental model, the bilayer would conform to the rectangular-wave substrate with some additional curvature at the corners. Analysis using the rectangular-wave model resulted in heights lower than expected, much like in the simulation case. It is therefore speculated that the bilayer system loosely follows the structure of the surface and exhibits a topography somewhere between a rectangular and sine wave.

However, it is clear from Figure 6.13 that it is not appropriate to fit the experimental data with the parabolic sine wave model. A different interpretation of the phase changes in the iSCAT data, particularly the three contrast levels seen in Figure 6.8, is that for a fixed expected height, the output height changes as pitch changes. Complete inversion of the phase in iSCAT is $\frac{\lambda}{4n}$ where λ is the incident wave length (639 nm) and n is the refractive index of the surrounding medium (~ 1.33). This corresponds to a z displacement of 120 nm for this experiment. As one phase inversion was seen in the iSCAT data from the 200 nm spacing, it is reasoned that the bilayer height is likely to be $\sim$ 120 nm, which is consistent with the output of the rectangular wave model. However, it is possible that the two inversions seen for the 600 nm spacing was not a focussing error but a result of the particle traversing between 120 and 240 nm. In this case it is possible that the large spacing allowed the bilayer to better conform to the expected topography. It can be seen that the data

does begin to deviate from the straight line fit consistent with an apparent height of 97 nm.

Anisotropic surfaces were chosen for this study, but further work could extend this to substrates exhibiting more complex topographies. For example, SPT could easily be completed on the nanopillar samples. Anomalous diffusion has been observed in nanostructure [139, 155] and nano-patterned [156, 157, 158] systems before. However, it is of great importance that it is noted here that these structures induced anomalous behaviour because they act as obstacles. The bilayers were not allowed to coat the structure as was demonstrated in the work presented here and is effectively equivalent to the fibronectin control. Such obstacles are expected to cause anomalous behaviour and these systems do not mimic the texture of biological membranes. In the studies which formed a contiguous bilayer over nano-patterning [159, 160], it was noted that the structure acted as a barrier, reminiscent of cytoskeletal pinning, also known to cause anomalous behaviour.

An obvious extension to this work would be to analyse the effect of these substrates on cells. Topographical substrates are important for sensor applications [161] and cells have previously been shown to conform to certain shapes [162]. In this study, Hanson *et al.* indicated that the ratio of feature width to spacing was the most important metric determining cell surface conformation with the substrate. The present work had a fixed ratio of 1 which is much larger than in Hanson's work. Nanobars have also been used to show curvature dependent clustering of proteins in cells [163]. These substrate a more similar to the nanowalls presented here, yet the spacing and height were still much greater (by almost order of magnitude). Therefore care must be taken to determine if the cell membrane has conformed to the substrate if this study is to be repeated in cells.

6.6 Conclusions

This preliminary data has shown that topography does not cause anomalous diffusion. Thus, it is argued that the anomalous behaviour seen in cells cannot be a result of topography but is more likely to be caused by immobile obstacles *i.e.* topography. The α values extracted from the present study, being so close to 1.0, support this. In addition, immobile obstacles, produced by printed fibronectin, were required to induce anomalous behaviour in the topographical system. Only in this case were the α values reduced to coincide with the range reported in cells [48, 135, 136, 137]. It was also shown in this study that, with proper analysis, the reduction in the diffusion

coefficient can be used to estimate feature size. It may be possible to use single particle tracking data from cells to assess cell topography, or conversely, measured features could be used to estimate the resultant reduction in diffusion coefficient.

Chapter 7

Conclusions and Outlook

Anomalous diffusion is a phenomenon widely reported in biological systems, which greatly effects the movement of molecules within the bilayer. These molecules include lipids themselves, which can be confined to raft like domains, and receptor proteins essential for cell signalling. Anomalous diffusion therefore plays an important role in the normal functioning of biological membranes. Despite this, there are still some fundamental questions surrounding the causes, extent and control of this phenomenon. The aim of this work was to address two fundamental questions regarding anomalous diffusion; a) can Saxton's call for *'a positive control for anomalous sub-diffusion'* be answered? and b) can topography cause anomalous behaviour?

To achieve this, quantitative analysis of the diffusion in lipid bilayers at biologically relevant timescales is essential. High speed single particle tracking of gold nanoparticle-conjugated lipids using iSCAT microscopy was employed. The iSCAT method allows for theoretically indefinite imaging at microsecond time resolution. In practice, the technique is limited by uneven, varying background and unwieldy data volumes. The third chapter of this thesis suggests some ways to manage these limitations. Attaining sufficiently high signal to noise ratios is important for ensuring good localisation. This was achieved by altering the magnification, evenly illuminating with high intensity light and optimising the label size. Computational routines were also established to manage the data which increased the efficiency of the analysis process.

Contrast can be improved by maximising the scattering cross-section or excluding stray reflected light. Of particular promise is the ten-fold enhancement of contrast using the Nanolane Surf substrates. Although the cost is currently a limitation, these substrates have potential to allow the detection of particles half the size of the current limit. Careful procedures for cleaning and handling would need to be established to ensure that the substrate remains effective. This requires a more sophisticated SLB

chamber, such as PDMS gaskets, rather than vacuum grease. Such polymer or glass flow cells are common and easy to make, but are not compatible with iSCAT. The high intensity of light transmitted through the sample can reflect from the top surface of a flow cell leading to obscuring reflections. Perhaps a more successful design would be an open polymer gasket.

Despite these optimisations, there are still some limitations to our iSCAT instrument. Namely, the localisation precision and noise levels are not as good as those reported for other instruments. Stability of the instrument is the factor most easily addressed and likely to have the most impact on the noise. To achieve greater stability, the feedback system should be implemented for all experiments. A new platform could be designed and produced which fixes and encloses the coverslip to reduce transmission of vibrations. Full concealment of the optics with a positive pressure system would reduce stray light as well as aberrations caused by dust particles. This would result in a more even background, easily subtracted in the analysis phase.

The iSCAT and fluorescence methodologies were utilised for the main body of this work in which anomalous diffusion was studied in three model systems. The aim of the first was to contribute to answering the call by Saxton, in which eight criteria for a 'positive' control for anomalous diffusion were outlined. Saxton argued that questions were still unanswered about the mechanisms underlying anomalous diffusion because each proposed mechanism was determined by a different method or experimental model. Thus, control was necessary to cross-calibrate these studies. The PEG-SLB model fully satisfied six of the eight criteria. Criterium (7), 'Tracers detectable by both NMR and fluorescence', has not been assigned as satisfied as no NMR experimentation was completed in this work. It was argued in the conclusion of Chapter 4 that only a sub-case of criterion (8) was satisfied as no second crossover, to return to normal diffusion, was seen. It would be possible using iSCAT to image for a sufficiently long time to definitively know if diffusion returned to normal or did indeed continue to be anomalous.

It was demonstrated using urea, that simple buffer additives can induce complex anomalous behaviour. The diffusion of lipids was affected in both a time and concentration dependant manner. Again this resulted in a partial fulfilment of Saxton's criteria. However, without proper characterisation of the surface, the mechanism of action of urea is so far unknown. An obvious extension to this work on these models exhibiting anomalous behaviour, would be to track other molecules of interest such as membrane proteins to determine their behaviour in both the PEG and urea systems. It has been shown that cells used subdiffusion to regulate the interactions of molecules

[64, 164, 165, 166, 167], thus, it may also be possible to use these systems to control the rates of membrane associated reactions or to specifically conjugate proteins to the membrane as a means to control their action.

It has been demonstrated in a systematic way that topography does not cause apparent anomalous behaviour and that topology is necessary for this. Glass substrates were custom made to present a rectangular wave profile in the x direction and flat profile in the y direction. Height and spacing were altered to provide a number of aspect ratios ranging from 1:1 to 120:7. Over all of these surfaces, the diffusion was normal, which was also confirmed using simulations. This result indicates that topography does not result in apparent anomalous diffusion in single molecule microscopy projections of 3D surfaces. Fibronectin printing showed that topography was necessary to result in anomalous behaviour on the 3D substrates. This suggests that the 3D structure of cells does not contribute to the anomalous diffusion detected *in vivo*. It is likely that this, as described in the opening pages, is at least partly caused by cytoskeletal pinning.

To further this work, it would be necessary to prove this hypothesis in cells. Current work being undertaken by our collaborators in Glasgow aims to address this. Anomalous diffusion has been detected in the cells incubated on smooth coverslips and dyed with a fluorescent membrane label. In planned experiments this will be observed on on the topographical substrates. It is hypothesised that on depolymerisation of the cytoskeleton, diffusion will become normal despite the 3D structure of the membrane.

The 3D tracking potential of iSCAT is an attractive avenue of further investigation into diffusion on 3D surfaces. To accomplish this, a number of instrument and analysis routine optimisations would need to be completed. In particular, focal plane locking would need to be implemented such that it can be used to calibrate any change in particle height. Calibrations have previously been undertaken using gold nanoparticles deposited on silicon oxide layers of known thickness [168], and a similar method would need to be implemented to achieve this on the particular instrument to be used. To optimise the processing, tracking algorithms must detect the particle whilst its z displacement changes the phase of the particle, ideally giving an accurate estimation of the position even with zero contrast.

Simulations have played a key role in assessing data and validating models. Simple Monte Carlo simulations were used to produce tracks and image stacks which could be subjected to the same analysis routines as experimental data. These simulations elucidated the importance of signal to noise ratio in causing apparently anomalous behaviour at short timescales. This prevented false assignment of anomalous diffusion

to tracking artefacts caused by poor localisation. In the study of the PEG-SLB model, simulations aided understanding of the experimental data by allowing comparison to a system of known topology. Of particular interest was the result that different obstacle sizes were easily distinguishable by de-dimensionalisation of the simulations, while the experimental data suggested a fixed length scale. The square lattice simulations however, were not representative of the experimental system. In further work it would be possible to simulate random obstacles or defects which bear more resemblance to the structures seen using AFM.

In the chapter separating topology from topography as a potential cause of anomalous diffusion, simulations were essential in validating the height estimation models. Random walks were undertaken with path lengths resembling either a rectangular or sine wave. These were then returned to contravariant space to simulate the 'projection' of the 3D surface observed using single molecule microscopy. The ratio of the path lengths in covariant and contravariant space were used to produce models in which the diffusion coefficients in the x and y directions could be used to estimate the feature height.

Overall, the iSCAT methods developed have proven to be powerful and complementary to SM-TIRF methods for studying diffusive behaviour. The use of both techniques allows high temporal resolution which can span several orders of magnitude in time and has the potential to be effective in three dimensions. The work presented has provided a method by which the extent of anomalous behaviour can be carefully chosen. This has helped to elucidate aspects of the anomalous diffusion phenomenon which are of great importance to understanding the complex cell membrane, perhaps allowing for better artificial mimics of this structure in the future.

Appendix A

Publications

Coker, H. L. E., Cheetham, M. R., Kattnig, D. R., Wang, Y. J., Garcia-Manyes, S., & Wallace, M. I. (2017). Controlling Anomalous Diffusion in Lipid Membranes. ArXiv Pre-Press. Retrieved from http://arxiv.org/abs/1709.04698. Submitted to ACS Nano.

Weatherill, E., **Coker, H. L. E.**, Cheetham, M. R., & Wallace, M. I. (2018). Urea-Mediated Anomalous Diffusion in Supported Lipid Bilayers. ArXiv Pre-Press. Retrieved from https://arxiv.org/abs/1805.05620. Interface Focus. Under review.

Cheetham, M. R., **Coker, H. L. E.**, Blosser, M. C., Greer, A., Reynolds, P., Gadegaard, N., & Wallace, M. I. (2018). Topology *vs.* Topography: What Really Causes Anomalous Diffusion? In preparation.

Appendix B

Code

B.1 Python

B.1.1 GUI free TrackMate

```
# # # # # # # # # # # # # # # # # # # # # # # # # # # # # # # # # # # # # # #
# HC 23 OCT 17
#
# TrackMate without the GUI so that large files/many frames can be...
# processed quickly.
# Based on http://imagej.net/Scripting_TrackMate
# Spits out data table and exports *TRACKS* into XML
# Lines see 181-183 can be added in to export *ALL FEATURES* from...
# table to XML
#
# AS WITH TRACKMATE THIS HAS MEMORY LEAK so you MUST close and...
# restart FIJI every time.
# If it complains that it's out of memory, make sure you have...
# allocated as much as possible and just restart FIJI and try again.
# It's usally just a memory leak issue.
#
# Sections containing user settings which MUST be checked prior to...
# running are ...
#
# -------------------
# in boxes like this
# -------------------
#
# # # # # # # # # # # # # # # # # # # # # # # # # # # # # # # # # # # # # # #

# Import Packages #

from ij import IJ, ImagePlus, ImageStack
import fiji.plugin.trackmate.Settings as Settings
```

```
import fiji.plugin.trackmate.Model as Model
import fiji.plugin.trackmate.SelectionModel as SelectionModel
import fiji.plugin.trackmate.TrackMate as TrackMate
import fiji.plugin.trackmate.Logger as Logger
import fiji.plugin.trackmate.detection.DetectorKeys as DetectorKeys
import fiji.plugin.trackmate.detection.LogDetectorFactory as
    LogDetectorFactory
import fiji.plugin.trackmate.tracking.sparselap.SparseLAPTrackerFactory as
    SparseLAPTrackerFactory
import fiji.plugin.trackmate.tracking.LAPUtils as LAPUtils
import fiji.plugin.trackmate.visualization.hyperstack.HyperStackDisplayer
    as HyperStackDisplayer
import fiji.plugin.trackmate.features.FeatureFilter as FeatureFilter
import fiji.plugin.trackmate.features.FeatureAnalyzer as FeatureAnalyzer
import
    fiji.plugin.trackmate.features.spot.SpotContrastAndSNRAnalyzerFactory
    as SpotContrastAndSNRAnalyzerFactory
import fiji.plugin.trackmate.action.ExportStatsToIJAction as
    ExportStatsToIJAction
import fiji.plugin.trackmate.io.TmXmlReader as TmXmlReader
import fiji.plugin.trackmate.action.ExportTracksToXML as ExportTracksToXML
import fiji.plugin.trackmate.io.TmXmlWriter as TmXmlWriter
import fiji.plugin.trackmate.features.ModelFeatureUpdater as
    ModelFeatureUpdater
import fiji.plugin.trackmate.features.SpotFeatureCalculator as
    SpotFeatureCalculator
import fiji.plugin.trackmate.features.spot.SpotContrastAndSNRAnalyzer as
    SpotContrastAndSNRAnalyzer
import fiji.plugin.trackmate.features.spot.SpotIntensityAnalyzerFactory as
    SpotIntensityAnalyzerFactory
import fiji.plugin.trackmate.features.track.TrackSpeedStatisticsAnalyzer
    as TrackSpeedStatisticsAnalyzer
import fiji.plugin.trackmate.util.TMUtils as TMUtils
from ij import IJ, WindowManager
from java.io import File
import fiji.plugin.trackmate.action.AbstractTMAction
import java.util.HashMap
import os
import fiji.plugin.trackmate.features.track.TrackDurationAnalyzer as
    TrackDurationAnalyzer

# ------------------------
# Import Specific Image
# ------------------------

#imp = IJ.openImage('http://fiji.sc/samples/FakeTracks.tif')
#imp.show()
```

```
# OR...

# Get Current Image #

imp = WindowManager.getCurrentImage()
dims = imp.getDimensions();
imp.setDimensions( dims[ 2 ], dims[ 4 ], dims[ 3 ] );
shortTitle = WindowManager.getCurrentImage().getShortTitle()
name = str(shortTitle)

# -----------------------
# Choose Save Location
# -----------------------

filename = '/Users/miwgroup/Desktop/'+ name +'.xml'

# Instantiate Model Object #

model = Model()

# Set Logger #

model.setLogger(Logger.IJ_LOGGER)

# Prepare Settings Object #

settings = Settings()
settings.setFrom(imp)

# --------------------
# Configure Detector
# --------------------

settings.detectorFactory = LogDetectorFactory()
settings.detectorSettings = {
    DetectorKeys.KEY_DO_SUBPIXEL_LOCALIZATION : True,
    DetectorKeys.KEY_RADIUS : 3.5, #set spot RADIUS (must be a double),
        note: in GUI this is diameter
    DetectorKeys.KEY_TARGET_CHANNEL : 1, # must be integer
    DetectorKeys.KEY_THRESHOLD : 0.015, # must be double so include
        decimal place
    DetectorKeys.KEY_DO_MEDIAN_FILTERING : False,
}

# --------------------
# Configure Tracker
```

```
# --------------------
settings.trackerFactory = SparseLAPTrackerFactory()
settings.trackerSettings = LAPUtils.getDefaultLAPSettingsMap()
settings.trackerSettings['LINKING_MAX_DISTANCE'] = 3. # must be double so
    include decimal place
settings.trackerSettings['GAP_CLOSING_MAX_DISTANCE']= 0. # must be double
    so include decimal place
settings.trackerSettings['MAX_FRAME_GAP']= 0 # must be integer

# Add the analyzers for some SPOT features.

# You need to configure TrackMate with analyzers that will generate the
    data you need.
# Here we just add two analyzers for spot, one that computes generic ...
# pixel intensity statistics (mean, max, etc...) and one that computes an
    estimate of each spot's SNR.
# The trick here is that the second one requires the first one to be in
    place.
# Be aware of this kind of gotchas, and read the docs.

settings.addSpotAnalyzerFactory(SpotIntensityAnalyzerFactory())
settings.addSpotAnalyzerFactory(SpotContrastAndSNRAnalyzerFactory())

# Add an analyzer for some TRACK features
# e.g. track mean speed and TrackDuration which includes
    "TRACK_DURATION";"TRACK_START"; "TRACK_STOP";"TRACK_DISPLACEMENT";
# if you want to filter by other things you need to find the correct
    analyzer and add this first.

settings.addTrackAnalyzer(TrackSpeedStatisticsAnalyzer())
settings.addTrackAnalyzer(TrackDurationAnalyzer())

# ----------------------
# Initial Spot Quality
# ----------------------

# settings.initialSpotFilterValue = 1

print(str(settings))

# ------------------------------------------------
# Filter By Track Duration or Track Displacement
# ------------------------------------------------

# Configure track filters - Track displacement must be above 10 pixels =
    FeatureFilter('TRACK_DISPLACEMENT', 10, True)
```

```
# Track duration above 2000 frames = FeatureFilter('TRACK_DURATION', 2000,
    True)

filter2 = FeatureFilter('TRACK_DURATION', 10000, True)
#filter2 = FeatureFilter('TRACK_DISPLACEMENT', 10, True)
settings.addTrackFilter(filter2)

# Instantiate TrackMate #

trackmate = TrackMate(model, settings)

# Execute All #

import sys

ok = trackmate.checkInput()
if not ok:
    sys.exit(str(trackmate.getErrorMessage()))

ok = trackmate.process()
if not ok:
    sys.exit(str(trackmate.getErrorMessage()))

# Display Results #

model.getLogger().log('Found ' + str(model.getTrackModel().nTracks(True))
    + ' tracks.')

selectionModel = SelectionModel(model)
displayer = HyperStackDisplayer(model, selectionModel, imp)
displayer.render()
displayer.refresh()

# Add Features to Model # (stores edge and track features)

fm = model.getFeatureModel()

for id in model.getTrackModel().trackIDs(True):

    # Fetch the track feature from the feature model.
    v = fm.getTrackFeature(id, 'TRACK_MEAN_SPEED')
    model.getLogger().log('')
    model.getLogger().log('Track ' + str(id) + ': mean velocity = ' +
        str(v) + ' ' + model.getSpaceUnits() + '/' + model.getTimeUnits())

    track = model.getTrackModel().trackSpots(id)
    for spot in track:
```

```
        sid = spot.ID()
        # Fetch spot features directly from spot.
        x=spot.getFeature('POSITION_X')
        y=spot.getFeature('POSITION_Y')
        t=spot.getFeature('FRAME')
        q=spot.getFeature('QUALITY')
        snr=spot.getFeature('SNR')
        mean=spot.getFeature('MEAN_INTENSITY')
        model.getLogger().log('\tspot ID = ' + str(sid) + ': x='+str(x)+',
            y='+str(y)+', t='+str(t)+', q='+str(q) + ', snr='+str(snr) + ',
            mean = ' + str(mean))

# ----------------------
# Export TRACKS to XML
# ----------------------

ExportTracksToXML.export(model, settings, File(filename))

# ---------------------------
# Export ALL FEATURES to XML
# ---------------------------

#outfile = TmXmlWriter(File('/Users/miwgroup/Desktop/Testing123.xml'))
#outfile.appendModel(model)
#outfile.writeToFile()
```

B.1.2 Cine-TIFF conversion and averaging

Written with M.I. Wallace.

```
import os #for making directories
from glob import glob

#.cine to your file type
paths = glob('*.cine')
#print paths

for i in paths:
 os.system("python imageaverager.py --mean --grouped --filterwindow 10
     --normalise " + i)
```

```
# Setup Instructions
# -----
# pip install bottleneck
# pip install scikit-image
# pip install pims
```

```
# pip install jpype1
# pip install tifffile
# pip install tqdm

# Example Useage
# -----
# python imageaverager.py --median --running --filterwindow 50
    2PEG5us10short.cine
# python imageaverager.py --median --grouped --filterwindow 50 'test/*.tif'
# python imageaverager.py --median --grouped --filterwindow 50
    percsim_f_0.1.tif
# python imageaverager.py --quicksave 2PEG5us10.cine
# python imageaverager.py --normalise --quicksave 2PEG5us10.cine
# python imageaverager.py --normalise --quicksave
    /Volumes/Elements/HC/2PEG5us10.cine

import pims
from matplotlib import pyplot as plt # If you want to add plotting.
import argparse
import bottleneck as bn
from skimage import io
import numpy as np
import time
from tqdm import tqdm #adds a taskbar to any loop, just wrap any iterable
    with tqdm(iterable) e.g. for i in tqdm(range(10000)):
from matplotlib import pyplot as plt # for plotting

#from joblib import Parallel, delayed #easy parallel processing
# Under Windows, it is important to protect the main loop of code to avoid
    recursive spawning of subprocesses when using joblib.
# No code should run outside of the "if __name__ == '__main__'" blocks,
    only imports and definitions.


# Get some variables from command line (nb switch raw_input for input in
    python v3 here it's v2.7)
parser = argparse.ArgumentParser()
parser.add_argument('--test', action='store_true', help='mean flag')
parser.add_argument('--quicksave', action='store_true', help='quicksave
    flag')
parser.add_argument('--mean', action='store_true', help='mean flag')
parser.add_argument('--median', action='store_true', help='median flag' )
parser.add_argument('--running', action='store_true', help='running flag' )
parser.add_argument('--grouped', action='store_true', help='grouped flag' )
parser.add_argument('--filterwindow', type=int, help='The size of the
    filter window')
parser.add_argument('filename', help='The name of your input TIFF or cine
```

```
    file, or the directory containing individual TIFF images')
parser.add_argument('--normalise', action='store_true', help='normalise
    the data?' )
args = parser.parse_args()
filterwindow = args.filterwindow
filename = args.filename

# open the file using the magic of PIMS.
input_images = pims.open(args.filename)

if args.quicksave :
    im_out = np.uint16(input_images)
    #io.imsave(filename + '.output.tif',im_out)

elif args.test:
    print 'Testing - speedup'
    im_out =
        np.empty((len(input_images)/filterwindow,input_images[0].shape[0],input_images[0]
    #Parallel(n_jobs=2)(delayed(sqrt)(i ** 2) for i in range(10))
    #Parallel(n_jobs=2)(delayed(sqrt)(i ** 2) for i in range(10))
    #for n in tqdm(range(0,len(input_images)/filterwindow)):
    #im_out[n] = Parallel(n_jobs=2)
        bn.delayed(nanmean)(input_images[n*filterwindow:(n+1)*filterwindow],
        axis=0) for n in range(0,len(input_images)/filterwindow)
    len_t = len(input_images)
    len_x = input_images[0].shape[0]
    len_y = input_images[0].shape[1]
    print len_t, len_x, len_y
    frame_intensity = bn.nanmean(bn.nanmean(input_images, axis=1), axis=1)
    frame_stdev = bn.nanstd(bn.nanstd(input_images, axis=1), axis=1)
    n=0
    #frame_stdev_cumulative[n] = bn.nanstd(bn.nanstd(input_images[],
        axis=1), axis=1)
    plt.subplot(1,2,1)
    plt.plot(frame_intensity)
    plt.ylabel('frame_intensity')
    plt.subplot(1,2,2)
    plt.plot(frame_stdev)
    plt.ylabel('frame_stdev')
    plt.show()
    #im_out = np.uint16(im_out)
    #io.imsave(filename + '.output.tif',im_out)
    print "Finished Testing!"

elif args.grouped:
    print 'Group Averaging', input_images, 'with window size', filterwindow
```

```
    #figure out how big our final array needs to be and pre-populate it
        for speed.
    im_out =
        np.empty((len(input_images)/filterwindow,input_images[0].shape[0],input_images[0]

    if args.mean:
        print "Calculating means..."
        #loop through the image and compute means/medians/etc...
        for n in tqdm(range(0,len(input_images)/filterwindow)):
            im_out[n]=bn.nanmean(input_images[n*filterwindow:(n+1)*filterwindow],
                axis=0)

    elif args.median:
        print "Calculating medians...",
        #loop through the image and compute means/medians/etc...
        for n in tqdm(range(0,len(input_images)/filterwindow)):
            im_out[n] =
                np.uint16(bn.nanmedian(input_images[n*filterwindow:(n+1)*filterwindow],
                axis=0))


    im_out = np.uint16(im_out)
    #io.imsave(filename + '.output.tif',im_out)
    print "Finished!"

elif args.running:
    print "Running Averaging", input_images, " with window size",
        filterwindow
    #im_temp = io.concatenate_images(im_collection)
    if args.mean:
        print "Calculating means..."
        im_out = bn.move_mean(input_images, window=filterwindow,
            min_count=1, axis=0)
    elif args.median:
        print "Calculating median..."
        im_out = bn.move_median(input_images, window=filterwindow,
            min_count=1, axis=0)
    im_out = np.float32(im_out)
    #io.imsave(filename + '.output.tif',im_out)


if args.normalise :
    overall_median = bn.nanmedian(im_out, axis=0)
    im_out = np.float32(im_out / overall_median)
    #print "overall_median", overall_median

io.imsave(filename + '.' + str(filterwindow) + '.output.tif',im_out)
```

```
print 'Saved', filename + '.' + str(filterwindow) + '.output.tif'
```

B.2 ImageJ background subtraction macro (Java)

```
//runs TIFF stack normalisation using median and renames output file
//HC 2014
run("Subtract...", "value=32768 stack"); //only necessary if using
    photonfocus camera
macro "DivideByMedian" {
      var input_StackTitle = getTitle();
      //var stacklength = nSlices;
      var MED_StackTitle = "MED_"+input_StackTitle;
      run("Z Project...", "projection=Median");
      imageCalculator("Divide create 32-bit stack", input_StackTitle,
          MED_StackTitle);
      rename("DivMed_"+input_StackTitle);
      var output_StackTitle = getTitle();
      close(MED_StackTitle);
   }
```

B.3 Matlab

B.3.1 Track analysis

Written by M.R. Cheetham.

```
function [MomentsOut] = AverageSecondMoment(TracksIn)
%AverageSecondMoment Calculate the scalar second moment as a function of
    dt,
%averaged over all tracks
%
%   MomentsOut = AverageSecondMoment(TracksIn)
%
%   Notes: TracksIn is a cell array, with one cell element per track. Each
%   cell element contains an N-by-3 or N-by-4 matrix. The columns should
    contain
%   Frame number, X-position, Y-position, and Intensity (optional),
    respectively.
%   MomentsOut{} is a cell array of 5 cells, which respectively contain
    {1} deltaT,
%   {2} scalar second moment, {3} uncertainty, {4} number of points
    averaged over, and {5} number
%   of tracks averaged over.
```

```
NumSpots = cellfun(@(d) size(d,1),TracksIn);
WaitHandle = waitbar(0, 'Calculating Average Second Moment');
for SubLength = 1:max(NumSpots)
                                                % Set up a loop to count
    over dt for longest track (all other tracks will be covered by this
    loop)
    TempNum = 0;
                                                                % Reset
       temporary counters with each loop iteration
    TempTrackNum = 0;
    for TrackCounter = 1:length(TracksIn)
                                     % Loop over all tracks
       if SubLength <= NumSpots(TrackCounter)
                                    % Perform action if current
          sublength fits inside track
          for SpotCounter = SubLength:NumSpots(TrackCounter)
                       % Loop over possible starting points for
             current dt (sublength)
             TempNum = TempNum+1;
             TempMoment{SubLength}(TempNum) =
                ((TracksIn{TrackCounter}(SpotCounter,2)-...
                TracksIn{TrackCounter}(SpotCounter-SubLength+1,2))^2)+...
                ((TracksIn{TrackCounter}(SpotCounter,3)-TracksIn{TrackCounter}(Spo
          end
          TempTrackNum = TempTrackNum+1;
       end
    end
    %TempStDev{SubLength} =
       sqrt(mean((TempMoment{SubLength}-mean(TempMoment{SubLength})).^2));
       %Calculate Standard Deviation
    TempStDev{SubLength} = std(TempMoment{SubLength}); %Calculate
       Standard Deviation
    MomentsOut{1}(SubLength) = SubLength-1;
                                    % Time
    MomentsOut{2}(SubLength) = mean(TempMoment{SubLength});
                    % Second Moment
    MomentsOut{3}(SubLength) = TempStDev{SubLength}/sqrt(TempNum);
             % Uncertainty
    MomentsOut{4}(SubLength) = TempNum;
                                       % Record Number of Points for
       current dt
    MomentsOut{5}(SubLength) = TempTrackNum;
                                    % Record Number of Tracks that have
       been averaged over
    waitbar(SubLength/max(NumSpots),WaitHandle)
end
close(WaitHandle)
```

```
end
```

B.3.2 Extraction of spot intensities using TrackMate XML co-ordinates

```
%% Automatic Intensity Finder
% Runs GetIntensities code to read TrackMate .xml file and EITHER gauss
% fit, get the pixel intensity from the centre of the spot or average of
    defined number of pixels around the spot.
% **Careful tracking required to make sure that tracks are true and that
    tracks are not split into many smaller tracks**
% HC 17/02/2017

%% User Options
% InterpolateSwitch = true; frames without spots (closed gaps) are
    populated with co-ordinates from last spot and intensities found.
% InterpolateSwitch = false; intensities in gaps are not found.
InterpolateSwitch = false;
% AnalysisMethod 'gauss' = gaussian fit; 'pixel' = intensity of central
    pixel; 'average' = mean of defined box around central pixel.
AnalysisMethod = 'gauss';
% Define the length of the grid used for 2D Gaussian fitting for
    intensities; MUST BE ODD.
% Define size of kernel in case = average.
GridSize = 31;
FrameTime = 0.02; % Define frame time in ms
PixelSize = 30.0; %Define pixel size in nm, 100x 57.5 nm, 60x 94.3 nm,
    photonfocus 100x 30.0

Bins = 100; %Define number of bins for histogram of intensities.

%% Read Data
[TMFile,TMPath]=uigetfile('*.xml', 'Select TrackMate File...');
MyTracks = ReadTrackMateXML2([TMPath,TMFile]);

%% Re-structure the Tracks Cell Array to populate missing entries (Gap
    Closing)
% Copies previous co-ordinates when a spot is missing from the tracks and
    gets the intensity value.
if InterpolateSwitch
    NewTracks = cell(numel(MyTracks),1);
    for TrackCounter = 1:numel(MyTracks)
        NewTracks{TrackCounter} = zeros(MyTracks{TrackCounter}(end,1) -
            MyTracks{TrackCounter}(1,1) + 1,3);
```

```
        for PointCounter =
            MyTracks{TrackCounter}(1,1):MyTracks{TrackCounter}(end,1)
            LoopIndex = PointCounter - MyTracks{TrackCounter}(1,1) + 1;
            if ~isempty(find(MyTracks{TrackCounter}(:,1) == PointCounter,
                1))
                NewTracks{TrackCounter}(LoopIndex, :) =
                    MyTracks{TrackCounter}(find(MyTracks{TrackCounter}(:,1)
                    == PointCounter, 1), :);
            else
                NewTracks{TrackCounter}(LoopIndex, :) =
                    [NewTracks{TrackCounter}(LoopIndex - 1, 1) + 1,
                    NewTracks{TrackCounter}(LoopIndex - 1, 2:end)];
            end
        end
    end
    MyTracks = NewTracks; %Overwrite the tracks data with interpolated
        version
end

%% Populate Pixel Intensities
% Selects the image file pixel from which pixel intensities are to be
    taken and runs GetIntensities
[IMFile,IMPath]=uigetfile('*.tif', 'Select TIFF File...');
MyTracks =
    GetIntensities(MyTracks,[IMPath,IMFile],AnalysisMethod,GridSize);

%% Review Data
% SELECT RELEVANT SECTIONS TO REVIEW DATA
% Display one matrix for each track [Frame Number, X , Y , Intensity]
%MyTracks{:}

%either chose 'figure' and comment out hold to produce seperate graphs
    or...
%...comment out figure and have 'hold on' to apend to one graph

% Histogram intensities
AllIntensities = MyTracks{1}(:,4);
for TempTrack = 2:numel(MyTracks)
    AllIntensities = vertcat(AllIntensities,MyTracks{TempTrack}(:,4));
end
% Remove negative values
Index = AllIntensities >= 0;
FilteredIntensities = AllIntensities(Index);
Index = FilteredIntensities < 2;
FilteredIntensities = FilteredIntensities(Index);
Contrast = FilteredIntensities*100;
```

```
%AllIntensities = (AllIntensities-1)*100 %for converting intensities to...
%...contrast if using pixel or average

figure('position', [0, 0, 415, 400])
histogram(Contrast,Bins)
xlabel('Contrast', 'FontSize', 14)
ylabel('Number', 'FontSize', 14)
box on
set(gca,'fontsize',14)


% % Plot Intensity (:,4) against Frame number (:,1)
% figure('position', [0, 0, 415, 400])
% for TempTrack = 1:numel(MyTracks)
% %figure
% plot(MyTracks{TempTrack}(:,1)*FrameTime,MyTracks{TempTrack}(:,4))
% xlabel('Time / s', 'FontSize', 14)
% ylabel('Normalised Intensity', 'FontSize', 14)
% hold on
% end
% box on
% set(gca,'fontsize',14)
%
% % Plot Intensity (:,4) against x position (:,2)
% figure('position', [0, 0, 415, 400])
% for TempTrack = 1:numel(MyTracks)
% %figure
% scatter((MyTracks{TempTrack}(:,2))*PixelSize,MyTracks{TempTrack}(:,4))
% xlabel('x / nm', 'FontSize', 14)
% ylabel('Normalised Intensity', 'FontSize', 14)
% hold on
% end
% box on
% set(gca,'fontsize',14)
%
% figure('position', [0, 0, 415, 400])
% for TempTrack = 1:numel(MyTracks)
% %figure
% scatter((MyTracks{TempTrack}(:,3))*PixelSize,MyTracks{TempTrack}(:,4))
% xlabel('y / nm', 'FontSize', 14)
% ylabel('Normalised Intensity', 'FontSize', 14)
% hold on
% end
% box on
% set(gca,'fontsize',14)
% % figure
% % % %
```

```
% % % % Plot Intensity (:,4) againist y position (:,3)
% % for TempTrack = 1:numel(MyTracks)
% % %figure
% % scatter((MyTracks{TempTrack}(:,3))*PixelSize,MyTracks{TempTrack}(:,4))
% % xlabel('y position / nm')
% % ylabel('Normalised Intensity')
% % hold on
% % end
%
% % % Plot x position (:,2) againist y position (:,3)
% figure('position', [0, 0, 480, 400])
% for TempTrack = 1:numel(MyTracks)
% %figure
% c = MyTracks{TempTrack}(:,4);
% c = c';
%
    scatter((MyTracks{TempTrack}(:,2))*PixelSize,(MyTracks{TempTrack}(:,3))*PixelSize,
    [], c, 'filled')
% xlabel('x / nm', 'FontSize', 14)
% ylabel('y / nm', 'FontSize', 14)
% hold on
% end
% box on
% set(gca,'fontsize',14)
% %set(gca,'XMinorTick','on','YMinorTick','on')
% colorbar
%
% %[ExportFile,ExportPath] = uiputfile('*.csv','Export Data As...');
% %csvwrite([ExportPath,ExportFile],cell2mat(MyTracks))

%% Save
[temppath,tempfile,~] = fileparts([IMPath,IMFile]);
[SaveFile, SavePath] = uiputfile('*.mat', 'Save Data as...',
    fullfile(temppath,tempfile));
if ~(SaveFile == 0)
    save([SavePath, SaveFile]);
end
```

B.3.3 Monte Carlo simulations

Written by M.R. Cheetham.

```
function [TracksOut] = SimulateSM2(SaveFile,ParamsIn)
%SimulateSM2 Performs a Monte Carlo simulation of single molecule diffusion
%using the Continuous Time Random Walk (CTRW) model
%   GeneratedTracks = SimulateSM2(SaveFile,ParamsIn)
```

```
%
%   SaveFile is the complete path to a file where the generated image stack
%   will be saved; ParamsIn is a struct containing the following fields:
%   NumParticles is the total number of tracks to
%   simulate; FrameTime is the exposure time per frame; StepsPerFrame
%   specifies the number of time steps per frame, set this number higher
%   for better results; Diffusivity is the diffusion coefficient in um^2/s;
%   NumFrames is the length (in frames) of the generated image stack;
%   ImRes is spatial length (in pixels) of each frame, assuming a
%   square image; PixelSize is the number of um per pixel (sets the image
%   scale); SpotWidth is the Gaussian size (in um) of each single molecule;
%   SigNoise is the SNR of the image - set higher for cleaner spots.
%
%   Example
%          SimParams.NumParticles = 100;
%          SimParams.FrameTime = 0.02;
%          SimParams.StepsPerFrame = 10;
%          SimParams.Diffusivity = 5;
%          SimParams.NumFrames = 1000;
%          SimParams.ImRes = 128;
%          SimParams.PixelSize = 0.4;
%          SimParams.SpotWidth = 1;
%          SimParams.SigNoise = 7;
%          MyTracks = SimulateSM('/Desktop/FakeImage.tif',SimParams);
%      will generate an image stack of 1000 128x128 frames of 100
%      simulated single molecules, with a 20 ms frame time, 10 steps per
%      frame, a diffusivity of 5 um^2/s, a scale of 0.4 um per pixel,
%      Gaussian spot size of 1 um, and a single-to-noise ratio of 7. The
%      resulting image stack will be placed on the Desktop with the name
%      'FakeImage.tif'
%
%   Updated 16th Feb 2016 14:48 GMT
%     2015 Matthew R. Cheetham and University of Oxford

    %% Initial Setup
    TimeStep = ParamsIn.FrameTime/ParamsIn.StepsPerFrame;
                                % Set the temporal resolution of the
       simulation - set MUCH smaller than TimeSample for good data
    SpotAmp = 100;                                                  % Set
       the Gaussian amplitude of a spot
    % Setup length step and number of time steps automatically
    LengthStep = sqrt(2*ParamsIn.Diffusivity*TimeStep);
                            % This is in units of um, NOT pixels
    NumTimeSteps = ParamsIn.NumFrames*(ParamsIn.FrameTime/TimeStep);
                      % This is an integer stating how many total time
       steps to compute
```

```
%% Generate Tracks
WaitHandle=waitbar(0,'Running Monte Carlo Simulation...');       %
    Create a Progress Bar
for TrackCounter=1:ParamsIn.NumParticles
    NumSpots(TrackCounter)=randi(NumTimeSteps - ParamsIn.StepsPerFrame)
        + ParamsIn.StepsPerFrame;              % Randomly select the
        length of each track, at least length 2
    SimTracks{TrackCounter}(1,:)=[randi(NumTimeSteps-(NumSpots(TrackCounter)-1)),...
        randi(ParamsIn.ImRes),randi(ParamsIn.ImRes)];
                                        % Randomly find the starting
            point for each track, ensuring the end does not occur beyond
            maximum frame
    for SpotCounter=2:NumSpots(TrackCounter)
        SimTracks{TrackCounter}(SpotCounter,:)=SimTracks{TrackCounter}(SpotCounter-1,
            [1,(LengthStep/ParamsIn.PixelSize)*randn,...
            (LengthStep/ParamsIn.PixelSize)*randn];          % Do the
                molecular dance!
    end
    FrameIndex =
        ((SimTracks{TrackCounter}(:,1)-1)*(TimeStep/ParamsIn.FrameTime))+1;
    KeepFrameIndex = abs(FrameIndex-round(FrameIndex)) <
        TimeStep/ParamsIn.StepsPerFrame; %Error?
    SimTracksChopped{TrackCounter} =
        [FrameIndex(KeepFrameIndex),SimTracks{TrackCounter}(KeepFrameIndex,[2,3])];
    waitbar((TrackCounter-1)/ParamsIn.NumParticles,WaitHandle);
end
close(WaitHandle);

%% Generate Images from tracks
ImageMatrix=zeros(ParamsIn.ImRes,ParamsIn.ImRes,ParamsIn.NumFrames);
                        % Create an empty 3D image matrix
TwoDeeGauss=@(params,x,y)
    SpotAmp*exp(-0.5*((((x-params(1))/ParamsIn.SpotWidth).^2)+...
    (((y-params(2))/ParamsIn.SpotWidth).^2)));
                                % Define a 2D Gaussian function for
        spots
x = 1:ParamsIn.ImRes;
                                                        % Create vector
    of integers for x coordinates
y = 1:ParamsIn.ImRes;
                                                        % Create vector
    of integers for y coordinates
[x,y] = meshgrid(x,y);                                              %
    Create a matrix of arguments to put into 2D function
for TrackCounter=1:ParamsIn.NumParticles
                                    % Loop over tracks
    for FrameCounter=1:length(SimTracksChopped{TrackCounter}(:,1)) %
```

```
        Loop over frames included in current track
        frIndex = SimTracksChopped{TrackCounter}(FrameCounter,1); %
            Obtain actual frame index for current loop counter
        ImageMatrix(:,:,frIndex) = ImageMatrix(:,:,frIndex) + ... %
            Update current frame with information for this spot
            TwoDeeGauss(SimTracksChopped{TrackCounter}(FrameCounter,2:3),x,y);
    end
end

%% Add laser background
LaserGauss = @(params,x,y)
    exp(-0.5*((((x-params(1))/(ParamsIn.ImRes/3)).^2)+...
    (((y-params(2))/(ParamsIn.ImRes/3)).^2)));
                                % Define a laser illumination profile
TempMax = max(ImageMatrix(:));                                      %
    Store max pixel value BEFORE noise is added (for scaling)
LaserNoiseFunction = @(meani,sd)
    meani+sd*randn(ParamsIn.ImRes,ParamsIn.ImRes,ParamsIn.NumFrames);
LaserNoise =
    LaserNoiseFunction(SpotAmp/ParamsIn.SigNoise,SpotAmp/ParamsIn.SigNoise);
        % Generate noise from the laser (flat profile, curved by next
    step)
ImageMatrix = ImageMatrix + LaserNoise.*(LaserNoise>=0);          % Add
    the laser noise to the image

%% Add illumination profile
ImageMatrix = bsxfun(@times, ImageMatrix,...
    LaserGauss([ParamsIn.ImRes/2,ParamsIn.ImRes/2],x,y));
                               % Laser Profile applied to whole image
        so far

%% Add CCD Noise to the image
CCDNoiseFunction = @(meani,sd)
    meani+sd*randn(ParamsIn.ImRes,ParamsIn.ImRes,ParamsIn.NumFrames);
CCDNoise =
    CCDNoiseFunction(SpotAmp/ParamsIn.SigNoise,SpotAmp/ParamsIn.SigNoise);
            % Generate noise from the CCD
ImageMatrix = ImageMatrix + CCDNoise.*(CCDNoise>=0);              % Add
    the CCD noise to the image (always flat)

%% Convert to Image Data and scale for min and max
ImageMatrix = uint16((ImageMatrix./TempMax)*(2^16-1));            %
    Scale the image intensity
for FrameCounter=1:ParamsIn.NumFrames
    imwrite(ImageMatrix(:,:,FrameCounter),SaveFile,...
        'WriteMode','append');                                    %
            Write each frame of the image
```

```
    end

    %% Spit out the Generated Tracks
    TracksOut = SimTracksChopped;
end
```

Bibliography

[1] Alberts, B. *et al.* Cell Chemistry and Biosynthesis. In Goatly, B., Singer Anderson, M. & Dilernia, B. (eds.) *Molecular Biology of the Cell*, chap. 2, 61 (Garland Science, New York, 2002), fourth edn.

[2] Scrimgeour, C. & Harwood, J. L. Fatty Acid and Lipid Structure. In Gunstone, F. D., Harwood, J. L. & Dijkstra, A. J. (eds.) *The Lipid Handbook*, chap. 1, 1–16 (CRC Press, 2007), third edn.

[3] Redwood, W. R., Pfeiffer, F. R., Weisbach, J. A. & Thompson, T. E. Physical properties of bilayer membranes formed from a synthetic saturated phospholipid in n-decane. *BBA - Biomembranes* **233**, 1–6 (1971).

[4] Birdi, K. Surface and Colloid Chemistry. In Birdi, K. (ed.) *Handobook of Surface and Colloid Chemistry*, chap. 1, 1–40 (CRC Press, 2008), third edn.

[5] Kralchevsky, P., Krassimir, D. & Denkov, N. Chemical Physics of Colloid Systems and Interfaces. In Birdi, K. (ed.) *Handbook of Surface and Colloid Chemistry*, chap. 7, 199–355 (CRC Press, 2008), third edn.

[6] Israelachvili, J. N. Soft and Biological Structures. In Israelachvili, J. N. (ed.) *Intermolecular and Surface Forces*, chap. 20, 535–576 (Elsevier, 2011), third edn.

[7] Bangham, A. D. & Horne, R. W. Negative staining of phospholipids and their structural modification by surface-active agents as observed in the electron microscope. *Journal of Molecular Biology* **8**, 660–668 (1964).

[8] Alberts, B. *et al.* Membrane transport of small molecules and the electricl properties of membranes. In Goatly, B., Singer Anderson, M. & Dilernia, B. (eds.) *Molecular Biology of the Cell*, chap. 11, 615–658 (Garland Science, New York, 2002), fourth edn.

[9] Bernardino de la Serna, J., Schütz, G. J., Eggeling, C. & Cebecauer, M. There Is No Simple Model of the Plasma Membrane Organization. *Frontiers in Cell and Developmental Biology* **4**, 106 (2016).

[10] Alberts, B. *et al.* Membrane Structure. In Goatly, B., Singer Anderson, M. & Dilernia, B. (eds.) *Molecular Biology of the Cell*, chap. 10, 583–614 (Garland Science, New York, 2002), fourth edn.

[11] Singer, S. J. & Nicolson, G. L. The Fluid Mosaic Model of the Structure of Cell Membranes. *Science* **175**, 720–731 (1972).

[12] Spector, A. A. & Yorek, M. A. Membrane lipid composition and cellular function. *Journal of lipid research* **26**, 1015–1035 (1985).

[13] Gracià, R. S., Bezlyepkina, N., Knorr, R. L., Lipowsky, R. & Dimova, R. Effect of cholesterol on the rigidity of saturated and unsaturated membranes: fluctuation and electrodeformation analysis of giant vesicles. *Soft Matter* **6**, 1472–1482 (2010).

[14] Hazel, J. R. & Eugene Williams, E. The role of alterations in membrane lipid composition in enabling physiological adaptation of organisms to their physical environment. *Progress in Lipid Research* **29**, 167–227 (1990).

[15] Frolov, V. A., Shnyrova, A. V. & Zimmerberg, J. Lipid polymorphisms and membrane shape. *Cold Spring Harbor Perspectives in Biology* **3**, a004747 (2011).

[16] Özcan, N. *et al.* Osmolality, temperature, and membrane lipid composition modulate the activity of betaine transporter BetP in Corynebacterium glutamicum. *Journal of Bacteriology* **189**, 7485–7496 (2007).

[17] Rowlett, V. W. *et al.* Impact of membrane phospholipid alterations in Escherichia coli on cellular function and bacterial stress adaptation. *Journal of Bacteriology* **199**, e00849–16 (2017).

[18] Márquez, M. G., Favale, N. O., Leocata Nieto, F., Pescio, L. G. & Sterin-Speziale, N. Changes in membrane lipid composition cause alterations in epithelial cell-cell adhesion structures in renal papillary collecting duct cells. *Biochimica et Biophysica Acta - Biomembranes* **1818**, 491–501 (2012).

[19] Saffman, P. G., Delbruck, M. & Delbrück, M. Brownian motion in biological membranes. *Proc Natl Acad Sci USA* **72**, 3111–3113 (1975).

[20] Hughes, B. D., Pailthorpe, B. A. & White, L. R. The Translational And Rotational Drag On A Cylinder Moving In A Membrane. *Journal of Fluid Mechanics* **110**, 349–372 (1981).

[21] Bretscher, M. S. Asymmetrical lipid bilayer structure for biological membranes. *Nature New Biology* **236**, 11–12 (1972).

[22] Rothman, J. & Lenard, J. Membrane asymmetry. *Science* **195**, 743–753 (1977).

[23] Elani, Y. *et al.* Measurements of the effect of membrane asymmetry on the mechanical properties of lipid bilayers. *Chem. Commun.* **51**, 6976–6979 (2015).

[24] Huang, K. C., Mukhopadhyay, R. & Wingreen, N. S. A curvature-mediated mechanism for localization of lipids to bacterial poles. *PLoS Computational Biology* **2**, 1357–1364 (2006).

[25] Mileykovskaya, E. & Dowhan, W. Visualization of phospholipid domains in Escherichia coli by using the cardiolipin-specific fluorescent dye 10-N-nonyl acridine orange. *Journal of Bacteriology* **182**, 1172–1175 (2000).

[26] Daleke, D. L. Regulation of transbilayer plasma membrane phospholipid asymmetry. *Journal of Lipid Research* **44**, 233–242 (2003).

[27] Hankins, H. M., Baldridge, R. D., Xu, P. & Graham, T. R. Role of Flippases, Scramblases and Transfer Proteins in Phosphatidylserine Subcellular Distribution. *Traffic* **16**, 35–47 (2015).

[28] Slotte, J. Sphingomyelincholesterol interactions in biological and model membranes. *Chemistry and Physics of Lipids* **102**, 13–27 (1999).

[29] de Wit, G., Danial, J. S. H., Kukura, P. & Wallace, M. I. Dynamic label-free imaging of lipid nanodomains. *Proceedings of the National Academy of Sciences* **112**, 12299–12303 (2015).

[30] Simons, K. & Ikonen, E. Functional rafts in cell membranes. *Nature* **387**, 569–572 (1997).

[31] Nicolson, G. L. The Fluid-Mosaic Model of Membrane Structure: Still relevant to understanding the structure, function and dynamics of biological membranes after more than 40 years. *Biochimica et Biophysica Acta (BBA) - Biomembranes* **1838**, 1451–1466 (2014).

[32] Yeagle, P. L. Lipid Protein Interactions in Membranes. In *The Membranes of Cells*, chap. 11, 291–334 (Elsevier, 2016).

[33] Mouritsen, O. G. & Bloom, M. Mattress model of lipid-protein interactions in membranes. *Biophysical Journal* **46**, 141–153 (1984).

[34] Alberts, B. *et al.* The Self-Assembly and Dynamic Structure of Cytoskeletal Filaments. In Goatly, B., Singer Anderson, M. & Dilernia, B. (eds.) *Molecular Biology of the Cell*, chap. 16, 987–992 (Garland Science, New York, 2002), fourth edn.

[35] Luna, E. J. & Hitt, A. L. Cytoskeleton–plasma membrane interactions. *Science (New York, N.Y.)* **258**, 955–964 (1992).

[36] Bezanilla, M., Gladfelter, A. S., Kovar, D. R. & Lee, W. L. Cytoskeletal dynamics: A view from the membrane. *Journal of Cell Biology* **209**, 329–337 (2015).

[37] Nicolson, G. L. Transmembrane control of the receptors on normal and tumor cells. *Biochim. Biophys. Acta* **457**, 57–108 (1976).

[38] Kusumi, A. & Sako, Y. Cell surface organization by the membrane skeleton. *Cell* **8**, 566–574 (1996).

[39] Einstein, A. Über die von der molekularkinetischen Theorie der Wärme geforderte Bewegung von in ruhenden Flüssigkeiten suspendierten Teilchen. *Annalen der Physik* **322**, 549–560 (1905). 9811186.

[40] Havlin, S. & Ben-Avraham, D. Diffusion in disordered media. *Advances in Physics* **51**, 187–292 (2002).

[41] Saxton, M. J. Anomalous diffusion due to obstacles: a Monte Carlo study. *Biophysical Journal* **66**, 394–401 (1994).

[42] Kusumi, A., Tsunoyama, T. A., Hirosawa, K. M., Kasai, R. S. & Fujiwara, T. K. Tracking single molecules at work in living cells. *Nature Chemical Biology* **10**, 524–532 (2014).

[43] Höfling, F. & Franosch, T. Anomalous transport in the crowded world of biological cells. *Reports on Progress in Physics* **76**, 046602 (2013).

[44] Fujiwara, T. K. *et al.* Confined diffusion of transmembrane proteins and lipids induced by the same actin meshwork lining the plasma membrane. *Molecular Biology of the Cell* **27**, 1101–1119 (2016).

[45] Golan, Y. & Sherman, E. Resolving mixed mechanisms of protein subdiffusion at the T cell plasma membrane. *Nature Communications* **8**, 15851 (2017).

[46] Kusumi, A. *et al.* Paradigm shift of the plasma membrane concept from the two-dimensional continuum fluid to the partitioned fluid: high-speed single-molecule tracking of membrane molecules. *Annual review of biophysics and biomolecular structure* **34**, 351–378 (2005).

[47] Fujiwara, T., Ritchie, K., Murakoshi, H., Jacobson, K. & Kusumi, A. Phospholipids undergo hop diffusion in compartmentalized cell membrane. *The Journal of cell biology* **157**, 1071–1081 (2002).

[48] Murase, K. *et al.* Ultrafine Membrane Compartments for Molecular Diffusion as Revealed by Single Molecule Techniques. *Biophysical Journal* **86**, 4075–4093 (2004).

[49] Sako, Y. & Kusumi, A. Compartmentalized structure of the plasma membrane for receptor movements as revealed by a nanometer-level motion analysis. *Journal of Cell Biology* **125**, 1251–1264 (1994).

[50] Kusumi, A., Sako, Y. & Yamamoto, M. Confined Lateral Diffusion of Membrane-Receptors as Studied by Single-Particle Tracking (Nanovid Microscopy) - Effects of Calcium-Induced Differentiation in Cultured Epithelial-Cells. *Biophysical Journal* **65**, 2021–2040 (1993).

[51] Schütz, G. J., Schindler, H. & Schmidt, T. Single-molecule microscopy on model membranes reveals anomalous diffusion. *Biophysical Journal* **73**, 1073–1080 (1997).

[52] Weigel, A. V., Simon, B., Tamkun, M. M. & Krapf, D. Ergodic and nonergodic processes coexist in the plasma membrane as observed by single-molecule tracking. *Proceedings of the National Academy of Sciences* **108**, 6438–6443 (2011).

[53] Saxton, M. J. Lateral diffusion in an archipelago. The effect of mobile obstacles. *Biophysical Journal* **52**, 989–997 (1987).

[54] Berry, H. & Chaté, H. Anomalous diffusion due to hindering by mobile obstacles undergoing Brownian motion or Orstein-Ulhenbeck processes. *Physical Review E - Statistical, Nonlinear, and Soft Matter Physics* **89**, 022708 (2014).

[55] Saxton, M. J. Lateral diffusion in an archipelago. Dependence on tracer size. *Biophysical Journal* **64**, 1053–1062 (1993).

[56] Manzo, C. *et al.* Weak ergodicity breaking of receptor motion in living cells stemming from random diffusivity. *Physical Review X* **5**, 011021 (2015).

[57] Saxton, M. J. Lateral diffusion in an archipelago. Distance dependence of the diffusion coefficient. *Biophysical Journal* **56**, 615–622 (1989).

[58] Saxton, M. J. Anomalous subdiffusion in fluorescence photobleaching recovery: A Monte Carlo study. *Biophysical Journal* **81**, 2226–2240 (2001).

[59] Mardoukhi, Y., Jeon, J.-H. & Metzler, R. Geometry controlled anomalous diffusion in random fractal geometries: looking beyond the infinite cluster. *Phys. Chem. Chem. Phys.* **44**, 30134–30147 (2015).

[60] Stachura, S. & Kneller, G. R. Anomalous lateral diffusion in lipid bilayers observed by molecular dynamics simulations with atomistic and coarse-grained force fields. *Molecular Simulation* **40**, 245–250 (2014).

[61] Koldsø, H., Reddy, T., Fowler, P. W., Duncan, A. L. & Sansom, M. S. P. Membrane Compartmentalization Reduces the Mobility of Lipids and Proteins within a Model Plasma Membrane. *J. Phys. Chem. B* **120**, 8873–8881 (2016).

[62] Jeon, J.-H., Javanainen, M., Martinez-Seara, H., Metzler, R. & Vattulainen, I. Protein Crowding in Lipid Bilayers Gives Rise to Non-Gaussian Anomalous Lateral Diffusion of Phospholipids and Proteins. *Physical Review X* **6**, 021006 (2016).

[63] Bakalis, E., Höfinger, S., Venturini, A. & Zerbetto, F. Crossover of two power laws in the anomalous diffusion of a two lipid membrane. *Journal of Chemical Physics* **142**, 215102 (2015).

[64] Javanainen, M. *et al.* Anomalous and normal diffusion of proteins and lipids in crowded lipid membranes. *Faraday Discuss.* **161**, 397–417 (2013).

[65] Ratto, T. V. & Longo, M. L. Anomalous subdiffusion in heterogeneous lipid bilayers. *Langmuir* **19**, 1788–1793 (2003).

[66] Rose, M., Hirmiz, N., Moran-Mirabal, J. M. & Fradin, C. Lipid diffusion in supported lipid bilayers: A comparison between line-scanning fluorescence correlation spectroscopy and single-particle tracking. *Membranes* **5**, 702–721 (2015).

[67] Horton, M. R., Höfling, F., Rädler, J. O. & Franosch, T. Development of anomalous diffusion among crowding proteins. *Soft Matter* **6**, 2648–2656 (2010).

[68] Spillane, K. M. *et al.* High-Speed Single-Particle Tracking of GM1 in Model Membranes Reveals Anomalous Diffusion due to Interleaflet Coupling and Molecular Pinning. *Nano letters* **14**, 5390–5397 (2014).

[69] Wu, H.-M., Lin, Y.-H., Yen, T.-C. & Hsieh, C.-L. Nanoscopic substructures of raft-mimetic liquid-ordered membrane domains revealed by high-speed single-particle tracking. *Scientific reports* **6**, 20542 (2016).

[70] Kepten, E., Weron, A., Sikora, G., Burnecki, K. & Garini, Y. Guidelines for the fitting of anomalous diffusion mean square displacement graphs from single particle tracking experiments. *PLoS ONE* **10**, e0117722 (2015).

[71] Magdziarz, M. & Weron, A. Anomalous diffusion: Testing ergodicity breaking in experimental data. *Physical Review E - Statistical, Nonlinear, and Soft Matter Physics* **84**, 051138 (2011).

[72] Metzler, R., Jeon, J.-H., Cherstvy, A. G. & Barkai, E. Anomalous diffusion models and their properties: non-stationarity, non-ergodicity, and ageing at the centenary of single particle tracking. *Phys. Chem. Chem. Phys.* **16**, 24128–24164 (2014).

[73] Mueller, P., Rudin, D. O., Ti Tien, H. & Wescott, W. C. Reconstitution of cell membrane structure in vitro and its transformation into an excitable system. *Nature* **194**, 979–980 (1962).

[74] Montal, M. & Mueller, P. Formation of Bimolecular Membranes from Lipid Monolayers and a Study of Their Electrical Properties. *Proceedings of the National Academy of Sciences* **69**, 3561–3566 (1972).

[75] Tien, H. T. Thickness and molecular organization of bimolecular lipid membranes in aqueous media (1966).

[76] Tamm, L. K. & McConnell, H. M. Supported phospholipid bilayers. *Biophysical Journal* **47**, 105–113 (1985).

[77] Richter, R. P., Bérat, R. & Brisson, A. R. Formation of solid-supported lipid bilayers: an integrated view. *Langmuir : the ACS journal of surfaces and colloids* **22**, 3497–505 (2006).

[78] Andrecka, J., Spillane, K. M., Ortega-Arroyo, J. & Kukura, P. Direct observation and control of supported lipid bilayer formation with interferometric scattering microscopy. *ACS nano* **7**, 10662–10670 (2013).

[79] Charitat, T., Bellet-Amalric, E., Fragneto, G. & Graner, F. Adsorbed and free lipid bilayers at the solid-liquid interface. *European Physical Journal B* **8**, 583–593 (1999).

[80] Knoll, W. *et al.* Functional tethered lipid bilayers. *Journal of biotechnology* **74**, 137–158 (2000).

[81] Mccabe, I. P. & Forstner, M. B. Polymer Supported Lipid Bilayers. *Open Journal of Biophysics* **3**, 59–69 (2013).

[82] Mashaghi, S. & van Oijen, A. M. A versatile approach to the generation of fluid supported lipid bilayers and its applications. *Biotechnology and Bioengineering* **111**, 2076–2081 (2014).

[83] Richter, R. P. & Brisson, A. R. Following the Formation of Supported Lipid Bilayers on Mica: A Study Combining AFM, QCM-D, and Ellipsometry. *Biophysical Journal* **88**, 3422–3433 (2005).

[84] Bayley, H. *et al.* Droplet interface bilayers. *Molecular bioSystems* **4**, 1191–1208 (2008).

[85] Leptihn, S. *et al.* Constructing droplet interface bilayers from the contact of aqueous droplets in oil. *Nature protocols* **8**, 1048–1057 (2013).

[86] Stanley, C. E. *et al.* A microfluidic approach for high-throughput droplet interface bilayer (DIB) formation. *Chemical Communications* **46**, 1620–1622 (2010).

[87] Holden, M. A., Needham, D. & Bayley, H. Functional bionetworks from nanoliter water droplets. *Journal of the American Chemical Society* **129**, 8650–8655 (2007).

[88] Freeman, E. C., Najem, J. S., Sukharev, S., Philen, M. K. & Leo, D. J. The mechanoelectrical response of droplet interface bilayer membranes. *Soft Matter* **12**, 3021–3031 (2016).

[89] Rosholm, K. R. *et al.* Activation of the mechanosensitive ion channel MscL by mechanical stimulation of supported Droplet-Hydrogel bilayers. *Scientific Reports* **7**, 45180 (2017).

[90] Yanez Arteta, M. *et al.* Interactions of PAMAM Dendrimers with Negatively Charged Model Biomembranes. *Journal of Physical Chemistry B* **118**, 12892–12906 (2014).

[91] Najem, J. S., Freeman, E. C., Yasmann, A., Sukharev, S. & Leo, D. J. Mechanics of Droplet Interface Bilayer Unzipping Defines the Bandwidth for the Mechanotransduction Response of Reconstituted MscL. *Advanced Materials Interfaces* **4**, 1600805 (2017).

[92] Sengel, J. T. & Wallace, M. I. Imaging the dynamics of individual electropores. *Proceedings of the National Academy of Sciences* **113**, 5281–5286 (2016).

[93] Huang, S., Romero-Ruiz, M., Castell, O. K., Bayley, H. & Wallace, M. I. High-throughput optical sensing of nucleic acids in a nanopore array. *Nature Nanotechnology* **10**, 986–991 (2015).

[94] Manzo, C. & Garcia-Parajo, M. F. A review of progress in single particle tracking: from methods to biophysical insights. *Reports on progress in physics.* **78**, 124601 (2015).

[95] Ambrose, E. J. A Surface Contact Microscope for the study of Cell Movements. *Nature* **178**, 1194–1194 (1956).

[96] Axelrod, D. Cell-substrate contacts illuminated by total internal reflection fluorescence. *Journal of Cell Biology* **89**, 141–145 (1981).

[97] Fish, K. N. Total Internal Reflection Fluorescence (TIRF) Microscopy. *Currrent Protocols in Cytometry* **12**, 1–21 (2009).

[98] Stout, A. L. & Axelrod, D. Evanescent field excitation of fluorescence by epi-illumination microscopy. *Applied Optics* **28**, 5237–5242 (1989).

[99] Ortega-Arroyo, J. & Kukura, P. Interferometric scattering microscopy (iSCAT): new frontiers in ultrafast and ultrasensitive optical microscopy. *Physical chemistry chemical physics : PCCP* **14**, 15625–15636 (2012).

[100] Hu, M. *et al.* Dark-field microscopy studies of single metal nanoparticles: understanding the factors that influence the linewidth of the localized surface plasmon resonance. *Journal of Materials Chemistry* **18**, 1949–1960 (2008).

[101] Rodríguez-Fajardo, V. *et al.* Two-color dark-field (TCDF) microscopy for metal nanoparticle imaging inside cells. *Nanoscale* **10**, 4019–4027 (2018).

[102] Weber, I. Reflection interference contrast microscopy. *Methods in enzymology* **361**, 34–47 (2003).

[103] Curtis, A. The mechanism of adhesion of cells to glass. A styudy by interference refection microscopy. *The Journal of Cell Biology* **20**, 199–215 (1964).

[104] Verschueren, H. Interference reflection microscopy in cell biology: methodology and applications. *J. Cell Sci* **75**, 279–301 (1985).

[105] Ploem, J. *Mononuclear Phagocytes: In Immunity, Infection, and Pathology* (Blackwell Scientific, Oxford, 1975), 1st edn.

[106] Lindfors, K., Kalkbrenner, T., Stoller, P. & Sandoghdar, V. Detection and Spectroscopy of Gold Nanoparticles Using Supercontinuum White Light Confocal Microscopy. *Physical Review Letters* **93**, 037401 (2004).

[107] Jacobsen, V., Stoller, P., Brunner, C., Vogel, V. & Sandoghdar, V. Interferometric optical detection and tracking of very small gold nanoparticles at a water-glass interface. *Optics Express* **14**, 405–414 (2006).

[108] Spindler, S. *et al.* Visualization of lipids and proteins at high spatial and temporal resolution via interferometric scattering (iSCAT) microscopy. *Journal of Physics D: Applied Physics* **49**, 274002 (2016).

[109] Hsieh, C.-L., Spindler, S., Ehrig, J. & Sandoghdar, V. Tracking single particles on supported lipid membranes: multimobility diffusion and nanoscopic confinement. *The journal of physical chemistry. B* **118**, 1545–1554 (2014).

[110] Coker, H. L. E. *et al.* Controlling Anomalous Diffusion in Lipid Membranes. *ArXiv Pre-press* (2017). 1709.04698.

[111] Andrecka, J. *et al.* Structural dynamics of myosin 5 during processive motion revealed by interferometric scattering microscopy. *eLife* **4**, e05413 (2015).

[112] Andrecka, J. *et al.* Interferometric Scattering Microscopy for the Study of Molecular Motors. In Spies, M. & Chemla, Y. R. (eds.) *Methods in Enzymology*, vol. 581, chap. 17, 517–539 (2016).

[113] Park, J.-S. *et al.* Label-free and live cell imaging by interferometric scattering microscopy. *Chemical Science* **9**, 2690–2697 (2018).

[114] Andrecka, J., OrtegaArroyo, J., Lewis, K., Cross, R. & Kukura, P. Label-free Imaging of Microtubules with Sub-nm Precision Using Interferometric Scattering Microscopy. *Biophysical Journal* **110**, 214–217 (2016).

[115] Ewers, H. *et al.* Label-free optical detection and tracking of single virions bound to their receptors in supported membrane bilayers. *Nano letters* **7**, 2263–2266 (2007).

[116] Kukura, P. *et al.* High-speed nanoscopic tracking of the position and orientation of a single virus. *Nature methods* **6**, 923–927 (2009).

[117] Ortega Arroyo, J. *et al.* Label-free, all-optical detection, imaging, and tracking of a single protein. *Nano letters* **14**, 2065–2070 (2014).

[118] Piliarik, M. & Sandoghdar, V. Direct optical sensing of single unlabelled proteins and super-resolution imaging of their binding sites. *Nature communications* **5**, 4495 (2014).

[119] McDonald, M. P. *et al.* Visualizing Single-Cell Secretion Dynamics with Single-Protein Sensitivity. *Nano Letters* **18**, 513–519 (2018).

[120] Liebel, M., Hugall, J. T. & Van Hulst, N. F. Ultrasensitive Label-Free Nanosensing and High-Speed Tracking of Single Proteins. *Nano Letters* **17**, 1277–1281 (2017).

[121] Avci, O., Ünlü, N. L., Özkumur, A. Y. & Ünlü, M. S. Interferometric reflectance imaging sensor (IRIS)a platform technology for multiplexed diagnostics and digital detection. *Sensors (Switzerland)* **15**, 17649–17665 (2015).

[122] Fringes, S., Holzner, F. & Knoll, A. W. The nanofluidic confinement apparatus: Studying confinement-dependent nanoparticle behavior and diffusion. *Beilstein Journal of Nanotechnology* **9**, 301–310 (2018).

[123] Ortega-Arroyo, J., Bissette, A. J., Kukura, P. & Fletcher, S. P. Visualization of the spontaneous emergence of a complex, dynamic, and autocatalytic system. *Proceedings of the National Academy of Sciences* **113**, 11122–11126 (2016).

[124] Mojarad, N., Sandoghdar, V. & Krishnan, M. Measuring three-dimensional interaction potentials using optical interference. *Optics Express* **21**, 9377–9389 (2013).

[125] Ortega Arroyo, J., Cole, D. & Kukura, P. Interferometric scattering microscopy and its combination with single-molecule fluorescence imaging. *Nature protocols* **11**, 617–633 (2016).

[126] Christy, A., Tavassoli, N., Bain, A., Melo, L. & Grant, E. R. Wide-Field Confocal Interferometric Backscattering (iSCAT)-Raman Microscopy. In *Optics in the Life Sciences*, NM4C.4 (OSA, Washington, D.C., 2015).

[127] Cole, D., Young, G., Weigel, A., Sebesta, A. & Kukura, P. Label-Free Single-Molecule Imaging with Numerical-Aperture-Shaped Interferometric Scattering Microscopy. *ACS Photonics* **4**, 211–216 (2017).

[128] Reina, F. *et al.* Complementary studies of lipid membrane dynamics using iSCAT and STED microscopy. *bioRxiv Pre-press* 235564 (2017).

[129] Brian, A. A. & McConnell, H. M. Allogeneic stimulation of cytotoxic T cells by supported planar membranes. *Proceedings of the National Academy of Sciences of the United States of America* **81**, 6159–6163 (1984).

[130] Tinevez, J. Y. *et al.* TrackMate: An open and extensible platform for single-particle tracking. *Methods* **115**, 80–90 (2017).

[131] Saxton, M. J. Wanted: A positive control for anomalous subdiffusion. *Biophysical Journal* **103**, 2411–2422 (2012).

[132] Kaufmann, S., Papastavrou, G., Kumar, K., Textor, M. & Reimhult, E. A detailed investigation of the formation kinetics and layer structure of poly(ethylene glycol) tether supported lipid bilayer. *Soft Matter* **5**, 2804 (2009).

[133] Axelrod, D., Koppel, D. E., Schlessinger, J., Elson, E. & Webb, W. W. Mobility measurement by analysis of fluorescence photobleaching recovery kinetics. *Biophysical Journal* **16**, 1055–1069 (1976).

[134] Soumpasis, D. M. Theoretical analysis of fluorescence photobleaching recovery experiments. *Biophysical Journal* **41**, 95–97 (1983).

[135] Schwille, P., Korlach, J. & Webb, W. W. Fluorescence correlation spectroscopy with single-molecule sensitivity on cell and model membranes. *Cytometry* **36**, 176–182 (1999).

[136] Feder, T. J., Brust-Mascher, I., Slattery, J. P., Baird, B. & Webb, W. W. Constrained diffusion or immobile fraction on cell surfaces: A new interpretation. *Biophysical Journal* **70**, 2767–2773 (1996).

[137] Smith, P. R., Morrison, I. E., Wilson, K. M., Fernández, N. & Cherry, R. J. Anomalous diffusion of major histocompatibility complex class I molecules on HeLa cells determined by single particle tracking. *Biophysical Journal* **76**, 3331–3344 (1999).

[138] Saxton, M. J. A biological interpretation of transient anomalous subdiffusion. I. Qualitative model. *Biophysical journal* **92**, 1178–1191 (2007).

[139] Tsai, J., Sun, E., Gao, Y., Hone, J. C. & Kam, L. C. Non-Brownian diffusion of membrane molecules in nanopatterned supported lipid bilayers. *Nano Letters* **8**, 425–430 (2008).

[140] Nowacka, A., Douezan, S., Wadsö, L., Topgaard, D. & Sparr, E. Small polar molecules like glycerol and urea can preserve the fluidity of lipid bilayers under dry conditions. *Soft Matter* **8**, 1482–1491 (2012).

[141] Costa-Balogh, F. O., Wennerström, H., Wadsö, L. & Sparr, E. How small polar molecules protect membrane systems against osmotic stress: The urea-water-phospholipid system. *Journal of Physical Chemistry B* **110**, 23845–23852 (2006).

[142] Yu, Z. W., Feng, Y., Wang, J., Dong, B. Z. & Quinn, P. J. Study of the effect of urea on the phase transition of phospholipid by synchrotron X-ray diffraction. *High Energy Physics and Nuclear Physics* **25**, 75–80 (2001).

[143] Yeagle, P. L. & Sen, A. Hydration and the Lamellar to Hexagonal II Phase Transition of Phosphatidylethanolamine. *Biochemistry* **25**, 7518–7522 (1986).

[144] Dewald, A. H., Hodges, J. C. & Columbus, L. Physical determinants of β-barrel membrane protein folding in lipid vesicles. *Biophysical Journal* **100**, 2131–2140 (2011).

[145] Schiffrin, B. *et al.* Effects of Periplasmic Chaperones and Membrane Thickness on BamA-Catalyzed Outer-Membrane Protein Folding. *Journal of Molecular Biology* **429**, 3776–3792 (2017).

[146] Klaus, C. J. S., Raghunathan, K., DiBenedetto, E. & Kenworthy, A. K. Analysis of diffusion in curved surfaces and its application to tubular membranes. *Molecular Biology of the Cell* **27**, 3937–3946 (2016).

[147] Frankel, D. J. *et al.* Revealing the topography of cellular membrane domains by combined atomic force microscopy/fluorescence imaging. *Biophysical Journal* **90**, 2404–2413 (2006).

[148] Sbalzarini, I. F., Hayer, A., Helenius, A. & Koumoutsakos, P. Simulations of (an)isotropic diffusion on curved biological surfaces. *Biophysical Journal* **90**, 878–885 (2006).

[149] Adler, J., Shevchuk, A. I., Novak, P., Korchev, Y. E. & Parmryd, I. Plasma membrane topography and interpretation of single-particle tracks. *Nature Methods* **7**, 170–171 (2010).

[150] Parmryd, I. & Önfelt, B. Consequences of membrane topography. *FEBS Journal* **280**, 2775–2784 (2013).

[151] Hall, D. Analysis and interpretation of two-dimensional single-particle tracking microscopy measurements: Effect of local surface roughness. *Analytical Biochemistry* **377**, 24–32 (2008).

[152] Weiss, M., Hashimoto, H. & Nilsson, T. Anomalous protein diffusion in living cells as seen by fluorescence correlation spectroscopy. *Biophysical Journal* **84**, 4043–4052 (2003).

[153] Cheetham, M. R. *et al.* Concentrating membrane proteins using asymmetric traps and AC electric fields. *Journal of the American Chemical Society* **133**, 6521–6524 (2011).

[154] Werner, J. H. *et al.* Formation and dynamics of supported phospholipid membranes on a periodic nanotextured substrate. *Langmuir* **25**, 2986–2993 (2009).

[155] Fowlkes, J. D. *et al.* Tailored transport through vertically aligned carbon nanofibre membranes; Controlled synthesis, modelling, and passive diffusion experiments. *Nanotechnology* **16**, 3101–3109 (2005).

[156] Boxer, S. Molecular transport and organization in supported lipid membranes. *Current Opinion in Chemical Biology* **4**, 704–709 (2000).

[157] Hovis, J. S. & Boxer, S. G. Patterning barriers to lateral diffusion in supported lipid bilayer membranes by blotting and stamping. *Langmuir* **16**, 894–897 (2000).

[158] Vats, K., Kyoung, M. & Sheets, E. D. Characterizing the chemical complexity of patterned biomimetic membranes. *Biochimica et Biophysica Acta - Biomembranes* **1778**, 2461–2468 (2008).

[159] Kam, L. C. Capturing the nanoscale complexity of cellular membranes in supported lipid bilayers. *Journal of Structural Biology* **168**, 3–10 (2009).

[160] Zhou, X., Moran-Mirabal, J. M., Craighead, H. G. & McEuen, P. L. Supported lipid bilayer/carbon nanotube hybrids. *Nature Nanotechnology* **2**, 185–190 (2007).

[161] Lou, H.-Y., Zhao, W., Zeng, Y. & Cui, B. The Role of Membrane Curvature in Nanoscale Topography-Induced Intracellular Signaling. *Accounts of Chemical Research* **5**, 1046–1053 (2018).

[162] Hanson, L., Lin, Z. C., Xie, C., Cui, Y. & Cui, B. Characterization of the cell-nanopillar interface by transmission electron microscopy. *Nano Letters* **12**, 5815–5820 (2012).

[163] Zhao, W. *et al.* Nanoscale manipulation of membrane curvature for probing endocytosis in live cells. *Nature Nanotechnology* **12**, 750–756 (2017).

[164] McCloskey, M. A. & Poo, M. M. Rates of membrane-associated reactions: Reduction of dimensionality revisited. *Journal of Cell Biology* **102**, 88–96 (1986).

[165] Eze, M. O. Consequences of the Lipid Bilayer to Membrane-Associated Reactions. *Journal of Chemical Education* **67**, 17–20 (1990).

[166] Golding, I. & Cox, E. C. Physical nature of bacterial cytoplasm. *Physical Review Letters* **96**, 098102 (2006).

[167] Guigas, G. & Weiss, M. Sampling the cell with anomalous diffusion - The discovery of slowness. *Biophysical Journal* **94**, 90–94 (2008).

[168] Jacobsen, V., Klotzsch, E. & Sandoghdar, V. Interferometric detection and tracking of nanoparticles. In Masuhara, H., Kawata, S. & Tokunaga, F. (eds.) *Nano Biophotonics: Science and Technology*, chap. 9, 143–158 (Elsevier, 2007), third edn.